Pierre-Daniel Jameson

Machine Vision and Scientific Imaging for Autonomous Air Vehicles (UAV)

School of Engineering (College of Aeronautics)

MSc Aerospace Dynamics (Dynamics)

o0o- Intentionally left blank -o0o

Title page

School of Engineering (College of Aeronautics)

MSc Aerospace Dynamics (Dynamics)

Academic year 2007 - 2008

Pierre-Daniel Jameson

Machine Vision and Scientific Imaging for Autonomous Air Vehicles (UAV)

Supervisor:….....**Dr A.K. Cooke, Department of Aerospace Sciences**

Assistant Supervisor:.....**Dr S.E Hobbs, Cranfield Space Research Centre**

September 2008

This thesis is submitted in partial [50%] weighting fulfilment of the requirements for the Degree of Master of Science in Aerospace Dynamics (Dynamics option).

o0o- Intentionally left blank -o0o

Abstract:

This thesis outlines the necessary requirements to determine an Unmanned Aerial Vehicles (UAV's) pose relative to a lead aircraft or target, thus enabling a UAV to successfully follow a lead aircraft or target. The use of Machine Vision for Autonomous navigation has been investigated and two flight scenarios were chosen for analysis. Firstly, following a manoeuvring lead aircraft, and secondly, maintaining a steady heading behind a target/lead aircraft (as would be required for in-flight refuelling). In addition, the author has performed a literature review of current research in this field which is significantly dominated by eventual military requirements in order to improve UAV endurance.

In addition, experimental work towards developing a passive vision based navigation system has been undertaken. It is hoped that after further research and development this will lead to an eventual flight trial using the flight dynamics department's UAV's. The experimental work has been performed using both equipment and software already available within the department and furthermore, it has enabled an analysis of the department's currently available capabilities for passive visual navigation to be undertaken. Key points for further work have been outlined for the future advancement of the visual navigation project.

o0o- Intentionally left blank -o0o

Acknowledgements:

I would like to take the opportunity to thank the following members of staff:

Dr A.K Cooke, for his guidance and support and also for giving me the chance to undertake a project within the UAV domain.
Dr S.E Hobbs for his time, encouragement and patience with my many questions on *Camera Calibration.*
Dr J.F Whidborne for his continued support and availability throughout the year.
Mr M. V Cook for his constructive questions and for the time he spent in discussion.
Barry Walker for his help during the experimental work.
Both Cathy Carr and Heather Woodfield for their help in getting to grips with using the vast library resources.

I would also like to extend my sincere thanks and warmest regards to all the *AD* students for their friendship, good cheer and for making Cranfield University what it was during this past year.

I am also deeply indebted to my first flight dynamics teacher, Dr T.Rahulan, for having shared his knowledge and passion for this subject.

Finally, I would like to dedicate this work as a token of my appreciation to my family.

o0o- Intentionally left blank -o0o

Contents:

Page

Appendices for Experimental work:

Figures:

Page

Tables:

Inserts:

Appendix (Figures & Tables):

Abbreviations:

A/D…… Analogue to Digital
AFC……Autonomous Flight Control
APS……..... Active Pixel Sensors

CAD……... Computer Aided Design
CC…….. Charge Couple
CCD……... Charged Couple Device
CMOS…..... Complementary Metal Oxide Semiconductor
CORSE…….. Centre Only Relative State Estimation
COTS……. Commercial Off The Shelf

DLT……Direct Linear Transformation
DN……..Digital Number

EKF…… Extended Kalman Filter
EQN …….. Equation

FAA……... Federal Aviation Authority
FOV……... Field Of View

GA……. General Aviation
GLSDC…..... Gaussian Least Squares Differential Correction
GPS…… Global Positioning System

IMU…..... Inertial Measurement Unit
INS……. Inertial Navigation System

KAMS…… Ka Multifunctional System
KF……..... Kalman Filter

LED……Light Emitting Diode
LHM……...Lu, Hagar and Mjolssness
LR…….. Literature Review

MAC…….. Mid Air Collision
MIDAS……...Multifunctional Infrared Distributed Aperture System
MOS…….. Metal Oxide Semiconductor
MV..... Machine Vision

NED……... North East Down

PIF-NZSP-CRW..... Proportional Integral Filter optimal Nonzero Setpoint with Control Rate Weighting

RAF……Royal Air Force
RDV……... Rendezvous
RF…….. Radio Frequency
RGB……... Red Green Blue

S&A……... See and Avoid
SARSE……... Subtended Angle Relative Estimation
SNR……....Signal to Noise Ratio

TCAS……. Traffic Collision Avoidance System
TSP……Travelling Salesman Problem
TTG……Time to Go

UAV……...Unmanned Aerial Vehicle
UKF……... Unscented Kalman Filter
UV……..Ultraviolet
USAF……. United States Air Force

W.R.T……..…With Respect To

Notation:

N…...…….Noise

S.……... Short noise

I_D……... Dark Current

N_D ...…….. Dark Current noise

N_C …….Circuit Noise

N_S ……. Photon Short noise

i_ρ^o ……..…….. Line of sight unit vector (optical camera to target)

i_x, i_y, i_z ……. Individual components of line of sight unit vector

ψ ……... Azimuth angle measured from camera focal plane

θ …… Elevation angle measured from camera focal plane

φ ...……..Roll angle measured from camera focal plane

ν_ψ ……. Azimuth noise vector

ν_θ …….. Elevation noise vector

ν_o^o …….. Optical camera noise vector

X_n, Y_n, Z_n …. Earth fixed inertial axis system

X_b, Y_b, Z_b …. Body axis system

X_d, Y_d, Z_d ….Initial offset between drogue and receiver probe

R.……... Range between leader and follower

X_L, Y_L, Z_L ….Coordinates along inertial axis for leader

X_F, Y_F, Z_F ... Coordinates along inertial axis for follower

D…….. Diameter

ρ …….. Relative Range

θ_{pixel} ……..Angular size

θ_{FOV} ……..Cameras field of view

f……. Cameras focal length

n.……... Noise vector

b…… Target/leader size

r ……Relative distance

r^n …….. Position vector of leader/target relative to follower in navigation frame

v^n …….. Position vector of leader/target relative to follower in navigation frame

a^n …….. Position vector of leader/target relative to follower in navigation frame

X, Y, Z ……...Forward, lateral and vertical displacement

U, V, W …….. Forward, lateral and vertical velocity

a_{lat} …… Target/leader lateral acceleration

a_{long} …….. Target/leader longitudinal acceleration

t_k ……... Time step

L_c …….. Known camera attitude represented by a rotation matrix from inertial frame to a camera frame.

h…… Target/leader position in image frame

a_{Veh} ……... Vehicles acceleration in inertial frame

$\hat{x}_k^-$ and $\hat{x}_k$ …. Estimated and updated state x

P_k^- and P_k …. Estimated and updated error covariance matrix

Subscripts

c……. Camera

v…….Velocity

L…… Leader

F…… Follower

l……..Left

r…….Right

k…… Initial time

k+1…… Updated time

o0o- Intentionally left blank -o0o

1) Introduction:

This thesis outlines the development of a method of navigation enabling a follower UAV to fly aft of a leader/target (such as a re-fuelling drogue) by means of a mounted camera using only the visual input of the leader/target's 3D position. Reasons for using a vision based system can be attributed to the Commercial Off The Shelf (COTS) availability of the key components. The benefits of such a system of navigation include, firstly, the potential for autonomy of the system (there is no need for a Global Positioning System (GPS)) and, secondly, the ability of the UAVs to undertake a mission in complete radio silence; both of which increase potential survivability in a hostile environment.

The author's work has been to initiate the project, which is aimed at ultimately progressing into an open atmosphere test in order to prove the system's capability using the departments' two Piper Cub (scaled model) aeroplanes. The project was performed under the supervision of Dr A.K. Cooke with the support of (an assistant supervisor) Dr S.E. Hobbs. The author was able to take advantage of a previously developed program from (Hobbs, 2003), utilising captured images of the leader/target from a *Eyecam*© camera (for manufacturers specifications see figure A3.1 in appendix 3). The study employed a built in pose algorithm which was able to estimate the *Eyecam*© cameras' pose and LED's were placed at known reference points on the target aircraft in order to illuminate the target against its background. This enabled the follower's camera (the *Eyecam*©) to capture images containing sufficient pose information for image post-processing to enable formation flight.

It should be noted that a significant proportion of the time allocated for this project was devoted to practical experimentation, notably in the visual system configuration. In fact, altogether three experiments were performed, with the final experiment leading to pose estimation results that proved the initial system concept. The work presented can be divided into two areas, the first relating to background research and formulation of the problem and the second including the experimental work performed by the author.

The initial *Literature review* relating to the machine vision and autonomous navigation topic is presented in *Chapter 2*. A further background search into the interactions of light emitted in the atmosphere and the principles behind digital photography can be found in under the *Machine vision* heading in *Chapter 3*. *Target Identification*, (*chapter 4*) discusses target labelling, reference axes and formatting from a distance. *Chapter 5* leads on from this to *Pose estimation* which addresses the problem of determining a follower UAV's position and pose relative to a target. Current pose algorithms are also discussed and finally the proposed solution using the **Mfitvid** program developed at Cranfield University by (Hobbs, 2003) is presented.

Chapter 6, Testing outlines each of the three experiments performed along with corresponding experimental results, discussions and conclusions. An *Overall Discussion* of the work carried out during this thesis is made in *Chapter 7*. *Chapter 8, Thesis Outcome*, summarises the key theoretical and practical work completed during the project while concluding remarks resulting from the current work are listed in the *Overall Conclusion Chapter 9*. Finally, *Chapter 10, Future work* contains suggestions which a future project within the same domain should address in order to continue and develop the current work.

2) Literature review:

The purpose of this *Literature Review* (*LR*) was to enable the author to gain an initial understanding and insight into the project, titled "Machine Vision and Scientific Imaging for Autonomous Air Vehicles (UAV)". Following the *LR* the core body of further in-depth research and the necessary practical aspects required to advance the project were realised. The *LR* was a constant process featuring throughout the duration of the project in order help the author to understand the issues and clarify where best to apply the most current and relevant techniques available.

The mission statement for the scope of this project is: *to achieve a robust solution enabling a follower UAV to keep in formation flight with respect to a lead aircraft using* (*solely*) *machine vision throughout the duration of a mission envelope*.

A structured approach to performing the *LR* was taken by the author and the research was organised under the following categories:

- 2.1. Current UAV capabilities: endurance, range, uses
- 2.2. Current research involving UAVs : new roles, regulations
- 2.3. Calibration of digital cameras: how to calibrate,
- 2.4. Current pose algorithms: techniques, robustness, marker requirements

2.1 Current UAV capabilities:

During the past few years there have been marked developments in both the capabilities and performances of Unmanned Air Vehicles (UAV's). Initially, arising from the military requirement of reconnaissance; UAV's such as the USAF "Global Hawk" and the newly deployed RAF "Reeper" (Gardener, 2008) have become capable of providing an effective projection force within hostile territory. Civilian applications of UAV technology have followed suite, with off-shoot applications such as offering local communication and data transfer coverage and atmospheric data measurement (to give a few examples).

Already projects are taking advantage of Commercial Off The Shelf (COTS) equipment by constructing low cost UAVs with surveillance capabilities. COTS equipment enables UAV development to be speeded up through the purchase of fully equipped hobby airframes, aircraft autopilots, cameras, video imaging software and data linking software (Ma et al., 2006) and as a result of such capabilities control algorithms can be tested much more easily in open atmosphere. Furthermore, this last paper underlines the advantages of small COTS UAVs being inexpensive to build and perhaps more importantly easy to repair.

Figure 1[a] An image of the MQ9 "Reeper".

[a] Taken from Defense industry daily, www.defenseindustrydaily.com

2.2 Current research involving UAVs

UAV technology is constantly advancing. However, the benefits of removing a human pilot from the cockpit have lead to new limiting factors in keeping a UAV airborne; notably with respect to fuel and engine oil reserves. As a result, current research is dominated by addressing the need to re-fuel in-flight in order to further extend a UAV's mission endurance. This aerial refuelling can be separated into two types: "boom operated" (as employed by the USAF) or "basket and drogue" (the most commonly used method) (Campa et al., 2007) see figures 2 and 3 below. The first requires the pilot to fly the aircraft within a designated 3-dimensional box below the tanker aircraft at the same time as a boom operator "flies" the boom into the fuel receptacle while the latter requires the pilot to successfully dock a drogue into a basket attached to a fuel hose trailed from the tanker aircraft. The difficulty of accurately measuring the pose of the lead aircraft highlights the limitations of GPS due to possible local interference; therefore, LASER, Infrared (IR) and Machine Vision (MV) solutions are also being investigated. Using MV has the distinct advantage of radio silence which is important during a covert operation.

Figures 2[b] and 3[c] Illustrating boom refuelling and probe and drogue refuelling.

[b] US Air force photos webpage, www.af.mil/photos/
[c] Figure 1, (Kimmett et al., 2002)

Research into mimicking natural animal behaviour such as flocking and swarming and their possible application to future UAV formation flying is presented in (Crowther, 2003). Figures 4 to 6 below illustrate two of the rules/situations modelled using computer animation in order to test the developed flocking rules. It should be noted that there is a difference between formation flying and flocking. The latter having no specific order allows the flock members to change their position and this enables the flock to manoeuvre in a fluid like manner, with each member capable of turning at their maximum rate or radius unlike the steady rate of turn required for formation flight.

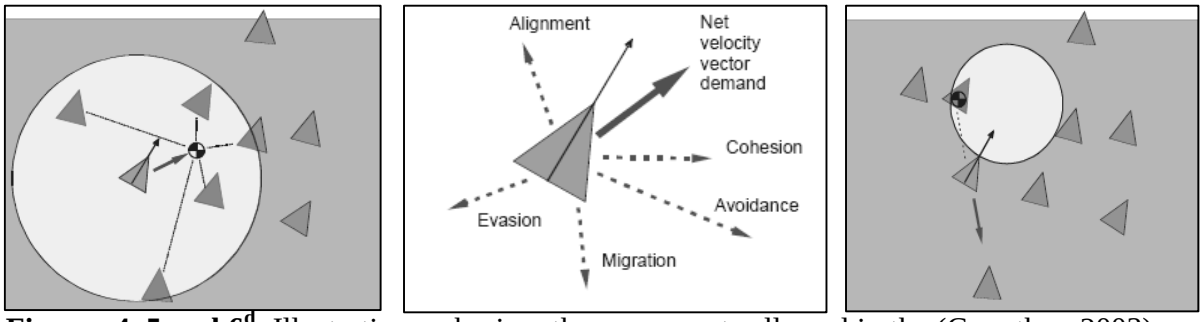

Figures 4, 5 and 6[d]: Illustrating, cohesion, the movements allowed in the (Crowther, 2003) simulation and evasion.

One has only to look up into the sky and observe the "V" flying formation that is adopted by migrating birds during long distance travel to appreciate its potential significance. Scientific analysis of this behaviour has highlighted the beneficial downwash interference developed by horse-shoe vortices trailing from the birds' wing tips, hence reducing the total effort required by the flock to fly. Therefore, it is possible to envisage an eventual requirement for several UAV's to fly autonomously in formation behind a leader (manned or unmanned). However, the development of a means of following a manoeuvring leader poses additional problems which conflict with the requirements of holding a steady position as required during re-fuelling. Ultimately, the need to rapidly respond to the uncertainty in the leaders' flight path prevails in all circumstances.

[d] Figure1, (Crowther, 2003)

Finally, the introduction of UAVs into manned airspace necessitates that the level of safety in avoiding a Mid Air Collision (MAC) is equal to or is better than that of manned planes. A UAV is therefore required to substitute a pilot's vision and intellect in being able to deal with a potential MAC scenario. Current work sponsored by the USAF relating to Autonomous Flight Control Sensing Technologies (AFCST) for a See and Avoid (S&A) system is presented in (Chen and O'Neil, 2003). Development of two sensors: 1) Multifunctional Infrared Distributed Aperture System (MIDAS) and 2) Ka Multifunctional System (KAMS) are discussed alongside the Time To Go (TTG) model developed and used to simulate the UAVs' encounters with various category aircraft. TTG criteria are divided into two time regions: > 43 seconds to perform a standard TCAS de-confliction manoeuvre and > 8 seconds for an aggressive last ditch attempt.

Particular emphasis is placed on using speed ratios between ownship velocity and the threat aircrafts' speed. Trajectories for the conflicting flight paths are shown in figures 7 and 8 below, these illustrate the increased visibility necessary for increased velocity difference between the two aircraft.

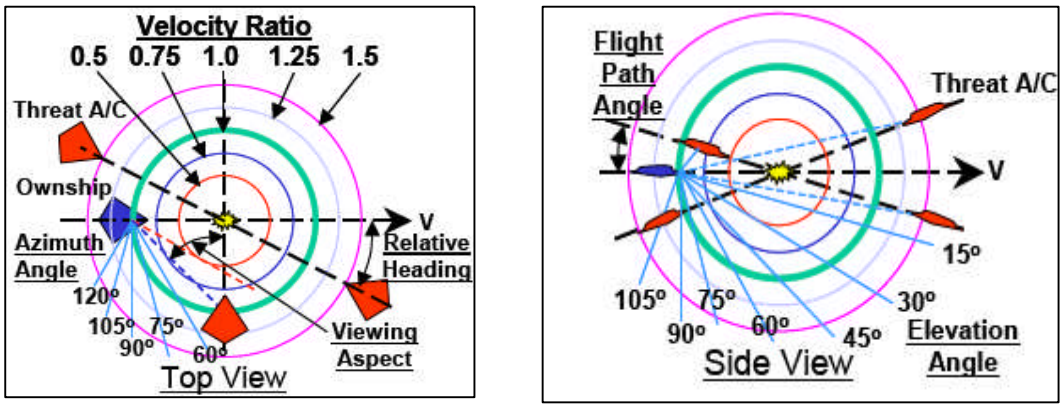

Figures 7 and 8[e]: illustrate the MAC threat posed by conflicting trajectory path angles and velocity ratios for ownship trajectory with respect to other aircraft.

[e] Figure 2, (Chen and O'Neil, 2003)

According to FAA statistics 88 % of MACs are due to a blind area located under the nose; which for a UAV poses no issues for a possible sensor location. The worst case scenario predicted by (Chen and O'Neil, 2003) is for a head on collision with a General Aviation (GA) aircraft at 3 nm. Thus, the sensor Field Of View (FOV) is crucial to providing adequate MAC coverage. In order to achieve 94 % coverage, 100° elevation (± 50°) and 200° azimuth (± 100°) visibility are required. However, reducing the FOV to 60° (± 30°) elevation by 120° (± 60°) azimuth significantly reduces the coverage to 67 %. The paper suggests that only frontal hemisphere coverage is required to protect against slower oncoming aircraft but that a 4π coverage (± 90° horizontally and ± 90° vertically) is necessary for faster than ownship (such as fighter aircraft) coverage.

2.3 Calibration of digital cameras:

Geometrical camera calibration has the aim of mapping 3D "real world" co-ordinates into 2D row and column image co-ordinates. Several methods exist and have been analysed by (Heikkila and Silven, 1997) who highlighted the *classical approach* of minimising a non-linear error function, a *two-step* method where initial parameters are evaluated linearly followed by a final non-linear minimisation before finally presenting their *four-step* calibration. The latter produces, firstly, a closed-form solution using Direct Linear Transformation (DLT), then a non-linear parameter estimation with an optional third step depending on the control point projection size and a final fourth step which solves the image correction problem. However, two distinct camera models can be outlined:
1) the "Pinhole" camera models, which neglect any optical distortion and 2) the more complicated models which include lens distortion (Motta, 1999).

DLT is a procedure best described by the "Pinhole" camera method in which collinearity between each point object in space draws a straight line through to the centre of the image plane. It must be noted that the *Z*-pane of the camera is kept perpendicular to the image plane. Linear transformation is then obtained by ignoring the non-linear radial and tangential components and by using a 5^{th} order correction polynomial which compensates

for the non-orthagonality errors for the image co-ordinates. Using a linear transformation has the disadvantage of excluding the lens distortion promoting errors. This can be reduced by computing the camera correction parameters iteratively.

A more in-depth understanding of calibration errors of digital cameras can be gained from an earlier paper (Heikkilä and Silvén, 1996) which introduces the two types of error: *Random error* such as in nature or *Systematic error* for example, those arising from calibration, geometrical distortions and illumination. The article highlights the fact that errors due to the measurement procedure are not accounted for in the majority of calibration reports. Quantization noise, caused as a result of the finite spacing of the CCD arrays can reduce the precision to which a point object (such as a dot) can be captured.

One solution is to detect the centroid of the point using an image extraction algorithm which by converting the image into binary code enables each pixel to be weighted thus returning a normalised grey scale value and hence improving the resolution (see figure 9 below). In addition, variations in readings can be seen by changing the illumination condition. Colour aberration occurs due to the difference between point detection under fluorescent (blue spectrum) and halogen (red spectrum) lighting. Intensity in local dot centres are shifted due to the non-uniform lighting conditions and therefore constrains the acceptability of the results to those obtained under the same light conditions as the calibration. This last point will need to be considered for the application of MV to UAVs.

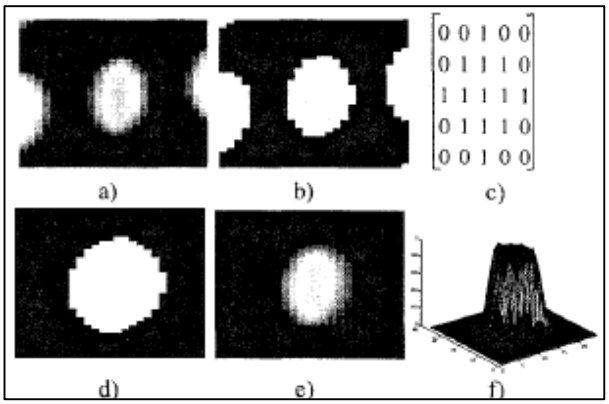

Diagram 9[f]: illustrating the improved image (a to e) via a binary image (c) used in determining the image centroid weighting.

Another method of camera calibration is presented in (Hobbs, 2003) , where the author has chosen to use a 3rd order polynomial which adequately adjusts the distortion in the camera model. The procedure of calibrating two different makes of digital cameras is presented and the evaluated errors in vertical and horizontal directions are quantified. These calibration values are to within the same order of magnitude as that of the measurement noise.

The MV problem can be best described as an optical-physics problem in which the camera's lens needs to focus the image containing the targets markers onto the CCD chip producing the *row* and *column* numbers needed for the pose algorithm. The calibration step is a means by which of converting the CCD read out into useful angles of pose: elevation, rotation and yaw.

[f] Figure 2, (Heikkilä and Silvén, 1996)

2.4 Current pose algorithms

Manoeuvring, the UAV using MV requires the onboard avionics to be able to transform the visual cues into useful flight dynamic data to control the UAVs flight path. Pose algorithms are a means by which the useful visual data is converted into required data for the control commands of the UAV. The visual cues required are in the form of markers located at known positions on the lead aircraft. This topic is at the centre of a considerable amount of current research and many sources are available. For example, (Valasek et al., 2005) proposes a *Vis Nav* system which works on the principle of a Position Sensing Diode (PSD) that receives light emitted from markers on the lead aircraft after which the navigation solution is obtained from a Gaussian Least-Squares Differential-Correction (GLSDC) iteration routine.

(Johnson et al., 2007) outlines two MV algorithms which can be performed using a single camera: 1) Centre Only Relative State Estimation (CORSE) and 2) Subtended Angle Relative State Estimation (SARSE). CORSE requires the "follower" to fly a meandering sinusoidal path before generating an optimum trajectory relative to a target using minimal processing power while SARSE requires rigorous image processing without the "follower" having to fly a prescribed path. Both methods yield comparable accuracy for range to target estimation. The use of image processing features in both the methods with active contours used to calculate the centre of the target aircraft for CORSE whereas SARSE draws on the additional information of the distance between the wingtips and the angle subtended between the wing tips. Extended Kalman Filtering (EKF) is applied to resulting data from either algorithm to provide state estimates of velocity and position with respect to the target aircraft.

A similar approach to the EKF above is presented in (Johnson et al., 2007) where images of the target are processed to determine azimuth, elevation and subtended angle. Only three target points are chosen: centre point, left and right wing tips. The centre point enables azimuth and elevation angles of the target to be determined with the wing tip points enabling the follower aircraft to be sized. Using this information the relative target position, velocity, target size and acceleration are determined using an Unscented Kalman Filter (UKF) because of the high non-linearity of the tracking. The algorithms have only been used to post process flight test data offline and therefore some reservations are placed on real time vision capabilities but the research is still being carried out and the algorithms still being refined.

Another approach of using infrared markers is proposed by (Pollini et al., 2005) who specifically targets the UAV re-fuelling capability requirements. The Lu, Hager and Mjolsness (LHM) pose algorithm is chosen because of its rapid execution speed which enables real time evaluation, permitting the UAV to follow the "lead" aircraft. The sole use of the algorithm is envisaged to keep the UAV in formation flight behind the lead aircraft during re-fuelling. However the drawback of using LHM is that each marker needs to be identified in each image frame, the LHM algorithm also has no guaranteed number of iterations before converging. Furthermore, marker geometry is important in this situation and in order for the LHM algorithm to work effectively, it necessitates a convex polygon formation (figures 10 and 11 below) without which the algorithm fails.

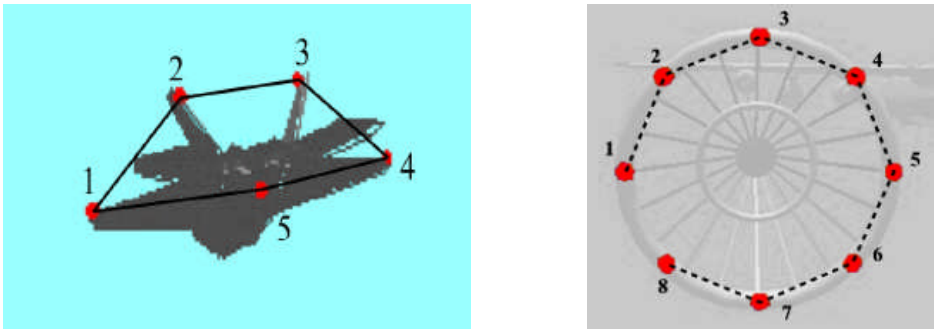

Figures 10 and 11[g]: Illustrating the convex polygons and numbering for the TSP.

[g] Figure 2 and Figure 3, (Pollini et al., 2005)

The numbering of the infrared LEDs in each image required for the LHM algorithm is calculated by a Travelling Salesman Problem (TSP) algorithm, however this algorithm is also limited by the perception of the LEDs via the camera. A solution to this problem is to put the LEDs in a line with a reference point below; lines then drawn from each LED to the reference point construct a fan, with the angles corresponding to the location of the wing tips of the lead aircraft. This solution is not suitable for large *yaw* (ψ) angles though these are unlikely to occur during steady level flight as required for re-fuelling and formation flying. Finally, successful experimental work on attitude and relative displacement estimation using the LHM algorithm and infrared LEDs has been done both indoors and outdoors.

o0o…o0o…o0o

o0o- Intentionally left blank -o0o

3) Machine Vision:

The experimental aspect of the project was conducted using cameras already purchased within the department. Two Radio Frequency (RF) "*Eyecam*" cameras were made available for use (see appendix 3 figure A3.1 for detailed specifications) and are referred to throughout this thesis as either **Yellow dot** with a 2452MHz RF (this was the principle camera used) or **Green dot** with a RF of 2473MHz. These cameras are designed for recreational use and are commercially available off the shelf.

Initial experiments were required in order to calibrate both the cameras. These are discussed later in chapter 6 and additional supporting work can be found for experiments 1, 2 and 3 at the end of the appendix section. The most important property of the cameras is their ability to map/convert correctly the 3D world to a 2D image with minimal distortion or skew. Their second most important property is their ability to filter correctly different colours into Red, Green and Blue (RGB) as required for specific colour identification in the post image capture processing. This last point will be necessary when automating the LED beacon position (*row* and *column*) tracking for input into the pose estimation software.

3.1) Light in the Atmosphere:

An underlying requirement for the Machine Vision application in this research is the ability of the follower UAV to adequately distinguish the target UAV from the surroundings. In keeping with the passive navigation capability of the UAV, the use of light beacons to mark points on the leader has been chosen. During the literature review the author identified the omission of atmospheric properties relating to the visual navigation problem. Therefore, it is necessary to gain an understanding of the properties which occur between the light source and the camera i.e. the effect of the atmospheric particles along a path of light (Nishita, 1987). This effect is described as: *Atmospheric Light Transmission and Attenuation*. However, a majority of the information regarding this topic is principally concerned with astronomy and thus lies out of the scope of this study.

The visual spectrum has been chosen as this is readily accessible with the use of basic Off-The-Shelf equipment such as cameras and LEDs. Figure 12, below illustrates the electromagnetic spectrum, with the visual spectrum ranging from shortwave *Blue* light to longer wavelength *Red* light.

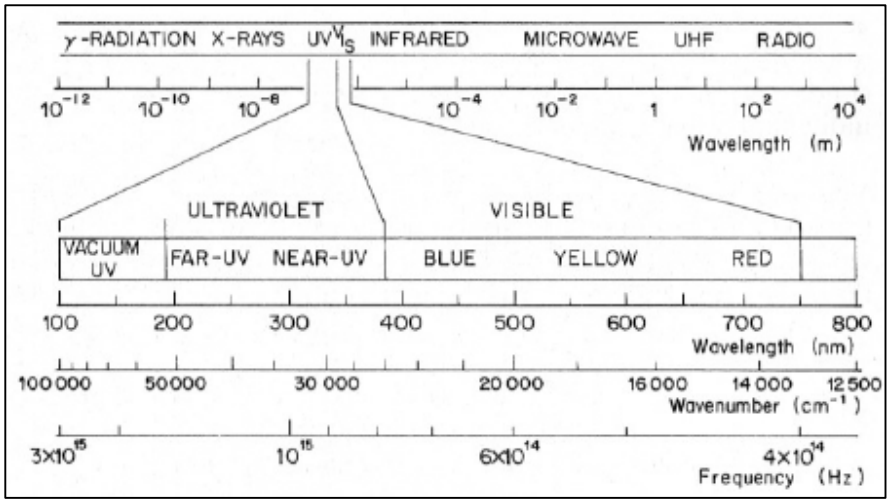

Figure 12[h]: The Electromagnetic spectrum.

The properties of light, such as its colour and intensity can be altered by three key interactions within the atmosphere:

1) *Attenuation* / *Scattering*
2) *Absorption*
3) *Emission* / *Background Radiation*

Out of the three, light scattering is the most pertinent interaction due to the number of suspended particles present in the atmosphere (Narasimhan and Nayar, 2002). In order to better understand this, a list of particle sizes for different weather conditions together with their concentrations is summarised in table 1 below.

Condition	**Particle type**	**Radius** (μm)	**Concentration** (cm^{-3})
Air	Molecule	10^{-4}	10^{19}
Haze	Aerosol	$10^{-2} – 1$	$10^{3} – 10$
Fog	Water droplet	1 – 10	100 – 10
Cloud	Water droplet	1 – 10	300 – 10
Rain	Water droplet	$10^{2} – 10^{4}$	$10^{-2} – 10^{-5}$

Table 1[i]: Weather conditions and associated particle types.

[h] Fig1.1a, p8, (Denny, Ronald C. and Sinclair, R., 1987)
[i] Table 1, (Narasimhan and Nayar, 2002)

From table 1, above, the effects of particle size of different weather conditions on light transmission can clearly be seen. For instances, air molecules are much smaller than the visible light wavelength and therefore will have a minimal effect. Haze however, consists of aerosol particles which are suspended in the atmosphere such as: volcanic ash, combustion products and sea salt. These particles can act as nuclei for water particles when the humidity is high, therefore, producing obstacles for light transmission. Fog and cloud have similar properties though fog only occurs at low altitudes. The intermediate stage during condensation build up between Haze and Fog is termed Mist. The formation and effects of rain and snow are much more complex and beyond the scope required for this initial investigation.

Another key point is the amount of *background luminance* present (Norris et al., 1999). This is the amount of ambient light which forms the backdrop against which the light source will be viewed. As a result, during daylight when the background is bright, it is difficult to detect the difference between an emitting light and its background. The majority of this *background luminance* is caused by solar radiation in the visible near-IR (1.5μm.) and mid-IR (3-5μm.). It should also be noted that the Earth's atmosphere absorbs solar background radiation in the Ultraviolet (UV) region below 0.285μm (which is termed the solar blind portion of UV radiation).

Further information regarding the atmosphere's optical properties can be found in the research report of (Elterman, 1968). This paper outlines the first two key interactions (*Attenuation* and *Absorption*) as discussed previously, summarising their effect on UV, Visible and IR light. The *Attenuation* parameters are determined using *Rayleigh* scattering cross-sections (N.B. Rayleigh scattering is isotropic) with molecular number densities from the standard atmosphere tables. *Absorption* parameters are derived based on Vigeroux's coefficients which are then applied to representative atmospheric distributions. The research compares seven sets of aerosol measurements with altitude which enables a profile of atmospheric *Attenuation coefficient* with altitude to be established. Aerosol *Attenuation* is a strongly fluctuating parameter and therefore, an average representative profile has been

created with measurements through both the troposphere and stratosphere. A summary of the data for the *Red*, *Green* and *Blue* wavelengths can be found in table 2 below.

Colour	h (km)	β_r (km^{-1})	r_r (0-h)	β_p (km^{-1})	r_p (0-h)	β_3 (km^{-1})	r_3 (0-h)	β_{ext} (km^{-1})	r_{ext} (0–h)
Blue, 470nm	0	5.89E-03	0.000	1.42E-01	0.000	2.21E-04	0.000	1.48E-01	0.000
	5	3.54E-03	0.023	4.50E-03	0.180	1.37E-04	0.001	8.19E-03	0.204
	11	1.76E-03	0.039	2.67E-03	0.199	2.85E-04	0.002	4.71E-03	0.239
Green, 568nm	0	2.64E-02	0.000	1.80E-01	0.000	1.25E-05	0.000	2.06E-01	0.000
	5	1.59E-02	0.104	5.72E-03	0.228	7.73E-06	0.000	2.14E-02	0.332
	11	7.87E-03	0.173	3.38E-03	0.252	1.61E-05	0.000	1.13E-02	0.425
Red, 660nm	0	1.16E-02	0.000	1.58E-03	0.000	3.28E-04	0.000	1.70E-01	0.000
	5	6.99E-03	0.046	5.02E-03	0.200	2.03E-04	0.001	1.22E-02	0.247
	11	3.46E-03	0.076	2.97E-03	0.221	4.23E-04	0.003	6.85E-03	0.300

Table 2[j]: Atmospheric properties for selected wavelengths

Where:

β_r = Rayleigh attenuation coefficient, r_r = Rayleigh optical thickness,

β_p = Aerosol attenuation coefficient, r_p = Aerosol attenuation coefficient,

β_3 = Atmospheric ozone absorption coefficient, r_3 = Ozone optical thickness,

β_{ext} = Extinction coefficient, and r_{ext} = Extinction optical thickness.

The extinction coefficient enables all three light waves to be compared with the sum of all the attenuating factors for the respective wavelength. The larger the coefficient the more the light intensity decreases with distance from the source. From table 2 it can be seen that the attenuating factors act the least for *Blue* wavelengths for low altitudes (0 and 5km). However, at higher altitude *Red* wavelength light is the least affected light.

[j] Data taken from tables 4.9, 4.11and 4.13 (Elterman, 1968)

When selecting the specific LEDs to be employed it is necessary to consider the wavelength of light being applied and the sizes of the particles with which it will interact within the atmosphere. Therefore, for the initial ground trials the author selected four **5*mm* Superbright *Red* Kingbright LEDs L-53SRC-DW** (see appendix 1 for further LED specifications) which from the manufacturers data are quoted to emit a *Red* light with a Peak wavelength of $660 \times 10^{-9}\, m$. Their light intensity is quoted as ranging from 1600 to 2000mcd (0.428 Lumens) and could be run of a 9V *PP3* battery. These LEDs were selected as they were easily and readily accessible from local electronic suppliers, but more importantly their performance enabled them to perform initial testing satisfactorily.

3.2) Digital Cameras:

Digital cameras permit a hardware-software interlink and are ideally suited for the MV application. Since research into Digital cameras / Charged Couple Device (CCD) imaging began in the early 1970's (Graham, 2005) p49, CCD imaging has progressed to the point where there is now a wide selection on the market for all levels of users especially for research purposes. The CCD imaging capabilities on offer are reflected in the wide range of respective unit costs. Trade-offs between image quality, spatial resolution, colour fidelity and dynamic range account for these varying product prices. The use of CCD imaging requires a computer in order to provide an interface to interrogate the images and perform post-photo image processing. The computer has therefore replaced the need to develop photos using chemicals and special dark rooms enabling photography to become more accessible and most importantly it has reduced the time it takes between capturing an image and being able to retrieve it.

3.2.1) CCD Arrays:

The process used in capturing a digital image relies on the use of semiconductors which are a form of solid state electronic components. The most common semiconductor used in CCD arrays is the *Metal Oxide Semiconductor* also known as MOS which is made up of an aluminium gate over a dielectric metal and placed on a silicon substrate. The CCD consists of many MOS's spread over the circuit (see figure 13 below).

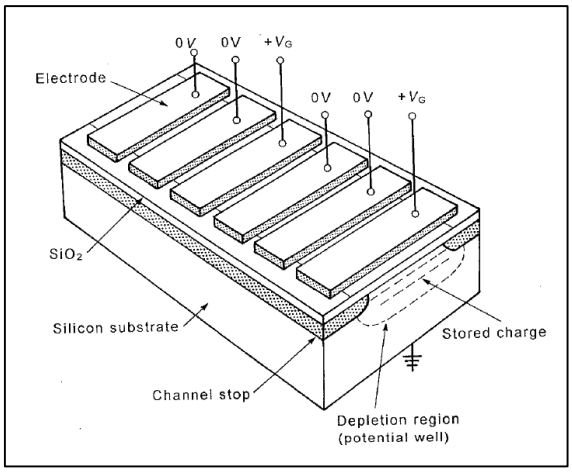

Figure 13[k]: An example of a CCD array structure.

When light is captured by the MOSs', they act as electrodes on the surface of the device, and a charge forms under the electrodes with the highest potential which then attracts electrons from the silicon substrate below. The information within the image is therefore stored in the form of electrical charges. The *Charge Coupling* (CC) occurs during the transfer of the image's information via sequential pulsing of the electrode voltages, enabling the image to be transferred through the array of MOSs with only small losses and minimal noise/interference.

The CCD array can be seen as a set of storage elements (individual pixels), with each element capable of capturing light. The amount of light which can be captured by the element is quoted as the "fill factor" in percentage terms. When an image is captured each individual element will receive an amount of light which will be transferred into electric charge and then passed from array to array using CC. A CCD circuit is made up of several rows of arrays (figure 14 below).

[k] Figure 4.4, p49, (Graham, 2005)

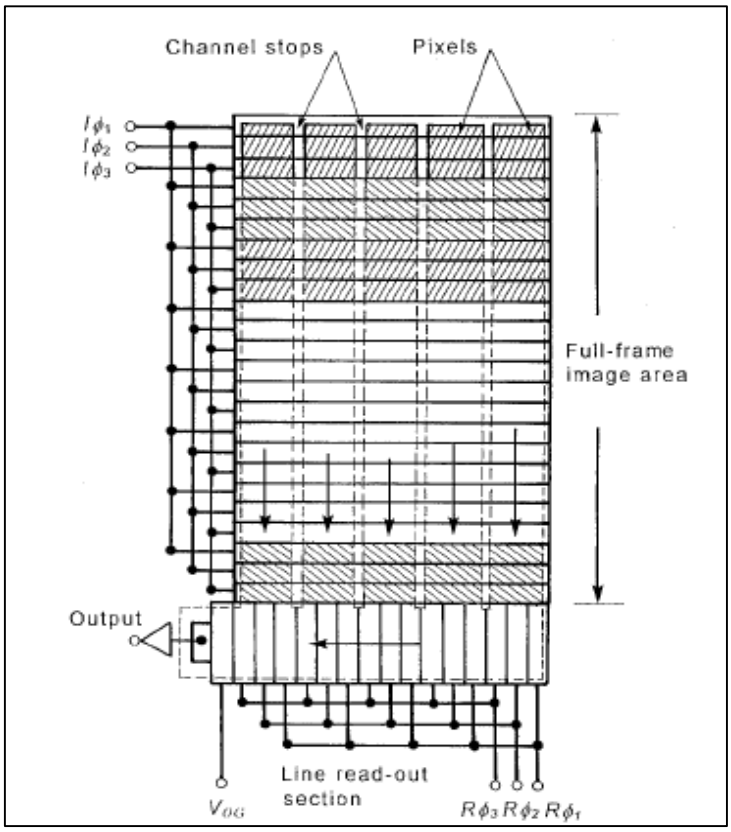

Once the information (in analogue form) reaches the end of each line / array it is transferred to an "output register".

The Analogue to Digital conversion (A/D) is performed as follows:
"The required input voltages are the upper and lower reference voltages, the voltage to be measured and a clock pulse.

Figure 14[1]: The CCD array illustrating information transfer.

The A/D converter comprises of a series of binary voltage comparators supplied with the input signal and a reference voltage which is scaled between the low and high values. At each clock pulse the comparators are simultaneously read and a binary code is then generated." (Graham, 2005)p55, this step is often referred to as image *quantization*.

[1] Figure 4.11, p58, (Graham, 2005)

3.2.2) CCD Noise

This can be accounted for by three main sources:

i) *Photon short noise*: this is the random arrival and absorption of photons during the charge generation. The Signal to Noise Ration (SNR) for sensed images is at a maximum when pixels are close to their full capacity of 10^6 electrons and is given as: $N_S = \sqrt{S}$ where S = short noise.

ii) *Dark current noise*: this is generated at the exposure and read-out phases at a rate proportional to the absolute temperature (K) of the sensor material. Therefore measuring the dark current (I_D) the dark noise can be given as: $N_D = \sqrt{I_D}$.

iii) *Circuit noise*: this accounts for the largest noise in the circuit (N_C) due to the onboard circuit amplifier which is required to amplify each pixel to register a useful reading. After each pixel is read-out, the amplifier must be reset to zero and therefore an uncertainty of the recovered zero level exists. This is known as the *rest noise*.

The sum of all three enables an estimate of the total noise (N) in the CCD:

$$N = N_S + N_D + N_C \qquad \ldots \text{(eqn 3.2.1)}$$

Furthermore, the SNR can be defined as: SNR = S/N. Which for practicality is measured using a log scale: $\text{SNR} = 10\log(S/N)\text{dB}$ … (eqn 3.2.2)

3.2.3) Complementary Metal Oxide Semiconductor (CMOS):

Similar to CCD, CMOS functions on the same principle of capturing light in an array and storing the information as an electric charge. The main difference between the two technologies lies in the fact that a CMOS circuit requires only one chip to perform the same task that a CCD chip does with three (required to capture Red, Green and Blue individually). Certain CMOS sensors have an amplifier for each pixel, termed *Active Pixel Sensors* (*APS*). The basic design consists of the photodiode, which converts incident light into an electric charge, a charge to voltage converter, a reset and select transistor and an amplifier. Above the CMOS sensor is a grid of metal connectors which is used for timing and signal read-out. Due to the fact that pixels in CMOS imaging arrays are read out in parallel (row by row) there is a read-out speed advantage over CCD.

3.2.4) Image File Formats:

A list of the most common image formats and their abbreviations follows:

BMP – Windows compatible bit-mapped graphics image
DIB – Device independent bit-map
EPS – Encapsulated post script
JPEG – Joint Photographic Experts Group, Discrete Cosine Transformation (DCT)
PICT – Mac supported image
TIFF – Tagged image file format

A Bit-mapped image: is composed of a series of dots (pixels) as opposed to lines. It consists of a grid of discrete pixels of grey or colour values. Each pixel is stored as a binary number with an (x, y) address which maps to a pixel located in the monitor display. Resizing a bit-mapped image without distortion or aliasing is problematic as it requires large amounts of computer memory.

Object Orientated (vector) graphics: the image is defined mathematically rather than by a set of dots which results in a more economical use of computer memory. Thus circles and squares can be reproduced without any aliasing or distortion, requiring much less computer manipulation. These images are mainly used for drawing and CAD.

3.2.5) Spatial filtering:

Digital image processing is facilitated by quantization of pixels into the binary scale (usually to a capacity of 8-bits) image brightness levels (grey or colours) on a scale of 0 to 255. This is performed by analysing the Digital Number (DN) assigned to various pixels, either by interpolation or filtering in the spatial domain. A number of re-sampling methods can be used to assign appropriate output DN with three forms of convolution: Nearest Neighbour, Bilinear and Bicubic. Spatial filters are employed mainly for improving edge detection/definition thus increasing image sharpness and noise reduction.

3.2.6) Image compression:

The data contained within a digital image can often be very large depending on pixel resolution for image quality, with typical high resolution values ranging between 18 to 25 Mb. The use of image compression reduces the number of image bits by a certain degree while making sure that the image resolution remains acceptable. This is done by grouping together large areas of common colour or tone. Compression ratios of 20 or 30 to 1 give satisfactory results. The most common techniques include reducing: 1) Repetition of data, 2) Redundancy in coding of data, 3) Redundancy between adjacent pixels and 4) Psycho-visually redundant information. The first three techniques are loss-less and the fourth utilises *lossy* compression techniques such as JPEG – Joint Photographic Experts Group (standard compression). JPEG is designed to discard information from the image not easily seen by the naked human eye.

4) Target identification:

In order to follow a lead aircraft or perform in-flight refuelling a reliable method capable of successfully identifying and distinguishing the target in front of the UAV is required. As outlined in the literature review (chapter 2), the ability to perform this operation using MV as an alternative to radio communication will enable the benefits of using low cost and light weight cameras such as an *Eyecam*© (two of which are already available within the department) to be realised. Furthermore, the additional advantage of navigating a UAV using vision provides a covert capability, useful for operating in hostile airspace since no information relating to either the leader's follower's position needs to be broadcasted. In order to achieve this, it is necessary to design and place suitable markers at known positions on the leader or target which will then act as reference points to be used in determining the pose of the follower.

4.1 Labels and markers:

The use of *passive* markers is required since there is no interaction/data transfer between the marker and the capturing device (e.g. camera). The choice available for such markers can be divided into the following two categories:

- *Non-emitting sources*: Labels, coloured dots and specific aircraft geometry
- *Emitting sources*: Lights, LEDs, visible (different colours), infrared and intermittent/pulsed

Initial research performed by the author focused on using *non-emitting sources* using suitable patterns of red coloured dots for use as reference point markers (see appendix 2). This study investigated the number of unique patterns/labels that could be made using 1, 3, 4 and 5 red dots. The individual patterns were printed, fixed to a cardboard backing and then attached to reference points on the target (the Piper cub model) to determine their suitability for use as markers. However, the difficulty of identifying the non-emitting labels as a result of poor background lighting was highlighted following a trial using the

Eyecam©. Subsequently, these patterns could be replicated using LEDs, thus enabling the camera to better cope with poor lighting conditions.

Having established the need for using an *emitting source* the next step was to determine which type of source was best suited for the project. Firstly, the choice between visual and IR needed to be made. Examples using IR were found in both (Pollini et al., 2005) and (Valasek et al., 2005). (Valasek et al., 2005) identified the need to also modulate the IR light emitted to 40*Hz* in order to filter out any natural and artificial light sources for use in their *Vis-Nav* system. On the other hand, (Pollini et al., 2005) used only the narrow transmission band of the IR LED and opted to implement a narrow band filter for the LED's specific wavelengths. The drawback to using IR is that it requires modifications to the camera, such as using a coloured glass optical-filter to block unwanted wavelengths.

In order to gain an initial insight and define a starting point for the machine vision navigation problem the author decided to use a system based in the visual wavelength spectrum to take advantage of readily available apparatus and components. The chosen LED (the 5*mm* Superbright *Red* Kingbright LED L-53SRC-DW) has a narrow viewing angle (30°) and gave the best light emission performance from the available resources. As outlined in chapter 3 the use of a red LED in the visual spectrum will minimise the susceptibility to atmospheric effects. The circuit diagram used can be found in appendix 4. Finally, in order to keep the system as simple as possible for the initial concept proving trials it was decided not to pulsate the light source.

4.2 Marker reference frame:

Suitable reference frames are required in order to determine the follower aircraft's pose relative to the target. Figures 15 and 16 below illustrate their use.

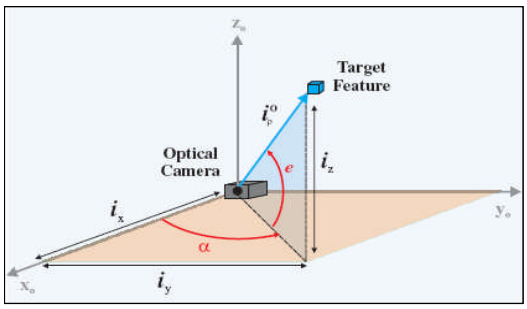

Figure 15[m]: Target position location

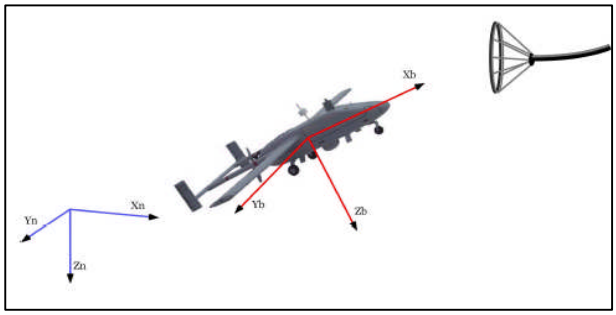

Figure 16[n]: Reference axes for re-fuelling.

Referring to figure 15 the position vector, i_ρ^o of the camera relative to a sample target is shown. This is a useful illustration and is applicable to the current pose estimation problem for the UAV follower-leader situation. Replacing the target feature by an LED and adding three more LED targets onto the leader creates the solution used in the project. Formulating the problem for just one marker as in figure 15 above:

- i_ρ^o = line of sight unit vector (from the optical camera to the target)

  which is given by $\left[i_x,\ i_y,\ i_z\right]^T$ …(eqn 4.2.1)
- $\psi = \tan^{-1}\left(\frac{i_y}{i_x}\right) + \upsilon_\psi$ …(eqn 4.2.2) azimuth angle measured from camera focal plane.
- $\theta = \tan^{-1}\left(i_z\right) + \upsilon_\theta$ …(eqn 4.2.3) elevation angle measured from the camera focal plane.
- $\upsilon_o^o = \left[\upsilon_\psi, \upsilon_\theta\right]^T$ … (eqn 4.2.4) optical camera noise vector.

For simplification the camera is assumed to be inline with the UAV *X-axis*.

[m] Figure 3.a), (Woffinden and Geller, 2007)
[n] Figure 5, (Tandale et al., 2005)

The re-fuelling problem can be described using three axes systems (see figure 16 above):

- 1) $[X_n, Y_n, Z_n]^T$ … (eqn 4.2.5) Earth axes.
- 2) $[X_b, Y_b, Z_b]^T$ … (eqn 4.2.6)UAV body axes (located at UAV *centre of gravity*)
- 3) $[X_d, Y_d, Z_d]^T$ …(eqn 4.2.7)the displacement between the drogue and the UAV's refuelling probe

Using the above axes the distance between the probe and drogue can be compared enabling pose algorithms to be developed.

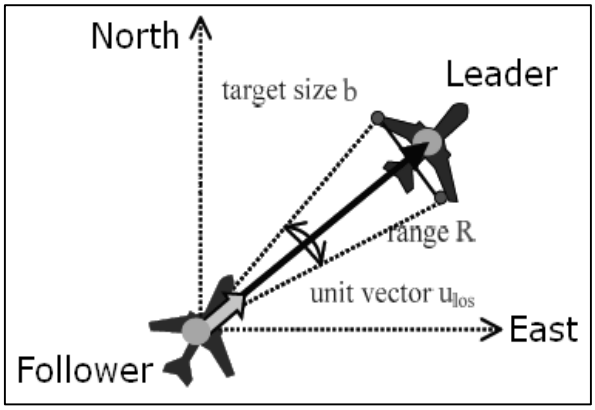

Figure 17[o]: Leader follower formation

A final example of using aircraft geometry for range estimation is discussed in (Sattigeri et al., 2005) see figure 17. Range, *R* is given by:

- $R = \sqrt{(X_L - X_F)^2 + (Y_L - Y_F)^2 + (Z_L - Z_F)^2}$ … (eqn 4.2.8)

where subscript *L* and *F* represent *leader* and *follower*.

The solution selected by the author was to create a cross-shaped pattern using four LED's, attaching one LED to each wing tip and to the top and bottom of the fin. Each LED was attached to a known reference point within the model's NED axis system. This created an outline of the model necessary for determining the follower's pose. In addition, distances between the models' *centre of gravity* and each LED reference point along with the test position for the *Eyecam*© were measured beforehand. Therefore, once the camera calibration has been performed, the relationship of the separation distance between the wing tip LED's in pixels can be used as a means of estimating the range (*R*) between the target and follower.

[o] Figure 2, (Sattigeri et al., 2005)

4.3 Formatting onto Leader/Target:

The machine vision problem has initially been approached from the standpoint where both the follower and the target are already sufficiently close together so that individual markers can be identified. This scenario is only made possible because of the prior step which requires the follower to manoeuvre from its current location to a position aft of the target. The use of "angles only" navigation has been proposed by (Woffinden and Geller, 2007), whom point out that this technique has been used much earlier in Naval applications when navigation was performed using a sextant. The principle behind the method lies in measuring the Line of Sight (LOS) angles (i.e. *azimuth* and *elevation*) from the reference point (taken to be the camera) to the target position and is based on an autonomous orbital rendezvous.

The rendezvous (RDV) is divided into four distinct phases including the final docking:

1) ***RDV operation***
2) ***Close proximity***
3) ***Final approach***
4) ***Pre-docking phases***

N.B: D – diameter, ρ – relative range and θ_{pixel} – angular size

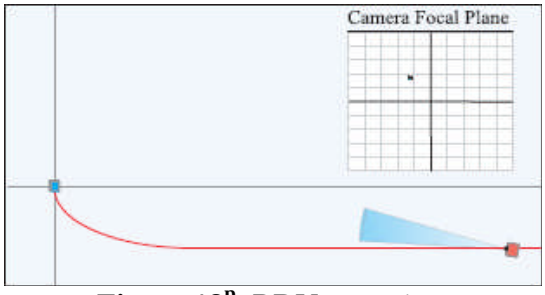

Figure 18[p]: RDV operation

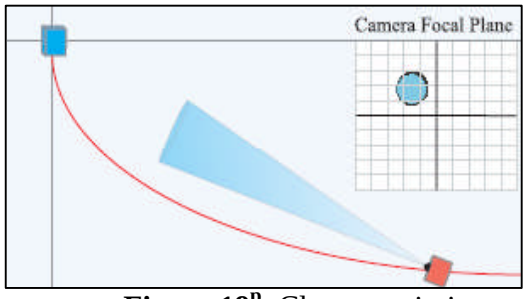

Figure 19[p]: Close proximity

1) *RDV operation* (10- 1km): When the target is observable on the focal plane but the apparent target angular diameter on the image is less than one pixel, θ_{pixel} (figure 18) $\frac{D}{\rho} < \theta_{pixel}$ ... (eqn 4.3.1), the optical camera can track the centroid of the target relatively well in order to generate the azimuth and elevation angles.

[p] Figure 2, (Woffinden and Geller, 2007)

2) *Close proximity phase* (1km to 100m): The camera is close enough to distinguish the target angular size but the distance is still great enough for the target image to stay within the camera's field of view, θ_{FOV} (figure 19 above) therefore:

$$\theta_{pixel} < \frac{D}{\rho} < \theta_{FOV} \ldots \text{(eqn 4.3.2)}$$

3) *Final approach phase* (100m – 5m): When the target occupies the entire camera field of view, $\frac{D}{\rho} > \theta_{FOV}$ … (eqn 4.3.3) (figure 20 below), the camera is no longer capable of determining the *azimuth* and *elevation* angles in relation to the target's centroid. However, the camera can identify three or more key features which can be used to measure their relative azimuth and elevation to the drogue/leader. This situation now corresponds to that of the follower-leader navigation problem using individual markers on the target as proposed in the current project.

4) *Pre-docking phase* (5m – 5cm): Since the chaser approaches the target before initiating pre-docking (such as with the fuel drogue in an air-to-air refuelling problem), the chaser has been aligned as a result of the manoeuvres leading up to this point. Finally, using the features of the docking port and key targets surrounding it the camera can measure the azimuth and elevation angles to perform the final procedure (figure 21 below).

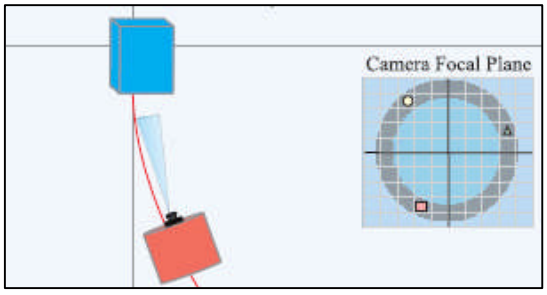

Figure 20[p]: Final approach

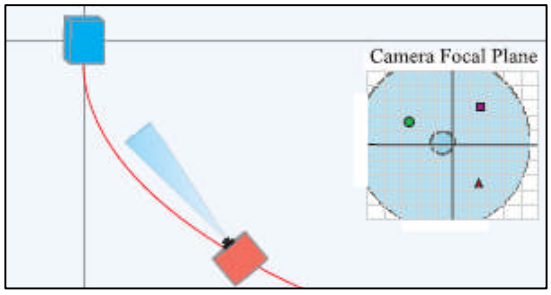

Figure 21[p]: Pre-docking

The limiting factor for the starting distance is a function of the camera's ability to resolve the target to the order of 1 miliradian.

5) Pose estimation:

Leading on from the target identification process, the estimation of the states of the UAV's ownship (the position in 3-*D*, as well as the orientation in yaw (ψ), pitch (θ), and roll (φ)) can be determined. These states are required as they are the inputs into the flight control/autopilot which will guide the UAV from its current location to the target/leader. The navigation problem can be formulated with the axes systems described in chapter 4 then resolved using vectors and trigonometry.

5.1) Determining the UAV states:

To solve the navigation problem it is necessary to create a position vector, which describes the location of the target relative to the follower. The following equations refer to the model presented by (Oh and Johnson, 2007) and are formulated from the follower to the target/leader in the Navigation Reference frame as illustrated in figure 22 below.

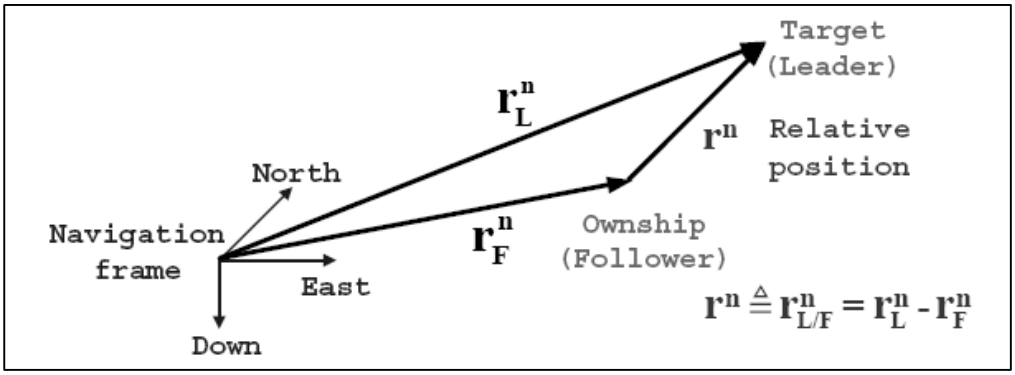

Figure 22[q]: illustrates the follower–leader *relative position*, r^n in the navigation frame.

The *relative position* 3-*D* vector, $r^n = \begin{bmatrix} X & Y & Z \end{bmatrix}^T$ … (eqn 5.1.1)

this corresponds to the first three displacement states $\begin{bmatrix} x_1 & x_2 & x_3 \end{bmatrix}^T$. Differentiating these w.r.t *x*, will yield the *relative velocity* vector, $\dot{r}^n = v^n = \begin{bmatrix} U & V & W \end{bmatrix}^T$ … (eqn 5.1.2)

which corresponds to the three velocity states $\begin{bmatrix} x_4 & x_5 & x_6 \end{bmatrix}^T$. Differentiating again w.r.t *x*, leads to the *relative acceleration* vector, $\ddot{r}^n = \dot{v}^n = a^n = \begin{bmatrix} \dot{U} & \dot{V} & \dot{W} \end{bmatrix}^T$ … (eqn 5.1.3)

[q] Figure 3, (Oh and Johnson, 2007)

and yields the three velocity rate states $\begin{bmatrix} \dot{x}_4 & \dot{x}_5 & \dot{x}_6 \end{bmatrix}^T$.

Three additional states are included: firstly, $x_7 = b$, the target/leader size, secondly, $x_8 = a_{lat}$ the target/leader lateral acceleration and finally, $x_9 = a_{long}$, the target/leader longitudinal acceleration.

Therefore, the state variables can be represented in matrix form:

$$x = \begin{bmatrix} x_{1:3} & x_{4:6} & x_7 & x_8 & x_9 \end{bmatrix}^T = \begin{bmatrix} r^n & a^n & b & a_{lat} & a_{long} \end{bmatrix}^T \quad \text{… (eqn 5.1.4)}$$

It should be noted that the following assumptions need to be made to create the model:

- the leader's longitudinal acceleration is perpendicular to the leaders total velocity and to lies in the vertical plane that is generated between the total velocity vector and vertical direction vector (W_L).
- the leader's lateral acceleration is perpendicular to the leaders total velocity.

Thus, this enables the leader's acceleration can now be expressed as a function of the leader's velocity component:

$$a_L^n = \frac{1}{\sqrt{U_L^2 + V_L^2}} \begin{bmatrix} \dfrac{U_L W_L}{\sqrt{U_L^2 + V_L^2 + W_L^2}} & -V_L \\ \dfrac{V_L W_L}{\sqrt{U_L^2 + V_L^2 + W_L^2}} & U_L \\ -\dfrac{U_L^2 + V_L^2}{\sqrt{U_L^2 + V_L^2 + W_L^2}} & 0 \end{bmatrix} \begin{bmatrix} a_{long} \\ a_{lat} \end{bmatrix} \quad \text{… (eqn 5.1.5)}$$

where $v_L^n = \begin{bmatrix} U_L & V_L & W_L \end{bmatrix}^T = v^n + v_F^n = \begin{bmatrix} x_4 & x_5 & x_6 \end{bmatrix}^T + v_F^n$ … (eqn 5.1.6)

with the above terms defined as:

a_L^n = leader acceleration in navigation frame

a_F^n = follower acceleration in navigation frame (follower's navigation system)

v_L^n = leader velocity vector in navigation frame

v_F^n = follower velocity vector in navigation frame (follower's navigation system)

Following on from equations 5.1.5 and 5.1.6 the relative acceleration between the follower and leader can be determined using the state variables:

$$a^n = a_L^n - a_F^n = \frac{1}{\sqrt{U_L^2 + V_L^2}} \begin{bmatrix} \frac{U_L W_L}{\sqrt{U_L^2 + V_L^2 + W_L^2}} & -V_L \\ \frac{V_L W_L}{\sqrt{U_L^2 + V_L^2 + W_L^2}} & U_L \\ -\frac{U_L^2 + V_L^2}{\sqrt{U_L^2 + V_L^2 + W_L^2}} & 0 \end{bmatrix} \begin{bmatrix} a_{long} \\ a_{lat} \end{bmatrix} - a_F^n \qquad \text{… (eqn 5.1.7)}$$

Now that the followers states have been defined, the targets position with measurement noise can be determined and expressed as a continuous time state-space model:

$$\dot{x}(t) = f(x(t)) + w(t) \qquad \text{… (eqn 5.1.8)}$$

(where $w(t)$ represents the noise vector)

which can be expressed using the known states is: $v_L^n = \begin{bmatrix} \dot{r}^n & \dot{v}^n & \dot{b} & \dot{a}_{lat} & \dot{a}_{long} \end{bmatrix}^T$

$$= \begin{bmatrix} v^n & a^n & 0 & 0 & 0 \end{bmatrix}^T + \begin{bmatrix} n_v & n_a & n_b & n_{a\,lat} & n_{a\,long} \end{bmatrix}^T \qquad \text{… (eqn 5.1.9)}$$

(where *n* represents the noise for each of the state variables)

Thus by substituting eqns 5.1.6 and 5.1.7 into eqn 5.1.9 the state space model becomes:

$$\begin{bmatrix} \dot{x}_1 \\ \dot{x}_2 \\ \dot{x}_3 \\ \dot{x}_4 \\ \dot{x}_5 \\ \dot{x}_6 \\ \dot{x}_7 \\ \dot{x}_8 \\ \dot{x}_9 \end{bmatrix} = \begin{bmatrix} x_4 \\ x_5 \\ x_6 \\ \frac{1}{\sqrt{U_L^2 + V_L^2}} \begin{bmatrix} \frac{U_L W_L}{\sqrt{U_L^2 + V_L^2 + W_L^2}} & -V_L \\ \frac{V_L W_L}{\sqrt{U_L^2 + V_L^2 + W_L^2}} & U_L \\ -\frac{U_L^2 + W_L^2}{\sqrt{U_L^2 + V_L^2 + W_L^2}} & 0 \end{bmatrix} \begin{bmatrix} x_9 \\ x_8 \end{bmatrix} - a_F^n \\ 0 \\ 0 \\ 0 \end{bmatrix} + \begin{bmatrix} n_v \\ n_a \\ n_b \\ n_{alat} \\ n_{along} \end{bmatrix} \qquad \text{… (eqn 5.1.10)}$$

N.B. the follower's velocity, v_F^n and acceleration, a_F^n are assumed to be readily available from the followers navigation system (either an Inertial Navigation System or GPS). Having now provided a model describing the displacement between the follower and leader/target a pose angle model can be defined. Figure 23 below shows the reference frame and pose angles used to define the follower's position relative to the leader/target.

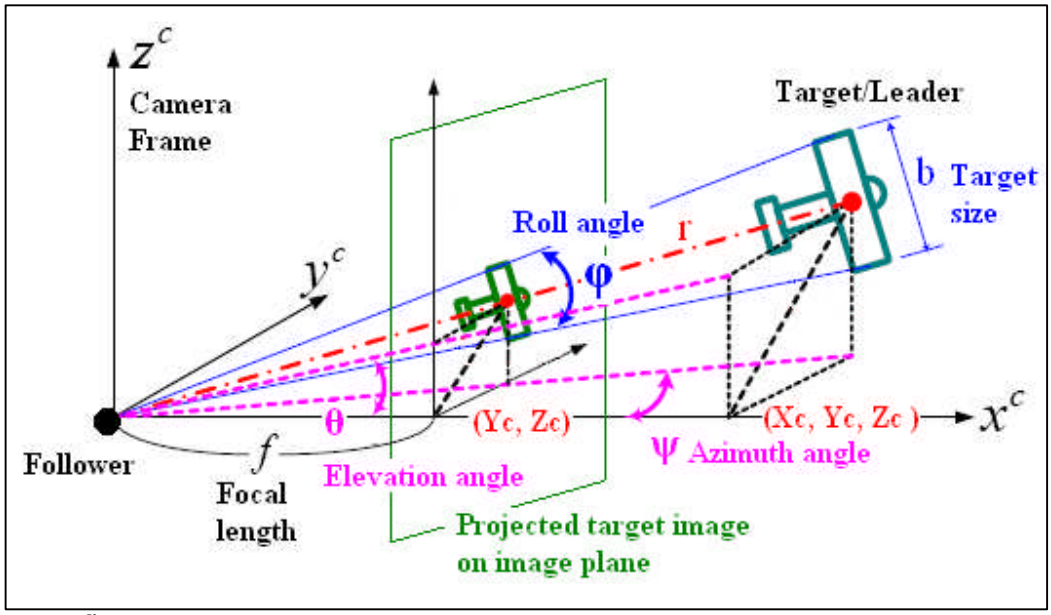

Figure 23[r]: illustrates the target image on the camera image plane for pinhole camera

As already mentioned the three pose angles are: ψ, Azimuth, θ, Elevation and φ, Roll and, referring to figure 23 above these angles can be determined from the reference frame measurements as follows:

$$\tan(\psi) = \frac{Y_c}{X_c} \quad \therefore \psi = \tan^{-1}\left(\frac{Y_c}{X_c}\right) \ (rads) \qquad \ldots \text{(eqn 5.1.11)}$$

$$\tan(\theta) = \frac{Z_c}{X_c} \therefore \theta = \tan^{-1}\left(\frac{Z_c}{X_c}\right) \ (rads) \qquad \ldots \text{(eqn 5.1.12)}$$

$$\tan(\varphi/2) = \frac{b}{2r} = \frac{b}{2\sqrt{X_c^2 + Y_c^2 + Z_c^2}} \therefore \varphi = 2\tan^{-1}\left(\frac{b}{2\sqrt{X_c^2 + Y_c^2 + Z_c^2}}\right)(rads) \ \ldots \text{(eqn 5.1.13)}$$

where subscript *c*, denotes the camera reference frame used in the pinhole camera model and *r*, is the relative distance between the follower and the leader/target $\left(\sqrt{X_c^2 + Y_c^2 + Z_c^2}\right)$.

[r] Figure 4, (Oh and Johnson, 2007)

The above relationships are then modified for application in the follower to leader pose estimation. The information obtained by the camera, relating to the position of the leader aircrafts wing tips can now be utilised: left wing tip (y_l, z_l) and right wing tip (y_r, z_r) as well as its centre point (y_c, z_c). The distance *X* is replaced by the cameras focal length, *f*, and hence the relative distance in the projected image frame, *r* becomes: $\left(\sqrt{f^2 + y_c^2 + z_c^2}\right)$. Therefore, the projected target size is defined by: $\left(\sqrt{(y_l - y_r)^2 + (z_l - z_r)^2}\right)$, substituting into the roll angle equation (eqn 5.1.13):

$$\tan(\varphi/2) = \frac{\sqrt{(y_l - y_r)^2 + (z_l - z_r)^2}}{2\sqrt{f^2 + y_c^2 + z_c^2}} = \frac{b}{2r} = \frac{b}{2\sqrt{X_c^2 + Y_c^2 + Z_c^2}} (rads) \ldots \text{(eqn 5.1.14)}$$

bringing together all the pose measurements into matrix form yields:

$$y = \begin{bmatrix} \psi \\ \theta \\ \varphi \end{bmatrix} = \begin{bmatrix} \tan^{-1}\left(\frac{y_c}{f}\right) & \tan^{-1}\left(\frac{x_c}{f}\right) & 2\tan^{-1}\left(\frac{\sqrt{\left(\frac{y_l}{f} - \frac{y_r}{f}\right)^2 + \left(\frac{z_l}{f} - \frac{z_r}{f}\right)^2}}{2\sqrt{1 + \left(\frac{y_c}{f}\right)^2 + \left(\frac{z_c}{f}\right)^2}}\right) \end{bmatrix}^T (rads)$$

… (eqn 5.1.15)

5.2) Verification of ownship:

As outlined in section 5.1, above, a means of quantifying the velocity and acceleration of the follower is essential. This will enable a comparison of the followers' current position with that determined by the pose algorithm. Therefore, a technique combining the two pose results will add a degree of robustness to the unmanned navigation solution. Possible navigation systems capable of providing the required information are: an Inertial Navigation System/Inertial Measuring Unit (INS/IMU), a Global Positioning System, angular rate gyros and accelerometers. Some of these systems have already been successfully used for navigation in unmanned open atmospheric flight (Ma et al., 2006).

The ability to determine the follower's state will be of significant benefit in either the manoeuvring formation flight or the in-flight refuelling scenarios. In these specific cases the vision navigation system will have difficulty in distinguishing which of the two (follower or leader/target) has moved. However, by using an INS device attached to the follower, its states can be determined and fed into the pose estimation algorithm, thus enabling a correct interpretation of the visual information captured by the camera to be made.

5.3) Noise filtering:

Inaccuracies relating to the measurements of the follower's velocity and acceleration from the additional navigation system (such as INS or GPS) will create unwanted noise. Having formulated the pose problem in section 5.1 the follower's states can be processed by applying an Extended Kalman Filter (EKF). The EKF consists of two steps, the *Prediction* step which is then followed by the *Update* step. This filter is an extension to the standard Kalman Filter (KF) and can be applied to non-linear problems by linearising the system about a predicted estimate for each time step. The following EKF equations were presented in the model used by (Watanabe et al., 2007), and are reproduce overleaf.

Starting with the state space model: $\dot{x}(t) = F(x(t)) + Ga_v(t)$ … (eqn 5.3.1)

(where $a_v(t)$ represents the acceleration vector in inertial frame)

the linear discretised system is: $x_{k+1} = \Phi_k x_k + G_k a_{vk}(t)$ … (eqn 5.3.2)

with $\Phi_k = e^{F(t_{k+1}-t_k)} = \begin{bmatrix} I & (t_{k+1}-t_k)I \\ 0 & I \end{bmatrix}$ and $G_k = \int_{t_k}^{t_{k+1}} e^{F(t_{k+1}-t_k)} G dt = \begin{bmatrix} \frac{1}{2}(t_{k+1}-t_k)^2 & I \\ (t_{k+1}-t_k) & I \end{bmatrix}$

at this point the two steps (*Prediction* and *Update*) of the EKF can be established in order to estimate the followers relative states at time step t_k, x_k from the vision based measurements determined by equation 5.1.8.

Prediction:

$$\hat{x}_{k+1}^- = \Phi_k \hat{x}_k + G_k a_{vk} \quad \text{… (eqn 5.3.3)}$$

$$P_{k+1}^- = \Phi_k P_k \Phi_k^T \quad \text{… (eqn 5.3.4)}$$

Update:

$$\hat{x}_{k+1} = \hat{x}_{k+1}^- + K_{k+1}\Phi_k \hat{x}_k \left(z_{k+1} - h\left(\hat{X}_{ck+1}^-\right)\right) \quad \text{… (eqn 5.3.5)}$$

$$P_{k+1} = \left(I - K_{k+1}H_{K+1}\right)P_{k+1}^- \quad \text{… (eqn 5.3.6)}$$

$$K_{k+1} = P_{k+1}^- H_{K+1}^T \left(H_{K+1} P_{k+1}^- H_{K+1}^T + R_{k+1}\right)^{-1} \quad \text{… (eqn 5.3.7)}$$

where:

$\hat{x}_k^-$ and $\hat{x}_k$ represent the predicted and updated estimates of the relative state x, at time step t_k.

P_k^- and P_k are the error covariance matrices for the predicted and updated estimates.

K_{k+1} is the Kalman gain matrix

H_{k+1} is the measurement matrix and is defined by:

$$H_{k+1} = \left.\frac{\partial h\left(X_c\left(t_{k+1}\right)\right)}{\partial x\left(t_{k+1}\right)}\right|_{x(t_{k+1})=\hat{x}_{k+1}^-} = \left[\frac{1}{\hat{X}_{ck+1}^-}\left[-h\left(\hat{X}_{ck+1}\right)\ \ I\right]L_c\left(t_{k+1}\right)\ \ O\right] \quad \text{… (eqn 5.3.8)}$$

where $\hat{X}_{ck+1}^- = L_c\left(t_{k+1}\right)\hat{X}_{ck+1}$

and $R_{k+1} = \frac{\sigma^2}{\hat{X}_{ck+1}^{-2}} I$

because of the camera's limited field of view the image processor may not always be able to capture the target, thus the corresponding vision-based measurements will not always be available. When this occurs, only the EKF prediction is performed (equations 5.3.3 and 5.3.4).

Without the vision-based measurement, a measurement of infinitely large noise arises, $R_{k+1} = \infty$ and the Kalman gain becomes zero.

Thus: $R_{k+1} = \infty$ which results in: $\hat{x}_{k+1} = \hat{x}_{k+1}^{-}$ and $P_{k+1} = P_{k+1}^{-}$

Following the application of the estimated relative position and velocity, an estimation of the target's state can be calculated by adding the known vehicle's state.

$\hat{X}_t(t_k) = \hat{X}_k + X_v(t_k)$, and $\hat{V}_t(t_k) = \hat{V}_k + V_t(t_k)$ … (eqn 5.3.9)

These estimates can then be fed into the guidance system.

5.4) Pose estimation algorithms:

The following section summarises the principles behind four different pose algorithms found during background research of the machine vision autonomous navigation topic.

1) A Gaussian Least-Squares Differential-Correction (GLSDC) algorithm developed by (Valasek et al., 2005), is proposed for use in the air-to-air refuelling scenario. The algorithm determines the states, attitude and position of the re-fuelling drogue once iterations of the least-square method have converged. The pose estimation technique uses data from a 6 degree of freedom position and attitude sensor. A rapid sensor update rate of 100*Hz* has been chosen in order to adequately track the re-fuelling drogue's movement. This solution is then fed into the Proportional Integral Filter optimal Nonzero Setpoint with Control Rate Weighting (PIF-NZSP-CRW) which is the autonomous navigation system used to generate the navigation solution for the UAV to dock with the re-fuelling drogue.

2) An angles-only-rendezvous navigation filter is presented in (Woffinden and Geller, 2007). This is an EKF which generates attitude data by processing angular measurements of three features located on the target using a navigation camera. A 35 state vector, including 13 target states, 13 follower states and 9 parameters is used to produce an orbital rendezvous simulation model and thus the relative position and velocity between the two vehicles can be estimated. This method has been developed specifically for the rendezvous and docking scenario of two spacecraft in orbit.

3) The Lu, Hager and Mjolsness (LHM) pose estimation algorithm is presented in (Pollini et al., 2005). This algorithm was chosen by the authors for its execution speed and capability to perform in "real-time" with disturbances present to the marker tracking problem. In addition, the pose algorithm is based on collinearity in object space. Using the known 3D locations of markers on the target, a transformation matrix between the 3D marker locations and the 2D camera plane is computed which then enables the estimation of the translation vector by minimising an error cost function, via an iterative process.

4) The **Mfitvid** program developed by (Hobbs, 2003), estimates both position and pose from the image data (pixel *row* and *column*) of markers placed on a target object. The camera's intrinsic properties are also required and need to be determined in a calibration performed beforehand. In order to generate the tangents of the markers inclination and azimuth, the program requires the 3-D position of each of the target's markers relative to the camera in each captured image. The Leuvenburg-Marquardt algorithm is used by the program to fit a non-linear model to the captured image data using a reference axis system relative to the target object.

5.5) Proposed solution:

The first steps towards achieving a MV based autonomous navigation system have been made using the **Mfitvid** program developed at Cranfield University by (Hobbs, 2003). Initially, a pose estimation technique for the MV follower to leader/target problem was developed and the experimental work that has been carried out towards accomplishing this task can be found in chapter 6. Secondly, the requirements for the image processing and pose estimation system have been discussed in chapter 4. Finally, using the system proposed by (Sattigeri et al., 2005), as a guideline, a complete overview of the machine vision and autonomous navigation solution can be shown (figure 24 below).

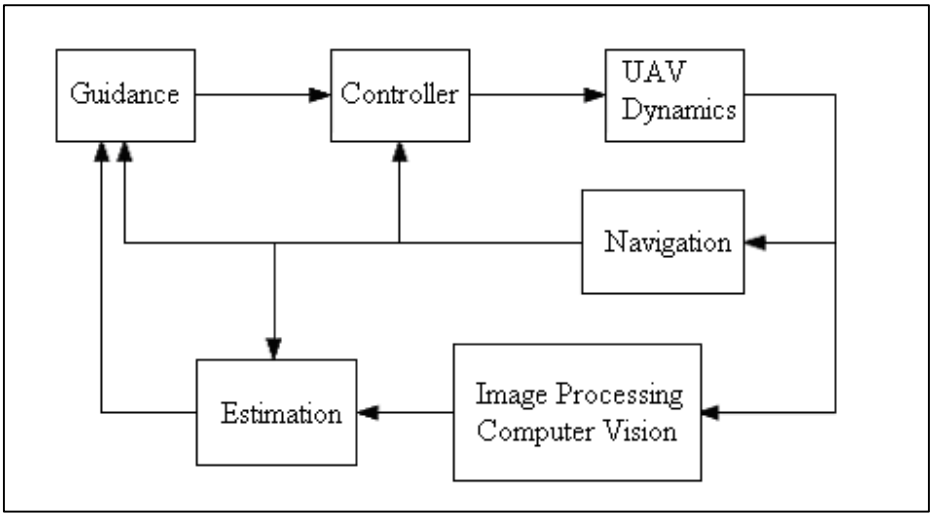

Figure 24[s]: illustrates a machine vision guidance control scheme for a follower UAV.

The *UAV Dynamics* are in part captured by the *Image Processing Computer Vision* block (this contains the current work that has been presented in this thesis) which outputs the estimated pose and size of the target/leader relative to the follower UAV. Thus, the *Estimation* block which consists of an Extended Kalman Filter, estimates the range and range-rate, which are required by the *Guidance* block to compute the velocity and acceleration commands necessary for the *Controller* block. A *Navigation* block, which represents the Inertial Navigation System, provides a comparison between the *pose* and *position* information determined by the *Image Processing Computer Vision* and *Estimation* blocks. Finally, the resulting commands executed by the *Controller* block modify the *UAV Dynamics*, hence completing the system and re-starting the closed-loop.

[s] Figure 1, (Sattigeri et al., 2005)

6) Testing:

The following chapter includes the *introduction*, *experimental results*, *discussion* and *conclusion* which have been taken from the reports of the 3 following practical experiments performed by the author:

- **Experiment 1**: *Camera Calibration*
- **Experiment 2**: *RGB estimation*
- **Experiment 3**: *Aircraft-LED position estimation*

Each of these experiments has been written as a stand alone report and can be found at the end of the appendix section. The reports are included in order to provide a documented procedure for persons coming from a flight dynamics background, who would be unfamiliar with machine vision techniques. Should further similar experimental work be required or need to be reproduced, the procedures to repeat the same experiments are explained. In addition, the reports and work performed contribute towards furthering the machine vision techniques within the department, the complete reports are included at the end of the Appendix section.

Furthermore, all the experimental data, including the images and results that were produced as a result of the experimental work has been saved onto an *Appendix CD* (see appendix 7 for the detailed contents list). This CD has been left with Dr A.K. Cooke and requests to borrow it should be addressed to: a.cooke@cranfield.ac.uk

6.1) Experiment 1-Camera Calibration: 05/07/08 – 08/07/08

6.1.1) Introduction experiment 1:

The purpose of this experiment was to provide an estimation of the amount of distortion present for two *Eyecam* CMOS micro-cameras (ALM-2451G/4RX) to a 1st order degree. Using readily available apparatus a simple experiment was devised and initial results for the lens' central distortion was determined.

6.1.2) Results experiment 1:

Using the squares closest to the centre of the image (see figure 25 below) the following calculations were performed for both cameras. Note that the square lengths in pixels were measured for the closest complete square nearest the centre of the lens. For example referring to figure 25, taking the centre of the lens to be represented by the black dot, the nearest complete squares are between the two white dots in both the X and Y directions.

Yellow dot camera:

Using the images named: **Pierre_machine_vision_test_5_july_0003** and **Pierre_machine_vision_test_5_july_0002**. Image 0002 and 0003 were taken at 1.15*m* and 0.15*m* away from the camera central lens respectively for the **Yellow dot camera** (this denotes the principal camera used throughout the research It has an a RF of 2472MHz).

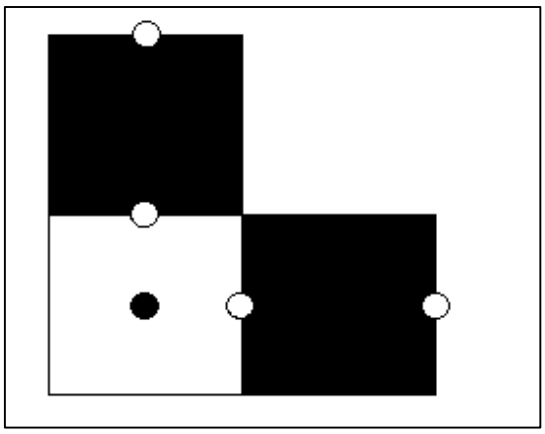

Image 0002

In *X*: $\frac{0.026}{10} \Big/ 1.15 = \underline{2.2609}$ *m*rad

In *Y*: $\frac{0.026}{12} \Big/ 1.15 = \underline{1.8841}$ *m*rad

Image 0003

In *X*: $\frac{0.026}{78} \Big/ 0.15 = \underline{2.3423}$ *m*rad

In *Y*: $\frac{0.026}{74} \Big/ 0.15 = \underline{2.2222}$ *m*rad

Figure 25: A sample grid near image centre.

Green dot camera:

Using the images named: **green_dot_camera_calib_close_up** and **green_dot_camera_calib_far_away**. The **Green dot camera** is the spare/secondary camera and has an RF of 2472MHz. The same procedure for calculating a first order model was used and the following values were established:

Far_away:

In X: $\frac{0.026}{24} \Big/ 0.57 = \underline{1.9006}$ *m*rad

In Y: $\frac{0.026}{25} \Big/ 0.57 = \underline{1.8246}$ *m*rad

Close_up:

In X: $\frac{0.026}{76} \Big/ 0.16 = \underline{2.1382}$ *m*rad

In Y: $\frac{0.026}{84} \Big/ 0.16 = \underline{1.9345}$ *m*rad

Summarising the close up calibration results:

Where the test image fills the majority of the field of view, the first order camera calibration is determined to be:

Camera:	**X**	**Y**
Yellow dot (principle)	2.3423 *m*rad	2.2222 *m*rad
Green dot (secondary)	2.1382 *m*rad	1.9345 *m*rad

Table 3: Camera calibration results

Uncertainty in measurements (For **Yellow dot** camera):

The measured quantities have the following ranges of precision: Tape measure = $\pm 0.002m$, Ruler = $\pm 0.0005m$, Pixel in $X = \pm 2$ pixel and $Y = \pm 2$ pixel

For the 15*cm* trial the following (1) Max error and (2) Min error are calculated with:

(1) Measurements: $L = 0.152m$, $X_{sq} = Y_{sq} = 0.0265m$, $X_{pix} = 76$ pixels and $Y_{pix} = 80$ pixels

(2) Measurements: $L = 0.148m$, $X_{sq} = Y_{sq} = 0.0255m$, $X_{pix} = 72$ pixels and $Y_{pix} = 76$ pixels

Therefore 1) Max error is determined to be:

In X: $\frac{0.0265}{76} \Big/ 0.152 = \underline{2.2940}$ *m*rad

In Y: $\frac{0.0265}{80} \Big/ 0.152 = \underline{2.1793}$ *m*rad

And the 2) Min error is determined to be:

In X: $\frac{0.0255}{72} \Big/ 0.148 = \underline{2.3930}$ *m*rad

In Y: $\frac{0.0255}{76} \Big/ 0.148 = \underline{2.2671}$ *m*rad

These enable a percentage error to be calculated in the X and Y axis:

Value	X	Y
Min	2.062 %	2.165 %
Max	1.9305 %	2.021 %

Table 4: Percentage error values for X and Y.

Following these results the camera calibration file, **imagecal_spycam** was created with the calibration data (for the **Yellow dot** camera) as required for the pose position software used in *Experiment 3*:

```
# imagecal_spycam.txt
# Contains image calibration coefficients for the Spycam.
# File contains one data line summarising the contents (# of cameras, # of coefficients, etc.)
# then a line giving the image origin for each camera (origin_col, origin_row),
# and then the lines giving coefficients of the polynomials used to model distortions for
# each camera (inclination coefficients, then azimuth; excluding a[0] which is assumed to be 0).
# All comment lines are at the head of the file and start with '#', data lines start with a white
# space character.
#
# S.E. Hobbs, 11:06, 17 Jul 2008   Modified PDJ, 16:00, 05 Aug 2008
        2       10
                383.5           287.5           383.5           287.5
                0.0             2.2E-3          -0.0            2.2E-3
                2.3E-3          0.0             2.3E-3          0.0
                0.0             0.0             0.0             0.0
                0.0             0.0             0.0             0.0
                0.0             0.0             0.0             0.0
                0.0             0.0             0.0             0.0
                0.0             0.0             0.0             0.0
                0.0             0.0             0.0             0.0
                0.0             0.0             0.0             0.0
```

Insert 1: Camera calibration results, as required for Experiment 3.

This file enables the first order distortion for the **Yellow dot** camera to be accounted for, in the correct format required for Experiment 3 (when the pose estimation program **Mfitvid** is run).

6.1.3) Discussion experiment 1:

The above experimental procedure describes the process to determine a basic first order relationship for the cameras' distortion. An important point to note during the image capturing process is the choice of backing material for the calibration grid pattern. A flat rigid backing material is required, such as sheet steel which is used in this experiment. This is essential in order to ensure that the calibration grid remains flat and perpendicular to the test camera.

The first order camera calibration has been determined to be approximately 2*mrad* (table 3). These results have been written in the required form for the **Mfitvid** program (see insert 1). The estimated errors in X and Y for the camera calibration were determined to be approximately 2% (table 4). However, due to the shape of the cameras lens these values would be expected to be higher in accordance with the "fish-eye" / skew effect associated with such a spherically shaped lens. The calibration would thus be expected to hold true for the central region in each image. Therefore, care must be taken when capturing further images in order to keep the object of interest within the centre of the cameras' field of view.

A final note regarding the experiment set-up should be mentioned. Before launching the *Capwizz*© software all cables should be correctly connected and the power to each device turned on, these should not be removed or turned off during the image capturing. Failure to adhere to these precautions may cause problems when attempting to preview and capture any image with the software, thus requiring a re-launch of the *Capwizz*© program.

6.1.4) Conclusion experiment 1:

This simple experiment has enabled a first order calibration of the two *Eyecams* to be performed. The values for the **Yellow dot** camera have been written in the necessary file format (**Imagecal_spycam**) for the **AVI1** converter. Thus the **Mfitvid** program can now also be used to determine the position/pose of the camera relative to key points within an image as required for Experiment 3.

6.2) Experiment 2-RGB estimation 07/07/08 – 11/07/08

6.2.1) Introduction experiment 2:

The aim of this experiment was to determine the ability of the two different *Eyecams* (**Yellow dot** and **Green dot**) to detect and isolate the three main colours in a given image. In order to enable a better comparison of the results, an Olympus Digital Camera was also used to capture images. Two LED's similar to those that would be used in the main pose estimation experiment provided the target image with a "passive" (i.e. without an information signal transfer, such as radio waves) colour source to be analysed.

Machine Vision Image RGB results from post processing of 5th of July experiments Yellow dot Camera (N0.1)

		Red			Green			Blue			Average Σ RGB		
Name of Image	LED	Mean	σ	Median	Mean	σ	Median	Mean	σ	Median	Mean	σ	Median
Pierre_machine_vision_test2_5_July_0000	Top	231.4	1.1	232.0	225.1	0.9	225.0	220.3	1.7	221.0	225.6	1.2	226.0
Taken @ 15cm from camera	Bottom	237.8	2.2	238.0	230.7	1.3	231.0	227.5	1.4	227.0	232.0	1.6	232.0
	Av.LED =>	***234.6***	***1.7***	***235.0***	***227.9***	***1.1***	***228.0***	***223.9***	***1.6***	***224.0***	***228.8***	***1.4***	***229.0***
Pierre_machine_vision_test2_5_July_0001	Top	222.8	1.9	222.0	216.5	3.0	217.0	211.5	1.9	212.0	216.9	2.3	217.0
Taken @ 53cm from camera	Bottom	232.7	2.1	233.0	223.5	3.4	224.0	221.3	2.2	221.0	225.8	2.6	226.0
	Av.LED =>	***227.8***	***2.0***	***227.5***	***220.0***	***3.2***	***220.5***	***216.4***	***2.1***	***216.5***	***218.2***	***3.7***	***221.5***
Pierre_machine_vision_test2_5_July_0002	Top	220.9	1.6	221.0	215.5	2.1	216.0	210.3	1.6	210.0	215.6	1.8	215.7
Taken @ 115cm from camera	Bottom	224.5	2.8	235.0	228.9	3.3	229.0	226.9	1.7	227.0	226.8	2.6	230.3
	Av.LED =>	***222.7***	***2.2***	***228.0***	***222.2***	***2.7***	***222.5***	***218.6***	***1.7***	***218.5***	***221.2***	***2.2***	***223.0***
Pierre_machine_vision_test2_5_July_0003	Top	235.2	2.8	235.0	228.9	3.3	229.0	226.9	1.7	227.0	230.3	2.6	230.3
Taken @ 115cm from camera (in Darkness)	Bottom	235.6	1.9	236.0	226.6	2.5	227.0	226.4	2.0	227.0	229.5	2.1	230.0
	Av.LED =>	***235.4***	***2.4***	***235.5***	***227.8***	***2.9***	***228.0***	***226.7***	***1.9***	***227.0***	***229.9***	***2.4***	***230.2***
Pierre_machine_vision_test2_5_July_0004	Top	217.8	2.0	217.0	212.9	2.7	213.0	207.4	1.6	207.4	212.7	2.1	212.5
Taken @ 230cm from camera	Bottom	220.4	2.6	220.0	213.5	2.6	213.0	208.6	2.5	208.0	214.2	2.6	213.7
	Av.LED =>	***219.1***	***2.3***	***218.5***	***213.2***	***2.7***	***213.0***	***208.0***	***2.1***	***207.7***	***213.4***	***2.3***	***213.1***
Pierre_machine_vision_test2_5_July_0005	Top	234.7	2.1	235.0	226.9	2.1	227.0	223.7	2.5	224.0	228.4	2.2	228.7
Taken @ 230cm from camera (in Darkness)	Bottom	231.9	6.3	234.0	221.2	6.6	224.0	221.6	6.2	223.0	224.9	6.4	227.0
	Av.LED =>	***233.3***	***4.2***	***234.5***	***224.05***	***4.35***	***225.5***	***222.7***	***4.35***	***223.5***	***226.7***	***4.3***	***227.8***

	Red			Green			Blue				Average Σ RGB		
Average of total Ave values for both LEDS	Mean	σ	Median	Mean	σ	Median	Mean	σ	Median		Mean	σ	Median
for the 6 positions =	228.8	2.5	229.8	222.5	2.8	222.9	219.4	2.3	219.5	Σ Ave. =	223.0	2.7	224.1

i.e average of average value from LEDs for the 6 different LED positions

σ = Standard deviation
Σ = Total

Table 5: Yellow dot camera RGB results.

Machine Vision Image RGB results from post processing of 8th of July experiments GREEN DOT CAMERA (No. 2)

		Red			Green			Blue			Average Σ RGB		
Name of Image	LED	Mean	σ	Median	Mean	σ	Median	Mean	σ	Median	Mean	σ	Median
Pierre_machine_vision_test2_8_july_0000	Top	208.7	27.8	220.0	206.9	29.8	220.0	205.8	28.6	218.0	207.1	28.7	219.3
Taken @ 15cm from camera	Bottom	207.0	10.9	213.0	201.0	18.2	211.0	201.7	15.8	210.0	203.2	15.0	211.3
	Av.LED =>	***207.9***	***19.4***	***216.5***	***204.0***	***24.0***	***215.5***	***203.8***	***22.2***	***214.0***	***205.2***	***21.9***	***215.3***
Pierre_machine_vision_test2_8_july_0001	Top	207.4	4.7	208.0	207.1	5.0	208.0	205.1	4.9	206.0	206.5	4.9	207.3
Taken @ 30cm from camera	Bottom	204.9	25.2	215.0	201.3	30.9	214.0	199.7	29.5	212.0	202.0	28.5	213.7
	Av.LED =>	***206.2***	***15.0***	***211.5***	***204.2***	***18.0***	***211.0***	***202.4***	***17.2***	***209.0***	***220.8***	***31.0***	***210.5***
Pierre_machine_vision_test2_8_July_0002	Top	189.9	33.8	206.0	189.7	34.1	206.0	187.6	34.5	204.0	189.1	34.1	205.3
Taken @ 50cm from camera	Bottom	202.4	26.1	214.0	194.9	30.0	210.0	195.4	28.5	210.0	197.6	28.2	211.3
	Av.LED =>	***196.2***	***30.0***	***210.0***	***192.3***	***32.1***	***208.0***	***191.5***	***31.5***	***207.0***	***193.3***	***31.2***	***208.3***
Pierre_machine_vision_test2_8_July_0003	Top	170.9	38.9	186.0	170.2	39.9	187.0	169.2	39.5	184.0	170.1	39.4	185.7
Taken @ 1m from camera	Bottom	170.8	48.4	194.0	167.2	49.1	191.0	167.4	48.8	192.0	168.5	48.8	192.3
	Av.LED =>	***170.9***	***43.7***	***190.0***	***168.7***	***44.5***	***189.0***	***168.3***	***44.2***	***188.0***	***169.3***	***44.1***	***189.0***
Pierre_machine_vision_test2_8_July_0004	Top	191.2	27.3	202.0	190.8	27.2	201.0	191.0	27.2	202.0	191.0	27.2	201.7
Taken @ 230cm from camera	Bottom	202.5	17.5	208.0	202.6	17.5	208.0	201.5	17.2	207.0	202.2	17.4	207.7
	Av.LED =>	***196.9***	***22.4***	***205.0***	***196.7***	***22.4***	***204.5***	***196.3***	***22.2***	***204.5***	***196.6***	***22.3***	***204.7***
Pierre_machine_vision_test2_8_July_0005	Top	152.7	61.0	173.0	148.6	61.6	170.0	151.9	61.1	174.0	151.1	61.2	172.3
Taken @ 230cm from camera (in Darkness)	Bottom	202.1	24.4	211.0	198.3	24.1	207.0	200.8	24.3	210.0	200.4	24.3	209.3
	Av.LED =>	***177.4***	***42.7***	***192***	***173.45***	***42.85***	***188.5***	***176.4***	***42.7***	***192***	***175.7***	***42.8***	***190.8***

	Red			Green			Blue				Average Σ RGB		
Average of total Ave values for both LEDS	Mean	σ	Median	Mean	σ	Median	Mean	σ	Median		Mean	σ	Median
for the 6 positions =	192.5	28.8	204.2	189.9	30.6	202.8	189.8	30.0	202.4	Σ Ave. =	193.5	32.2	203.1

i.e average of average value from LEDs for the 6 different LED positions

σ = Standard deviation
Σ = Total

Table 6: Green dot camera RGB results.

Machine Vision Image RGB results from post processing of 8th of July experiments with OLYMPUS CAMERA

		Red			Green			Blue			Average Σ RGB		
Name of Image	LED	Mean	σ	Median	Mean	σ	Median	Mean	σ	Median	Mean	σ	Median
p7080092.jpg	Top	254.1	4.8	255.0	128.6	57.4	104.0	156.2	46.1	149.0	179.6	36.1	169.3
Taken @ 15cm from camera	Bottom	250.5	10.5	255.0	182.7	76.6	214.0	192.1	62.9	217.0	208.4	50.0	228.7
	Av.LED =>	***252.3***	***7.7***	***255.0***	***155.7***	***67.0***	***159.0***	***174.2***	***54.5***	***183.0***	***194.0***	***43.1***	***199.0***
p7080093.jpg	Top	230.5	28.8	244.0	80.0	63.3	53.0	106.0	60.0	85.0	138.8	50.7	127.3
Taken @ 30cm from camera	Bottom	249.7	9.7	255.0	105.7	73.1	76.0	130.7	64.3	110.0	162.0	49.0	147.0
	Av.LED =>	***240.1***	***19.3***	***249.5***	***92.9***	***68.2***	***64.5***	***118.4***	***62.2***	***97.5***	***163.4***	***74.4***	***137.2***
p7080094.jpg	Top	246.1	16.6	255.0	89.3	56.8	69.0	126.1	52.3	113.0	153.8	41.9	145.7
Taken @ 50cm from camera	Bottom	252.6	6.4	255.0	126.3	78.0	86.0	153.3	64.3	142.0	177.4	49.6	161.0
	Av.LED =>	***249.4***	***11.5***	***255.0***	***107.8***	***67.4***	***77.5***	***139.7***	***58.3***	***127.5***	***165.6***	***45.7***	***153.3***
p7080095.jpg	Top	239.8	22.0	254.0	93.1	64.0	70.0	124.4	58.7	110.0	152.4	48.2	144.7
Taken @ 100cm from camera	Bottom	251.9	8.1	255.0	131.6	62.8	115.0	157.6	50.6	156.0	180.4	40.5	175.3
	Av.LED =>	***245.9***	***15.1***	***254.5***	***112.4***	***63.4***	***92.5***	***141.0***	***54.7***	***133.0***	***166.4***	***44.4***	***160.0***
p7080096.jpg	Top	253.0	3.1	255.0	165.8	62.5	163.0	192.4	39.4	180.0	203.7	35.0	199.3
Taken @ 115cm from camera	Bottom	249.1	11.1	253.0	151.7	67.9	128.0	172.0	56.3	164.0	190.9	45.1	181.7
	Av.LED =>	***251.1***	***7.1***	***254.0***	***158.8***	***65.2***	***145.5***	***182.2***	***47.9***	***172.0***	***197.3***	***40.1***	***190.5***

	Red			Green			Blue				Average Σ RGB		
Average of total Ave values for both	Mean	σ	Median	Mean	σ	Median	Mean	σ	Median		Mean	σ	Median
LEDS for the 5 positions =	247.7	12.1	253.6	125.5	66.2	107.8	151.1	55.5	142.6	Σ Ave. =	177.3	49.5	168.0

i.e average of average value from LEDs for the 6 different LED positions

σ = Standard deviation
Σ = Total

Table 7: Olympus camera RGB results.

Machine Vision Image RGB results from post processing of 8th of July experiments Yellow dot Camera (N0.1), Green dot camera (No.2) and Olympus camera on red folders

		Red			Green			Blue			Average Σ RGB		
Name of Image	Position	Mean	σ	Median	Mean	σ	Median	Mean	σ	Median	Mean	σ	Median
YELLOW DOT (No.1) Pierre_machine_vision_test3_8_july_0001	Close up	87.4	6.0	87.0	83.1	5.4	83.0	80.2	5.4	221.0	83.6	5.6	130.3
YELLOW DOT (No.1) Pierre_machine_vision_test3_8_july_0002	Far away	133.2	5.5	133.0	107.9	5.6	107.0	6.0	107.0	227.0	82.4	39.4	155.7
		110.3	***5.8***	***110.0***	***95.5***	***5.5***	***95.0***	***43.1***	***56.2***	***224.0***	***83.0***	***22.5***	***143.0***
GREEN DOT (No.2) Pierre_machine_vision_test_8_july_0001	Close up	101.5	9.0	103.0	97.7	9.1	99.0	95.0	8.5	96.0	98.1	8.9	99.3
GREEN DOT (No.2) Pierre_machine_vision_test_8_july_0002	Far away	148.3	1.4	148.0	118.3	1.6	118.0	116.5	1.5	116.0	127.7	1.5	127.3
		124.9	***5.2***	***125.5***	***108.0***	***5.4***	***108.5***	***105.8***	***5.0***	***106.0***	***112.9***	***5.2***	***113.3***
OLYMPUS Camera P7080098	Close up	206.5	3.3	207.0	67.0	3.5	67.0	49.4	3.8	49.0	107.6	3.5	107.7
OLYMPUS Camera P7080099	Far away	193.1	3.1	193.0	64.4	3.1	64.0	52.4	3.6	52.0	103.3	3.3	103.0
		199.8	***3.2***	***200.0***	***65.7***	***3.3***	***65.5***	***50.9***	***3.7***	***50.5***	***105.5***	***3.4***	***105.3***

	Red			Green			Blue				Average Σ RGB		
Average of total Ave values for the RED folder positions =	Mean	σ	Median	Mean	σ	Median	Mean	σ	Median		Mean	σ	Median
	145.0	4.7	145.2	89.7	4.7	89.7	66.6	21.6	126.8	Σ Ave. =	100.4	10.4	120.6

i.e average of average value for RED folder for the 6 different folder positions

n.b. Close up = 0.15m, Far away = 1m

σ = Standard deviation
Σ = Total

Table 8: All 3 cameras RGB results for red folders.

Figure 26: *Eyecam*© image at 0.15*m*

Figure 27: *Eyecam*© in darkness

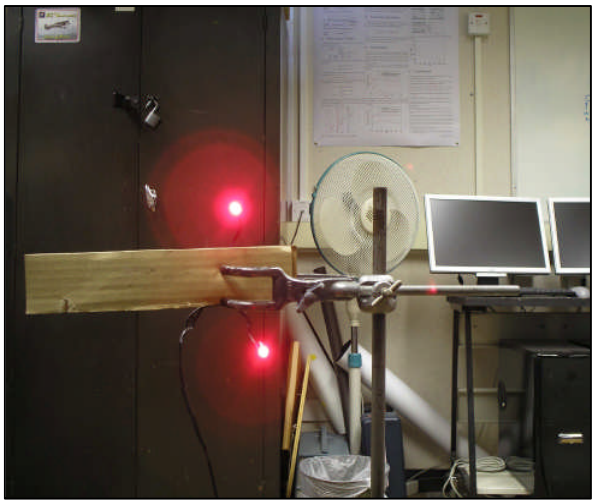

Figure 28: Olympus camera LED test.

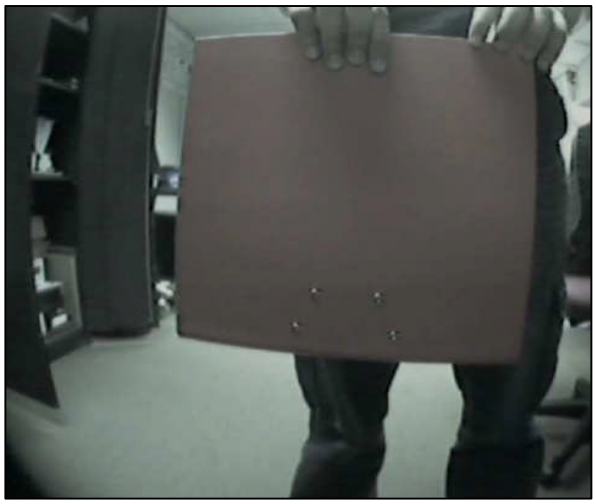

Figure 29: *Eyecam*© red folder test.

6.2.3) Discussion experiment 2:

The results shown in tables 5 to 8 enable the RGB capture for all three cameras to be compared. It can be observed for the 15*cm* case that the red LEDs for the **Yellow dot** and **Green dot** camera are seen as white (similar values across the RGB channels), however the **Olympus camera** has high *Red* saturation and marked lower saturation values for the *Green* and *Blue* channels. Furthermore, the standard deviations for the **Green dot** camera results are much larger than that of the **Yellow dot**. However, the difference between the RGB values for the top and bottom LEDs did not vary significantly for any of the cameras.

Referring to figures 26 to 29, the LEDs as seen by the *Eyecam* appear as a mixture of white with pale red, with the LEDs being easier to distinguish in darkness as would be expected. The image taken by the Olympus camera shows the top and bottom LEDs emitting their bright *Red* colour which is clearly distinct against their respective background.

The final figure 29 illustrates the captured *Eyecam* image for the passive non-emitting test for the red folder. These results in table 8 have much smaller values for the *Red* channel saturation in comparison to the LED tests and a slight reduction would be expected as the folder is a non-emitting source of *Red*. In addition, there is a difference between the *Close up* and *Far away* images for the *Eyecams*, with more *Red* colour being captured at the greater distance. Again the Olympus camera registers higher *Red* colour saturation than either of the *Eyecams* for this test. However, the difference between the results with distance from the target for the Olympus camera differs, with the colour saturation reducing very slightly in the *Red* and *Green* channels. A possible explanation for this difference between the Olympus and *Eyecams* could be the fact that the *Eyecams* are designed for outdoor use at height above a target.

6.2.4) Conclusion experiment 2:

The *Eyecam*© cameras RGB capabilities have been tested and it has been shown that their ability to distinguish the difference between *Red* targets and the background scenery is less sensitive than that of a consumer Digital camera. However, the *Eyecams* provide an adequate means of detecting the difference between the LEDs and their background, thus enabling a basic colour filter process of the image to select the LEDs. Finally, it should be highlighted that the cost, weight and size of the *Eyecams* against their image capturing performance are key factors that need to be considered, should improved image sensitivity be required.

6.3) Experiment 3: Aircraft-LED position estimation 14.07.08 – 17.07.08

6.3.1) Introduction experiment 3:

This experiment is a follow up from experiments 1 and 2 and aims to progress towards establishing the machine vision pose estimation concept. A suitable set of images is required in order to provide a variation in all three axes: *X*, *Y* and *Z*.

Using the knowledge gained in the previous experiments, the selected **Yellow dot** camera's physical properties can be accounted for. The technique and algorithms used to determine the pose estimation, is explained in detail in "*Target position and Trajectory Measurements by Videogrammetry*", COA Report No. 208, S.E Hobbs, 2003 see reference (Hobbs, 2003).

6.3.2) Results experiment 2:

Experimental results from **Monday 14th of July**, for 2 trials: 1) Varying Z and 2) Increasing X then Varying Z
N.B using a right-handed axis system, with A,B,C and D corresponding to LEDS on Aircraft in Clockwise allocation.

Pixel coordinates distance 1 (X = -5.59m)

	A		B		C		D		Camera position		
Image Name	Col	Row	Col	Row	Col	Row	Col	Row	X (m)	Y (m)	Z (m)
Pierre_machine_vision_test_pipercub_14_july_0002	404	216	473	227	405	237	335	231	-5.59	0.00	-0.21
Pierre_machine_vision_test_pipercub_14_july_0003	439	232	507	240	439	252	370	247	-5.59	0.00	-0.31
Pierre_machine_vision_test_pipercub_14_july_0004	461	244	529	251	461	265	392	258	-5.59	0.00	-0.40
Pierre_machine_vision_test_pipercub_14_july_0005	466	262	536	265	469	285	399	281	-5.59	0.00	-0.55
Pierre_machine_vision_test_pipercub_14_july_0006	473	277	543	277	476	300	405	295	-5.59	0.00	-0.70

Pixel coordinates distance 2 (X = -6.23m)

	A		B		C		D		Camera position		
Image Name	Col	Row	Col	Row	Col	Row	Col	Row	X (m)	Y (m)	Z (m)
Pierre_machine_vision_test_pipercub_14_july_0007	389	217	453	224	392	235	330	233	-6.23	0.00	-0.20
Pierre_machine_vision_test_pipercub_14_july_0008	385	232	447	236	387	250	325	247	-6.23	0.00	-0.31
Pierre_machine_vision_test_pipercub_14_july_0009	427	239	489	244	430	259	367	256	-6.23	0.00	-0.40
Pierre_machine_vision_test_pipercub_14_july_0010	431	245	492	247	432	263	370	262	-6.23	0.00	-0.51
Pierre_machine_vision_test_pipercub_14_july_0011	443	260	505	260	445	279	384	274	-6.23	0.00	-0.70

Location of LEDS on aircraft:

	X (m)	Y (m)	Z (m)
A	-0.67	0.00	-0.13
B	-0.12	0.76	-0.02
C	-0.67	0.00	0.07
D	-0.12	-0.76	-0.02

Table 9: Yellow dot camera LED *row* and *column* results, 14th July.

Experimental results from Thursday 17th of July, for 3 trials: 1) Varying Z, 2) Increasing X then Varying Z and 3) Varying Y at constant X and Z
N.B using a right-handed axis system, with A,B,C and D corresponding to LEDS on Aircraft in Clockwise allocation.

Pixel coordinates distance 1 (X = -4.67m)

	A		B		C		D		Camera position		
Image Name	Col	Row	Col	Row	Col	Row	Col	Row	X (m)	Y (m)	Z (m)
Pierre_machine_vision_test_pipercub_17_july_0000	416	210	498	230	416	236	332	288	-4.67	0.00	-0.10
Pierre_machine_vision_test_pipercub_17_july_0002	428	224	511	242	430	250	345	240	-4.67	0.00	-0.20
Pierre_machine_vision_test_pipercub_17_july_0003	429	245	512	259	430	271	346	260	-4.67	0.00	-0.30
Pierre_machine_vision_test_pipercub_17_july_0004	426	264	507	276	426	290	343	278	-4.67	0.00	-0.40
Pierre_machine_vision_test_pipercub_17_july_0005	416	281	497	292	416	306	332	293	-4.67	0.00	-0.50

Pixel coordinates distance 2 (X = -5.86m)

	A		B		C		D		Camera position		
Image Name	Col	Row	Col	Row	Col	Row	Col	Row	X (m)	Y (m)	Z (m)
Pierre_machine_vision_test_pipercub_17_july_0006	375	221	444	238	374	242	312	236	-5.86	0.00	-0.10
Pierre_machine_vision_test_pipercub_17_july_0007	364	233	433	246	364	252	301	246	-5.86	0.00	-0.20
Pierre_machine_vision_test_pipercub_17_july_0008	374	250	444	261	374	270	312	261	-5.86	0.00	-0.30
Pierre_machine_vision_test_pipercub_17_july_0009	386	265	456	275	386	286	324	276	-5.86	0.00	-0.40
Pierre_machine_vision_test_pipercub_17_july_0010	374	276	444	286	372	296	311	286	-5.86	0.00	-0.50

Pixel coordinates distance 3 (X = -5.86)

	A		B		C		D		Camera position		
Image Name	Col	Row	Col	Row	Col	Row	Col	Row	X (m)	Y (m)	Z (m)
Pierre_machine_vision_test_pipercub_17_july_0011	477	280	534	286	476	296	402	286	-5.86	-1.00	-0.50
Pierre_machine_vision_test_pipercub_17_july_0012	523	276	573	284	524	297	447	289	-5.86	-1.50	-0.50
Pierre_machine_vision_test_pipercub_17_july_0013	588	276	631	286	589	298	514	290	-5.86	-2.00	-0.50

Location of LEDS on aircraft:	X (m)	Y (m)	Z (m)
A	-0.67	0.00	-0.13
B	-0.12	0.76	-0.02
C	-0.67	0.00	0.07
D	-0.12	-0.76	-0.02

Table 10: Yellow dot camera LED *row* and *column* results 17th July.

Experimental results from Monday 14th of July, for 3 trials: 1) Varying Z, 2) Increasing X then Varying Z and 3) Varying Y at constant X and Z
N.B using a right-handed axis system, comparing actual measurements with MFITVID.exe results

Results 1)

	X (m)				Y (m)			
Image Name	Actual	Estimated	Error (sim)	Difference	Actual	Estimated	Error (sim)	Difference
Pierre_machine_vision_test_pipercub_14_july_0002	-5.59	-5.183	± 0.09379	0.4070	0	-0.0263	± 0.11201	0.0263
Pierre_machine_vision_test_pipercub_14_july_0003	-5.59	-5.2623	± 0.09599	0.3277	0	0.0282	± 0.11433	0.0282
Pierre_machine_vision_test_pipercub_14_july_0004	-5.59	-5.3192	± 0.09689	0.2708	0	0.0294	± 0.11605	0.0294
Pierre_machine_vision_test_pipercub_14_july_0005	-5.59	-5.2961	± 0.09555	0.2939	0	-0.0143	± 0.11568	0.0143
Pierre_machine_vision_test_pipercub_14_july_0006	-5.59	-5.27	± 0.09422	0.3200	0	0.0062	± 0.11391	0.0062
Pierre_machine_vision_test_pipercub_14_july_0007	-6.23	-5.7768	± 0.11741	0.4532	0	-0.0842	± 0.13974	0.0842
Pierre_machine_vision_test_pipercub_14_july_0008	-6.23	-5.789	± 0.11838	0.4410	0	-0.0147	± 0.14091	0.0147
Pierre_machine_vision_test_pipercub_14_july_0009	-6.23	-5.8288	± 0.11873	0.4012	0	-0.0628	± 0.14305	0.0628
Pierre_machine_vision_test_pipercub_14_july_0010	-6.23	-5.8206	± 0.11864	0.4094	0	0.0618	± 0.14128	0.0618
Pierre_machine_vision_test_pipercub_14_july_0011	-6.23	-5.891	± 0.12086	0.3390	0	0.0166	± 0.14479	0.0166

N.B. Position measured relative to the lead aircraft axis system
sim = simulation

Z (m)				Psi (Azimuth/Yaw) rad		Theta (pitch) rad		Phi (Roll) rad	
Actual	Estimated	Error (sim)	Difference	Estimated	Error (sim)	Estimated	Error (sim)	Estimated	Error (sim)
-0.21	-0.1996	± 0.11191	0.0104	-0.0438	± 0.02251	0.1707	± 0.02197	0.0330	± 0.01889
-0.31	-0.1683	± 0.11528	0.1417	-0.13	± 0.02239	0.1248	± 0.02227	0.0581	± 0.01913
-0.40	-0.2214	± 0.11816	0.1786	-0.1759	± 0.02237	0.1049	± 0.02249	0.0613	± 0.01935
-0.55	-0.3214	± 0.11865	0.2286	-0.1809	± 0.02216	0.0674	± 0.02260	0.1334	± 0.01936
-0.70	-0.3059	± 0.11699	0.3941	-0.1943	± 0.02177	0.028	± 0.02241	0.1481	± 0.01918
-0.20	-0.1867	± 0.13907	0.0133	-0.0119	± 0.02514	0.1655	± 0.02445	0.0784	± 0.02106
-0.31	-0.1847	± 0.14070	0.1253	-0.0127	± 0.02511	0.1340	± 0.02469	0.0959	± 0.02117
-0.40	-0.3154	± 0.14436	0.0846	-0.0948	± 0.02523	-0.0948	± 0.02523	0.1086	± 0.02147
-0.51	-0.185	± 0.14237	0.3250	-0.1232	± 0.02482	0.0911	± 0.02480	0.1327	± 0.02127
-0.70	-0.2533	± 0.14674	0.4467	-0.1390	± 0.02498	0.0678	± 0.02518	0.1279	± 0.02157

Table 11: Yellow dot camera pose estimation results, 14th of July.

Experimental results from Thursday 17th of July, for 3 trials: 1) Varying Z, 2) Increasing X then Varying Z and 3) Varying Y at constant X and Z
N.B using a right-handed axis system, comparing actual measurements with MFITVID.exe results

Results 1)

	X (m)				Y (m)			
Image Name	Actual	Estimated	Error (sim)	Difference	Actual	Estimated	Error (sim)	Difference
Pierre_machine_vision_test_pipercub_17_july_0000	-4.67	-4.1217	±0.05860	0.5483	0	0.1589	±0.06957	0.1589
Pierre_machine_vision_test_pipercub_17_july_0002	-4.67	-4.3477	±0.06514	0.3223	0	-0.0909	±0.07783	0.0909
Pierre_machine_vision_test_pipercub_17_july_0003	-4.67	-4.3326	±0.06485	0.3374	0	-0.0406	±0.07754	0.0406
Pierre_machine_vision_test_pipercub_17_july_0004	-4.67	-4.368	±0.06613	0.3020	0	-0.0042	±0.07919	0.0042
Pierre_machine_vision_test_pipercub_17_july_0005	-4.67	-4.3264	±0.06518	0.3436	0	-0.0083	±0.07762	0.0083
Pierre_machine_vision_test_pipercub_17_july_0006	-5.86	-5.3957	±0.10209	0.4643	0	0.0524	±0.12263	0.0524
Pierre_machine_vision_test_pipercub_17_july_0007	-5.86	-5.392	±0.10234	0.4680	0	0.0212	±0.12170	0.0212
Pierre_machine_vision_test_pipercub_17_july_0008	-5.86	-5.3644	±0.10159	0.4956	0	0.0229	±0.12130	0.0229
Pierre_machine_vision_test_pipercub_17_july_0009	-5.86	-5.3509	±0.10113	0.5091	0	0.0286	±0.12131	0.0286
Pierre_machine_vision_test_pipercub_17_july_0010	-5.86	-5.3112	±0.09985	0.5488	0	0.1161	±0.11901	0.1161
Pierre_machine_vision_test_pipercub_17_july_0011	-5.86	-5.5740	±0.10664	0.2860	-1.00	-0.0024	±0.12536	0.9976
Pierre_machine_vision_test_pipercub_17_july_0012	-5.86	-6.1076	±0.12192	0.2476	-1.50	-0.0715	±0.14808	1.4285
Pierre_machine_vision_test_pipercub_17_july_0013	-5.86	-7.1922	±0.15493	1.3322	-2.00	-0.0556	±0.19365	1.9444

N.B. Position measured relative to the lead aircraft axis system (and in a NED axis)
sim = simulation

Z (m)				Psi (Azimuth/Yaw) rad		Theta (pitch) rad		Phi (Roll) rad	
Actual	Estimated	Error (sim)	Difference	Estimated	Error (sim)	Estimated	Error (sim)	Estimated	Error (sim)
-0.10	-0.1327	±0.07061	0.0327	-0.1387	±0.01758	0.1056	±0.01758	0.3471	± 0.01495
-0.20	-0.1971	±0.07875	0.0029	-0.0744	±0.01861	0.1546	±0.01853	-0.0088	± 0.01580
-0.30	-0.1976	±0.07880	0.1024	-0.0897	±0.01841	0.1079	±0.01861	0.0111	± 0.01578
-0.40	-0.2078	±0.08058	0.1922	-0.0901	±0.01849	0.0675	±0.01887	0.0179	± 0.01594
-0.50	-0.1667	±0.07880	0.3333	-0.0666	±0.01818	0.0223	±0.01869	0.0100	± 0.01574
-0.10	-0.2636	±0.12268	0.1636	0.0077	±0.02363	0.1678	±0.02307	-0.0136	± 0.01982
-0.20	-0.1611	±0.12179	0.0389	0.0350	±0.02327	0.1260	±0.02300	0.0015	± 0.01967
-0.30	-0.2025	±0.12183	0.0975	0.0119	±0.02315	0.0969	±0.02310	0.0020	± 0.01967
-0.40	-0.2486	±0.12218	0.1514	-0.0155	±0.02319	0.0712	±0.02319	0.0108	± 0.01969
-0.50	-0.1916	±0.11981	0.3084	-0.0041	±0.02270	0.0366	±0.02296	0.0023	± 0.01946
-0.50	-0.0178	±0.12778	0.4822	-0.1904	±0.02276	0.0010	±0.02331	0.0011	± 0.02005
-0.50	-0.3968	±0.15492	0.1032	-0.2711	±0.02444	0.0511	±0.02533	0.0581	± 0.02205
-0.50	-0.7545	±0.2115	0.2545	-0.3998	±0.02695	0.0805	±0.02864	0.0749	± 0.02573

Table 12: Yellow dot camera pose estimation results, 17th July.

Results 4)
Altering both row and column pixel readings by 2 pixels for selected images:

	X (m)				Y (m)			
Image Name	Actual	Estimated	Error (sim)	Difference Res 1	Actual	Estimated	Error (sim)	Difference Res 1
Pierre_machine_vision_test_pipercub_17_july_0002	-4.67	-4.3493	± 0.06517	0.0016	0.00	-0.0914	± 0.07787	0.0005
Pierre_machine_vision_test_pipercub_17_july_0003	-4.67	-4.3353	± 0.06489	0.0027	0.00	-0.0409	± 0.07760	0.0003
Pierre_machine_vision_test_pipercub_17_july_0004	-4.67	-4.3712	± 0.10126	0.0032	0.00	-0.0042	± 0.07926	0.0000
Pierre_machine_vision_test_pipercub_17_july_0007	-5.86	-5.3878	± 0.10126	0.0042	0.00	0.0204	± 0.12160	0.0008
Pierre_machine_vision_test_pipercub_17_july_0008	-5.86	-5.3621	± 0.10155	0.0023	0.00	0.0224	± 0.12124	0.0005
Pierre_machine_vision_test_pipercub_17_july_0009	-5.86	-5.3506	± 0.10112	0.0003	0.00	0.0283	± 0.12130	0.0003
Pierre_machine_vision_test_pipercub_17_july_0011	-5.86	-5.5837	± 0.10684	0.0097	-1.00	-0.0016	± 0.12560	0.0001
Pierre_machine_vision_test_pipercub_17_july_0012	-5.86	-6.1224	± 0.12223	0.0148	-1.50	-0.0694	± 0.14849	0.0005
Pierre_machine_vision_test_pipercub_17_july_0013	-5.86	-7.2151	± 0.15544	0.0229	-2.00	-0.0512	± 0.19435	0.0012

Z (m)				Psi (Azimuth/Yaw) rad		Theta (pitch) rad		Phi (Roll) rad	
Actual	Estimated	Error (sim)	Difference Res 1	Estimated	Error (sim)	Estimated	Error (sim)	Estimated	Error (sim)
-0.20	-0.1979	± 0.07886	0.0008	-0.0786	± 0.01859	0.1503	± 0.01855	-0.0086	± 0.01581
-0.30	-0.1983	± 0.07760	0.0007	-0.0939	± 0.01839	0.1035	± 0.01863	0.0113	± 0.01579
-0.40	-0.2084	± 0.08068	0.0006	-0.0943	± 0.01847	0.0629	± 0.01888	0.0181	± 0.01595
-0.20	-0.1612	± 0.12173	0.0001	0.0308	± 0.02324	0.1215	± 0.02301	0.0016	± 0.01966
-0.30	-0.2026	± 0.12180	0.0001	0.0077	± 0.02313	0.0923	± 0.02311	0.0021	± 0.01966
-0.40	-0.2487	± 0.12220	0.0001	-0.0197	± 0.02305	0.0666	± 0.02320	0.011	± 0.01969
-0.50	-0.1948	± 0.02276	0.1770	-0.1948	± 0.02276	-0.0035	± 0.02333	0.0012	± 0.02008
-0.50	-0.3991	± 0.15550	0.0023	-0.2753	± 0.02442	0.0464	± 0.02535	0.0585	± 0.02208
-0.50	-0.7593	± 0.21219	0.0048	-0.4038	± 0.02693	0.0759	± 0.02867	0.0755	± 0.02577

Table 13: Yellow dot camera pose estimation results, 17th July, with 2 pixel differences.

6.3.3) Discussion experiment 3:

Two experiments were performed in order to provide sufficient data for the analysis using the **Mfitvid** program. In the first experiment (14th July) there were only two sets of images taken varying the cameras position only in *X* and *Z* axes, thus, enabling the performance of the pose estimation program to be determined. For the second experiment (17th July) an additional test varying the camera position in the *Y* axes was included which enabled a complete test of the pose software in all three axes to be performed.

Referring to tables 9 and 10 the *row* and *column* positions for each of the four LEDs are listed for all of the images captured. A table of the location of each LED with respect to the axes origin is included with both sets of results. The labelling of the LEDs was done in a clockwise manner (see appendix experiment 3 diagram E3.2 for an image) starting at the 12 o'clock position with position *A* (located at the top of the fin) followed by *B* (at the tip of the starboard wing) then *C* (at the bottom of the fin) and finishing with *D* (at the port wing tip), this information for each image was stored in a *txt* file for later use in the **AVI1** program.

Using the **Mfitvid** program the pose estimation of the camera relative to the target object (the Pipercub aircraft, identified by the rear mounted LEDs) was determined for each image in turn, this process required considerable manual configuration and manipulation of the **AVI1** output data. The results are presented in tables 11 and 12 with the measured *X, Y* and *Z* data compared to that predicted. In addition the angular pose of the camera in yaw, pitch and roll has been included.

Comparing the measured and estimated results for the *X, Y* and *Z* values in the first experiment, 14th of July (table 11), the largest difference for the *X* readings is 0.45*m*. This occurs for the first reading at the -6.23*m* distance (for an elevation value of -0.2*m*) and this difference is the same for the last *Z* reading of -0.70*m*, again at the -6.23*m* value. The *Y* values have fewer differences with the maximum difference of 0.08*m* occurring also for the -6.23*m* readings (at an elevation of -0.2*m*). These differences may be due to the fact that

during the vision trials the camera's position was "off-centre" from the target in *X* and *Z* (being above or below it) unlike in the *Y*, axis which was not varied from its initially aligned position. In addition, the three pose angles estimated are small, as would be expected for a wings level position and a correctly aligned camera. The values are less than 10 degrees with small uncertainties of 1 degree or less.

Referring to the second set of experimental results (see table 12) taken on the 17th of July, where an additional trial which included varying in the *Y* axis was performed. This experiment highlighted the difficulty with estimating the pose position when the *Field of View* is not perpendicular to the target object. In the *X* direction the largest difference occurred for the maximum *Y* displacement of -2*m* with an overestimation of 1.332*m* in the X *axis* predicted by the program. Again this same *Y* displacement produced the largest error in the *Y* estimation with an underestimation of 1.944*m* by the algorithm. The largest difference in the Z direction occurred for the -1m *Y* displacement with an underestimation of 0.48*m*. Therefore, the ability to determine the pose of the camera relative to the object is affected when observing a target from the side / "off-centre" position. This is further highlighted when analysing the number of iterations required for a solution to be reached between *image 05* and *image 13*; the first required only 2 iterations while the latter required 28.

In addition, the in-built error estimation for the **Mfitvid** program did not compare well with the "real" error differences determined by measuring. For the majority of the cases the error was underestimated. Using the Correlation matrix for the *image 13* result (see appendix 8) the relationships between *Y* and the 5 variables can be seen:

- Y and X, -0.00743
- Y and Z, -0.00612
- Y and ψ, -0.96982
- Y and θ, -0.111084
- Y and φ, 0.30110

The above results show that there is large negative correlation between Y and ψ. Furthermore, a very small negative correlation can be seen between X, Z, θ and Y and finally, the roll angle φ, has a positive medium correlation with Y. From these relationships it can be said that further changes to Y will result in poorer X, Z and θ estimations by the **Mfitvid** program. However, it should be highlighted that the camera calibration is only of first order. Therefore, a first step to understanding the error discrepancy would be to obtain a higher order camera calibration.

Comparing the pose angles determined for the X = -4.67m and X = -5.86m distances (see table 12), the largest angles for yaw and pitch occur for X = -5.86m with Z = -0.1m in the order of 10 degrees. However, a larger than expected roll angle of 20 degrees is predicted for the X = -4.67m and Z = -0.1m case. After calculating the trigonometry this last result would require the camera to be located at Y = -1.59m which is clearly not the case, therefore this result is anomalous. However, the other results are within acceptable values of less than 10 degrees. Referring to the Y displacement results in table 12 for the pose angles, it is interesting to observe the yaw angles as these angles agree well with those calculated by trigonometry, using the X and Y displacement values. Finally, the pitch and roll angles remain close to zero which is as expected.

Furthermore, an attempt to investigate the effect of changing the pixel coordinates for the *row* and *column* position of each LED by two pixels was performed (see table 13). This was done in order to determine the sensitivity of the program to mistakes in the actual location of the LED's centre in establishing the target object's pose. Overall, there are no major differences between the X, Y and Z distances with respect to the original values (table 12) greater than 0.02m. In this respect, it should be noted that the anomalous result occurring at X = -5.86m, Y = -1m and Z = -0.1m is excluded (which estimates a difference of 0.2m). Finally, observing the comparison between the pose angles the differences are of the order of 1 to 2 degrees with the original angles. Therefore, it can be seen that this simple investigation indicates that the algorithm is suitably well mannered, that small errors in pixel coordinates do not create large pose estimation.

6.3.4) Conclusion:

Using the **AVI1** and **Mfitvid** programs provided by (Hobbs, 2003) a technique enabling the pose estimation of a camera relative to a target has been trailed. This method provides reliable results in the *X*, *Y* and *Z* directions and yaw (ψ), pitch (θ) and roll (φ) angles provided the camera is perpendicular to and in-line with the centre of the object. However, there are a number of problems with the pose estimation when the camera is displaced both in the Y direction and for low *Z* (elevation) values. The angular position of the camera has also been estimated for the steady wing level condition at different *–X* distances and the results for yaw, pitch and roll reflect this with their small estimated angles

An additional investigation into the effect of pixel errors on the final pose estimation has also been performed. For errors of 2 pixels in both *row* and *column* coordinates **Mfitvid** is still capable of estimating the pose of the camera correctly with minimal differences in comparison with the zero error input data. Thus the position estimation exhibits good robustness with respect to pixel errors.

o0o…o0o…o0o

7) Overall Discussion:

During the literature review the author performed background research and was able to gain a more in-depth understanding of the topics relating to machine vision and autonomous navigation. Following the review several camera calibration articles were found which proposed different calibration models and techniques. An initial investigation into the model proposed by (Heikkila and Silven, 1997) was made, however, the author decided to perform only a first order calibration in order to progress towards firstly proving the concept. An extensive amount of research was also found relating to the pose position problem of the follower to leader/target scenario. The proposed techniques used a combination of machine vision and a means of measuring ownship movement (an Inertial Navigation System or GPS) to generate the necessary guidance to navigate the follower relative to the leader/target.

An important aspect of the machine vision for autonomous navigation concept was found to have been overlooked in the literature that was found. This related to investigating the effects of atmospheric interference on visual light transmission, which is necessary in order to accurately navigate using machine vision. The author was able to find sources relating to this topic, however no specific research was found to address the precise topic of visual light transmission for aircraft/target tracking. Therefore, using the available information a brief study into the atmospheric effects was made. The information gained enabled the author to establish suitable properties for the leader/target marker lights.

The machine vision element enables the pose information of the leader/target's markers to be extracted from the follower's camera. In order to determine the 3-*D* position of the follower a suitable navigation reference frame needed to be adopted to formulate the displacement vectors between the follower and leader/target. Using the standard North, East and Down (*NED*) reference frame, the origin was chosen to lie at the centre of gravity of the leader/target. Furthermore, the case of formatting onto the leader/target from a

distance was analysed, this highlighted the necessary ability of the camera to resolve the line of sight angles between the follower and leader/target.

Once the reference frame of the system had been defined the relative displacement vectors could be defined and differentiated to yield the relative velocity and relative acceleration respectively. Having done this the system was then represented in state variable form in order to create a model for the pose problem. Using the reference axes the pose angles could then in turn be defined. However, as previously outlined the use of an INS system will be needed to verify the model and provide a means of comparing the visual input data to that physically measured (see Further work section for more details).

The practical element to this thesis included performing 3 experiments, with each experiment leading towards the final experiment which proved the machine vision autonomous navigation concept. Discussions for each individual experiment can be found in the discussion section of each report. However, the key outcomes were that a first order model for the *Eyecam*© was established. The ability of the *Eyecam*© to distinguish *RGB* was evaluated and found to have a deficiency in being able to clearly distinguish different colours. Finally, the concept proving experiment to determine the pose of the *Eyecam*© relative to a lead model aircraft provided promising results for the current trial system.

A list of five key points for further work has been included in the section under the same heading.

o0o…o0o…o0o

8) Thesis Outcome:

For the successful realisation of the project the following key tasks have been performed:

Theoretical:

- Review of current research and present capabilities regarding the pose estimation arising from the *follower – leader* formation and *follower – drogue* scenarios.
- Understanding of camera calibration, machine vision algorithms and an introduction to *C*-programming in order to use the pose estimation program.
- Investigation of the properties of visual wavelengths in the atmosphere.
- Examination of digital photography and image processing.

Practical:

- First order calibration of the department's two CMOS micro-cameras (ALM-2451G/4RX).
- Investigation into the camera's *Red Green Blue* (*RGB*) capture of the LED colour, as used on the leader/target under different lighting conditions.
- Creation of a suitable data bank of photos acquired from the cameras.
- Testing of the **Mfitvid** pose algorithm from (Hobbs, 2003) for the follower-leader scenario.

Having synthesised the necessary information and completed the above tasks a sound introduction has been made and a solid starting point established for further research by a following MSc student. Suggestions by the author for further work have been made and can be seen overleaf in section 10.

o0o- Intentionally left blank -o0o

9) Overall Conclusion:

- An initial investigation into current literature relating to the Machine Vision and Autonomous Navigation topic has been performed. Several articles concerning pose estimation from target recognition were analysed. These papers were used to formulate the pose estimation problem in a *NED* axis system.

- A brief study into the properties of atmospheric interference of visible light emitted with altitude has been undertaken. The initial findings are, firstly, that at lower altitudes (0 - 5*km*) blue wavelength light has fewer attenuating factors, and secondly, that for higher altitudes red wavelength light is the least affected by this type of interference.

- A first order camera calibration has been successfully performed for the *Eyecam*©. This assumes a linear relationship for the lens distortion from the centre of each captured image.

- The *Eyecam's RGB* colour channel capturing capability has been tested. The test results have highlighted that the *Eyecam*© has difficulty in clearly distinguishing individual colours. Similar values on all three of the colour channels were recorded for an LED emitting Red light, which in the captured images corresponded to a Rose coloured LED.

- An attempt at developing a suitable system capable of providing ownship pose estimation in a follower–leader/target scenario has been made. The initial experimental system was configured and indoor trials of the Machine Vision Autonomous Navigation System produced promising results, thus enabling the validation of the systems concept. Furthermore, complete data sets of the images used and data produced by the pose estimation program have been gathered.

o0o- Intentionally left blank -o0o

10) Future work:

As a result of the research work that has been undertaken, the author can outline five key points which any further work will need to address.

1) *Improve the camera calibration*: The current experimental work utilised a 1st order calibration model in order to start the project. A higher order calibration will enable an improved mapping of the target's image to CCD. Increasing the order of calibration will help to further reduce additional "*skew*" errors due to the lens distortion or aberrations. Initial calibration work should be focused on obtaining a 3rd order polynomial fit, as preformed in the research of (Hobbs, 2003), who found that this lead to satisfactory results. Subsequently, experiment 3 should be repeated and the errors analysed. Should the camera not perform satisfactorily, a suitable substitute will need to be found with the same compact and lightweight characteristics as the *Eyecam*©.

2) *Integrate the image processing*: The author found that using both the **AVI1** and **Mfitvid** programs in sequence during the post image capture processing required a considerable amount of data manipulation and substantial expenditure of time. This step could benefit from the integration of both programs into one, therefore removing the need to create and manage the intermediate files when transferring between the two programs. In order to successfully complete this task a sound understanding of *C* programming will be essential.

3) *Active image scanning*: In keeping with the autonomous navigation project brief, a means of eliminating the current need to process the images offline following the image capture will need to be established. Thus a suitable next step will be to progress towards more real-time image processing. It will be essential to develop a pattern matching algorithm that takes advantage of the LEDs' colours and position within the target reference frame. The capacity of the Eyecams *RGB* capture has already been analysed but this alone will not be able to provide a sufficiently robust means of capturing the target's pose information. A possible solution to this last point could be to pulsate the LEDs,

however this will further complicate the image processing because of the additional images needed to determine the LED pulses.

4) *Increase LED power*: Currently, the pose estimation technique uses four LEDs rated by the manufacturer capable providing a light intensity that ranges from 1600 to 2000*mcd* (approximately equal to 0.428 *Lumens*). Following, the outdoor trials performed (see appendix 6) the performance of these LEDs was found to be inadequate since they did not produce sufficient light intensity against a light coloured background during daylight. This problem will need to be addressed before the in-flight trials of the vision system begin. Ideally, a supplier capable of providing higher intensity LEDs will need to be identified. However, the current LED lighting is sufficient for performing the indoor trials which will be necessary for further developing the image processing software.

5) *Incorporate an Inertial Navigation System*: Current work on determining the follower's pose relative to the leader has only addressed the static pose problem. Thus, the issue of identifying which out of the two (the follower or leader/target) has moved when in-flight will become a pertinent issue. During the literature review suitable solutions to this problem were established. The most complete solution included integrating an Inertial Navigation System (INS) into the follower. Once installed, the velocity and acceleration measurements for the followers' ownship become readily available. However, the integration and co-ordination of the INS and vision information into the autonomous navigation algorithm will require a substantial amount of work and should be undertaken once the previous four steps have been completed.

References:

Campa, G., Napolitano, M. R., Perhinschi, M., Fravolini, M. L., Pollini, L. and Mammarella, M. (2007), "Addressing pose estimation issues for machine vision based UAV autonomous serial refuelling", *The Aeronautical Journal*, vol. 111, no. 1120, pp. 389-396.

Chen, W. and O'Neil, W. (2003), "See and Avoid Sensor System Design Part I - Coverage Modeling", *2nd AIAA "Unmanned Unlimited" Systems, Technologies, and Operations - Aerospace, Land, and Sea Conference, Workshop and Exhibition; San Diego, CA; USA; 15-18 Sep. 2003*, Vol. AIAA Paper 2003-6606, AIAA, 1801 Alexander Bell Drive, Suite 500, Reston, VA, .

Crowther, B. (2003), "Flocking of autonomous unmanned air vehicles", *Aeronautical Journal*, vol. 107, no. 1068 SPEC, pp. 99-109.

Denny, Ronald C. and Sinclair, R. (1987), *Visible and Ultraviolet Spectroscopy (Analytical Chemistry by Open Learning)*, 1st ed, John Wiley & Sons, UK.

Elterman, L. (1968), *UV, Visible and IR Attenuation for Altitudes up to 50 km*, AFCRL-68-0153, Airforce Cambridge Research Laboratories, Bedford, Massachusetts.

Gardener, R. (2008), "Tigers in the sky", *Aerospace International*, vol. 35, no. 2, pp. 10.

Graham, R. (2005), *The Digital Image*, Rev. ed, Whittles Publishing Ltd., Dunbeath, UK.

Heikkilä, J. and Silvén, O. (1996), "Accurate 3-D measurement using a single video camera", *International Journal of Pattern Recognition and Artificial Intelligence*, vol. 10, no. 2, pp. 139-149.

Heikkila, J. and Silven, O. (1997), "Four-step camera calibration procedure with implicit image correction", *Proceedings of the 1997 IEEE Computer Society Conference on Computer Vision and Pattern Recognition; San Juan, PR; USA; 17-19 June. 1997*, IEEE, Los Alamitos, CA, United States, pp. 1106.

Hobbs, S. (2003), "Target Position and Trajectory Measurements by Videogrammetry", *College of Aeronautics*, vol. report 0208.

Johnson, E. N., Calise, A. J., Watanabe, Y., Ha, J. and Neidhoefer, J. C. (2007), "Real-time vision-based relative aircraft navigation", *Journal of Aerospace Computing, Information and Communication,* vol. 4, no. 4, pp. 707-738.

Kimmett, J., Valasek, J. and Junkins, J. L. (2002), "Autonomous aerial refueling utilizing a vision based navigation system", *AIAA Guidance, Navigation, and Control Conference and Exhibit, Monterey, CA; UNITED STATES; 5-8 Aug. 2002,* Vol. AIAA Paper 2002-4469, AIAA, 1801 Alexander Bell Drive, Suite 500, Reston, VA, .

Ma, L., Stepanyan, V., Cao, C., Faruque, I., Woolsey, C. and Hovakimyan, N. (2006), "Flight Test Bed for Visual Tracking of Small UAVs", *2006 AIAA Guidance, Navigation, and Control Conference and Exhibit; Keystone, CO; USA; 21-24 Aug. 2006,* Vol. AIAA Paper 2006-6609, AIAA, 1801 Alexander Bell Drive, Suite 500, Reston, VA, .

Motta, J. (1999), *Optimised Robot Calibration Using a Vision-based Mesurement System with a Single Camera* (unpublished PhD thesis), Cranfield University, Cranfield, Bedfordshire.

Narasimhan, S. G. and Nayar, S. K. (2002), "Vision and the atmosphere", *International Journal of Computer Vision,* vol. 48, no. 3, pp. 233-254.

Nishita, T. (1987), "Shading model for atmospheric scattering considering luminous intensity distribution of light sources", *Computer Graphics (ACM),* vol. 21, no. 4, pp. 303-310.

Norris, V. J.,Jr, Evans, R. S. and Currie, D. G. (1999), "Performance comparison of visual, infrared, and ultraviolet sensors for landing aircraft in fog", *Enhanced and synthetic vision 1999; Proceedings of the Meeting, Orlando, FL; UNITED STATES; 5-6 Apr. 1999,* Bellingham, WA: Society of Photo-Optical Instrumentation Engineers (SPIE Proceedings. Vol. 3691), .

Oh, S. and Johnson, E. N. (2007), "Relative Motion Estimation for Vision-based Formation Flight using Unscented Kalman Filter", *2007 AIAA Guidance, Navigation, and Control Conference and Exhibit; Hilton Head, SC; USA; 20-23 Aug. 2007,* Vol. AIAA Paper 2007-6866, AIAA, 1801 Alexander Bell Drive, Suite 500, Reston, VA, .

Pollini, L., Innocenti, M. and Mati, R. (2005), "Vision Algorithms for Formation Flight and Aerial Refueling with Optimal Marker Labeling", *2005 AIAA Modeling and Simulation Technologies Conference and Exhibit; San Francisco, CA; USA; 15-18 Aug. 2005*, Vol. AIAA Paper 2005-6010, AIAA, 1801 Alexander Bell Drive, Suite 500, Reston, VA, .

Sattigeri, R., Calise, A. J., Kim, B. S., Volyansky, K. and Kim, N. (2005), "6-DOF Nonlinear Simulation of Vision-based Formation Flight", *2005 AIAA Guidance, Navigation, and Control Conference and Exhibit; San Francisco, CA; USA; 15-18 Aug. 2005*, Vol. AIAA Paper 2005-6002, AIAA, 1801 Alexander Bell Drive, Suite 500, Reston, VA, .

Tandale, M. D., Bowers, R. and Valasek, J. (2005), "Robust Trajectory Tracking Controller for Vision Based Probe and Drogue Autonomous Aerial Refueling", *2005 AIAA Guidance, Navigation, and Control Conference and Exhibit; San Francisco, CA; USA; 15-18 Aug. 2005*, Vol. AIAA Paper 2005-5868, AIAA, 1801 Alexander Bell Drive, Suite 500, Reston, VA, .

Valasek, J., Gunnam, K., Kimmett, J., Tandale, M. D., Junkins, J. L. and Hughes, D. (2005), "Vision-Based Sensor and Navigation System for Autonomous Air Refueling", *AIAA Journal of Guidance, Control, and Dynamics*, vol. 28, no. 5, pp. 979-989.

Watanabe, Y., Johnson, E. N. and Calise, A. J. (2007), "Stochastically Optimized Monocular Vision-Based Guidance Design", *2007 AIAA Guidance, Navigation, and Control Conference and Exhibit; Hilton Head, SC; USA; 20-23 Aug. 2007*, Vol. AIAA Paper 2007-6865, AIAA, 1801 Alexander Bell Drive, Suite 500, Reston, VA, .

Woffinden, D. C. and Geller, D. K. (2007), "Relative Angles-Only Navigation and Pose Estimation for Autonomous Orbital Rendezvous", *AIAA Journal of Guidance, Control, and Dynamics*, vol. 30, no. 5, pp. 1455-1469.

o0o- Intentionally left blank -o0o

Appendix 1: Kingbright© L-53SRC-DW 5*mm* Superbright Red LED specifications.

Part No.	Dice	Lens Type	Iv (mcd) @ 20 mA		Viewing Angle
			Min.	Max.	2θ1/2
L-53SGC	SUPER BRIGHT GREEN (GaP)	WATER CLEAR	100	300	30°
L-53SRC-A	SUPER BRIGHT RED (GaAlAs)	WATER CLEAR	300	400	
L-53SRC-B			400	500	
L-53SRC-C			500	1000	
L-53SRC-DU			1000	1300	
L-53SRC-DV			1300	1600	
L-53SRC-DW			1600	2000	
L-53SRC-E			2000	3500	
L-53SRC-F			3500	4500	

Notes:
1. θ1/2 is the angle from optical centerline where the luminous intensity is 1/2 the optical centerline value.
2. Luminous intensity/ luminous Flux: +/-15%.

Table A1.1[t]: Manufacturer's specifications for LED Luminosity and viewing angle.

Electrical / Optical Characteristics at TA=25°C

Symbol	Parameter	Device	Typ.	Max.	Units	Test Conditions
λpeak	Peak Wavelength	Super Bright Red	660		nm	IF=20mA
λD [1]	Dominant Wavelength	Super Bright Red	640		nm	IF=20mA
Δλ1/2	Spectral Line Half-width	Super Bright Red	20		nm	IF=20mA
C	Capacitance	Super Bright Red	45		pF	VF=0V;f=1MHz
VF [2]	Forward Voltage	Super Bright Red	1.85	2.5	V	IF=20mA
IR	Reverse Current	Super Bright Red		10	uA	VR = 5V

Notes:
1.Wavelength: +/-1nm.
2. Forward Voltage: +/-0.1V.

Table A1.2[k]: Manufacturer's red LED light wavelength specifications.

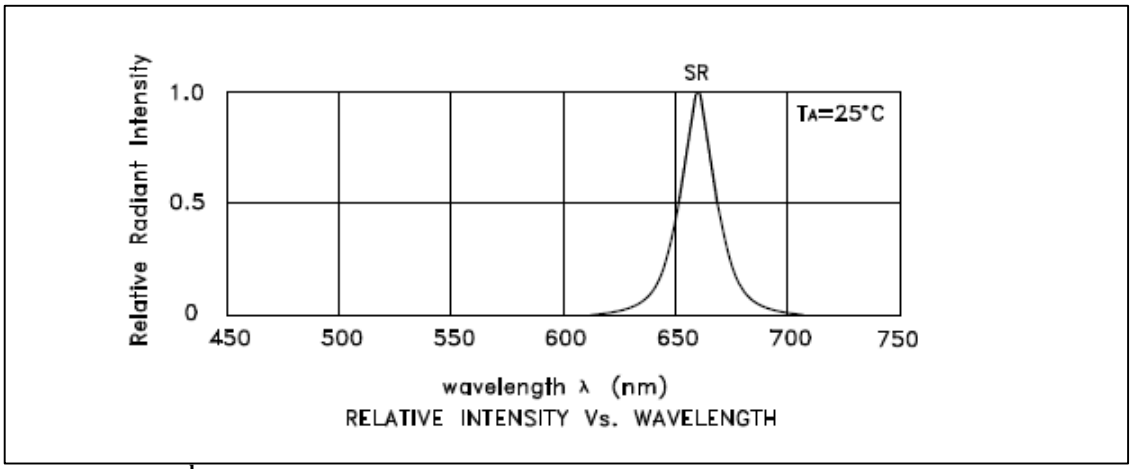

Graph A1.1 [k]: Manufacturer's specifications red LED light intensity with wavelength.

[t] Kingbright L-53SRC-E, www.kingbright.com

Appendix 2: Initial target cut outs.

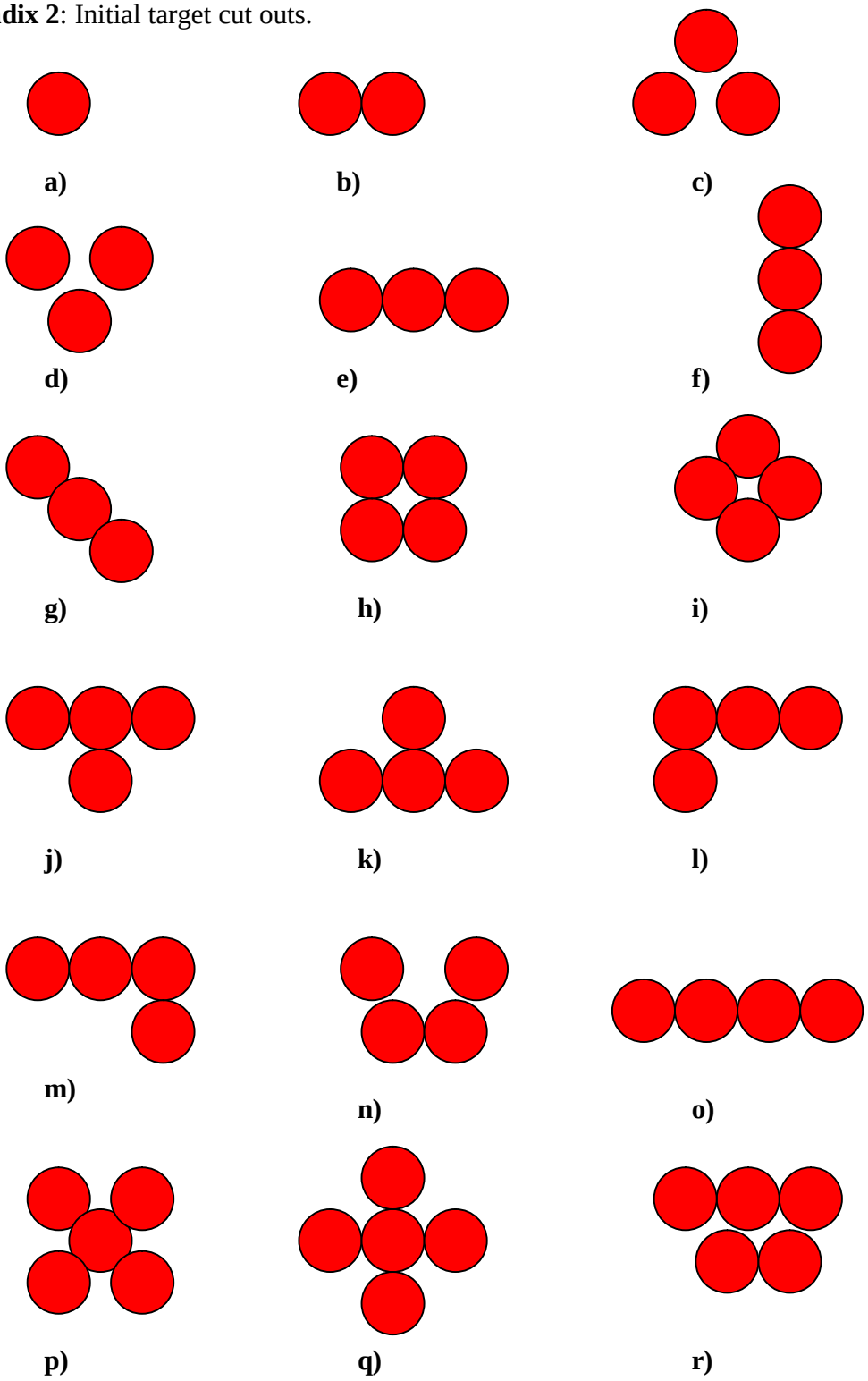

Appendix 3: Eyecam technical specifications

Technical Specifications

PLEASE NOTE: EYECAM DOES NOT CURRENTLY INCLUDE AN AUDIO FEATURE

Eyecam 2.4GHz Transmitter

One Channel:	2.4GHz Frequency band
RF output power:	EC R&TTE Compliant
Operating power:	DC4.8-7.2V, regulated
Power consumption:	100mA
Size:	15x22x32mm
Antenna:	Omni-directional
Transmitting Range:	300M (Line-of-sight)
Weight:	16 grams
Temperature:	-10 to +50°C

Eyecam CMOS Colour Camera

Pixels:	365K (PAL), 250 (NTSC)
Resolution:	Horizontal 380 TV lines
Auto Electronic Exposure:	1/60 - 1/15000 sec.
Automatic Exposure / Gain / White balance.	
Minimum Illumination:	<3 Lux@ f1.2
Signal to Noise Ratio:	>48dB
Board Lens:	3.66mm/view angle: 92
Field Angle:	92 degrees
Size:	15 x 15 mm, board lens

Eyecam Receiver

Frequency:	2.4GHz frequency band
Video input/output:	1V p - p /75 ohm
Audio input/output:	0.8V / 600 ohm
Antenna:	60 degree directional
Audio Bandwidth:	50 - 17000 Hz
Operating Power:	DC 12V, regulated
Power Consumption:	180mA
Size:	150 x 88 x 40 mm

Figure A3.1: Manufacturer's specifications for the *Eyecam*.

Appendix 4: LED circuit

In keeping with the mission statement of using "solely Machine Vision" in order to determine the pose estimation of the camera relative to the model aircraft, four Red LEDs were required to create suitable targets on the model. These targets were located at known points and were described by their 3D position relative to the model aircrafts' centre of gravity. The targets were required to be easily captured by the *Eyecam*© from a distance and therefore needed to stand out from the background environment. The four target LEDs (see appendix 1 for full specifications) were chosen as they emitted an intense Red wavelength of 660n*m*.

A suitable solution for the LEDs would have been to purchase a constant current LED. Such an LED is able to be connected to any power source ranging between 4*V* to 30*V*, however, this option was unavailable. Therefore, the author decided to create a simple circuit with four LEDs divided into two parallel circuits forming a 2×2 array (see figure A4.1 below). Such a circuit also optimised the number of components required, more importantly this allowed the option of easily connecting another parallel loop of two LEDs should they be required for later work.

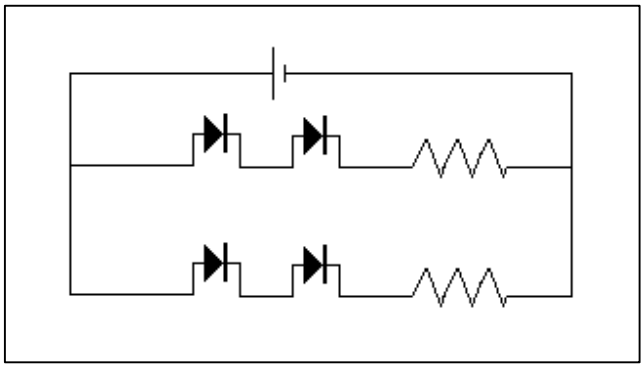

Figure A4.1: Circuit diagram used for LEDs

The components used were: $1 \times$PP3 9*V* battery, $1 \times$Battery connector, $2 \times 150\Omega$ Resistors (Brown, Green, Black, Black), 4×5*mm* Superbright *Red* Kingbright LEDs L-53SRC-DW and $6 \times$Lengths of low ohmic electrical wire (measured in order to adequately position the LEDs to the required location on the model aircraft).

Appendix 5: Piper cub model A/C dimensions

The model aircraft used in the Machine Vision trials is a scale model of the Piper cub J3 aircraft. Measurements of the major aircraft parts were taken for later use in the pose software. A summary of these are presented below, with additional diagrams of the model.

Wing (*m*)	
b_{wing}, wing span	1.520
s_{wing}, wing semi span	0.760
chord wing	0.235
dist. centreline to aileron	0.295
aileron length	0.370
dist.aileron to outboard wing tip	0.105

Distance Wing - tail plane & fin (*m*)	
dist. LE wing to LE tail plane	0.540
dist. TE wing to LE tail plane	0.300
dist. TE wing to LE fin	0.290

Tail plane (Horizontal tail surface) (*m*)	
b_{tail}, span tail plane	0.430
semi span tail plane	0.215
chord tail plane	0.150
chord elevator	0.085

Additonal mesurements (*m*)	
Nose to LE wing	0.250
Nose to TE wing	0.485
Nose to LE horizontal tail	0.740
Nose to TE horizontal tail	0.900
Nose to Fin	0.920

Fin (Vertical tail surface) (*m*)	
height above tail plane	0.180
height below tail plane	0.020
dist. aft of TE of tail plane	0.035

Tables A5.1 to A5.5: As measured by the author.

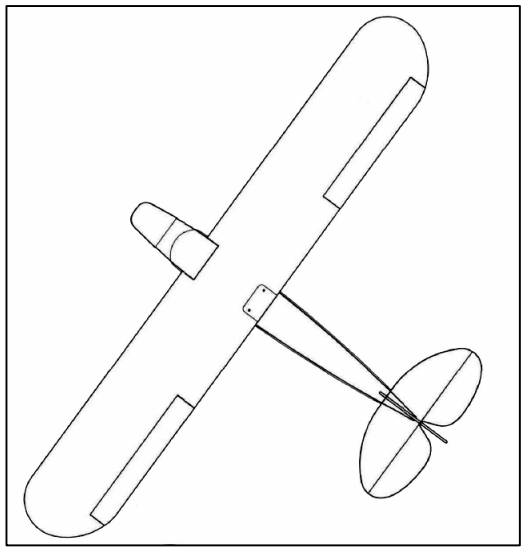

Figure A5.1[u]: Plan view of Piper cub model A/C.

[u] p47, http://manuals.hobbico.com/gpm/gpma0158-manual.pdf

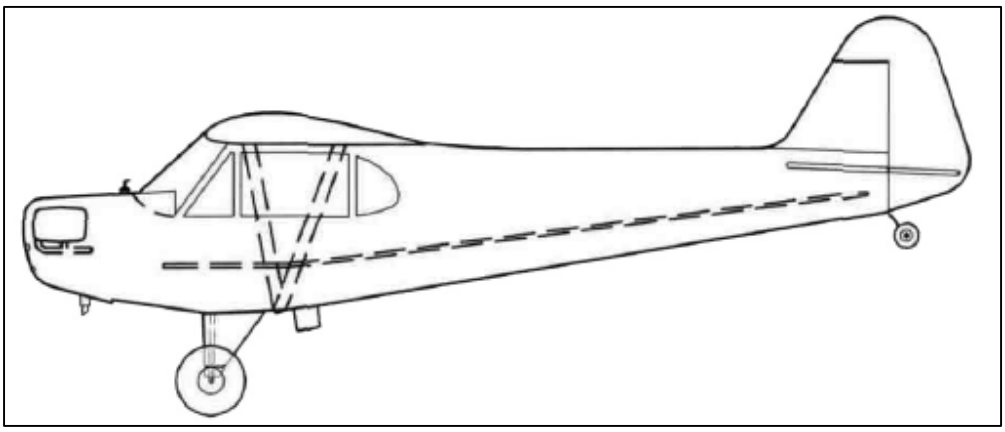

Figure A5.2[v]: Side view of Piper cub model A/C.

Figures A5.3 and A5.4: Illustrating the models' wingtips and fin

Distance CG to LEDs (*m*, in NED axis)			
LED	**X**	**Y**	**Z**
A, top of fin	-0.67	0.00	-0.13
B, Stbd wing tip	-0.12	0.76	0.00
C, bottom of fin	-0.67	0.00	0.07
D, port wing tip	-0.12	-0.76	0.00

n.b. *CG* taken to lie ontop of wing centre spar on a/c centre line.

Table A5.6: Positions of the LEDS, relating to Piper cub model's c.g.

The locations of the LEDs for the pose estimation were restricted by the model's size. Therefore, in order to facilitate identifying the individual LEDs their locations were chosen to lie on the extreme parts on the model. This point was important in being able to perform accurate pose estimations using the image processing software.

[v] p47, http://manuals.hobbico.com/gpm/gpma0158-manual.pdf

Appendix 6: Future work

The following images were captured by the *Eyecam*© outdoors:

Figure A6.1: *Pierre_machine_vision_test_pipercub_06_august_0009*

Figure A6.2: *Pierre_machine_vision_test_pipercub_06_august_0019*

Appendix 7: Appendix CD

The following text acts as a contents page for the data included on the Machine vision appendix CD.

****

MSc Thesis: Machine vision and autonomous navigation (Thesis title)
Submission: September 2008

This CD contains 13 folders of supporting information relating to the practical element of the thesis.

****

The following folders are listed in chronological order

***

These folders contain the images from experiment 1, used to calibrate the Eyecams:

1) 5 July Calib Test1 Yellow dot (Hobbs calib)
2) 8 July Calib Test1 Green dot (Hobbs calib)

****

These folders contain the images used for experiment 2, used to determine the RGB capability of the Eyecams:

3) July 5 Calib - Test 2 Yellow dot (LEDS)
4) July 8 Calib - Test 2 Green dot (LEDS)
5) July 8 Photos - Test 2 OLYMPUS Camera (LEDS)
6) July 8 Yellow dot camera (Principle) red folders
7) July 8 Green dot camera red folders

****

These folders contain the images used for experiment 3, used to determine the Eyecam cameras pose relative to the piper cub model plane:

8) July 14 Aircraft test Yellow Dot pics (Principle)
9) July 14 Aircraft test Yellow Dot pics (Principle)
10) July 17 Aircraft test Yellow Dot pics (Principle)

****

This folder contains the data following post processing of experiments 1 and 2:

11) Image data from post processing (Exel spreadsheets)

****

These folders are required for the AVI1 and Mfitvid programs to work (these should be saved on the C:\ drive) see appendix E3.3 in the thesis for guidlines on operating:

12) videowork
13) video

N.B. folder 12) contains all the files for the AVI1 program:

XX July Cal data => folders contain the data of each image for AVI1 to run
XX July Mfitvid data => folders contain the data output from the AVI1 program (require only dat files to run Mfitvid)

folder 13) contains all the files required for the Mfitvid program:

XX July Dat files => folders contain the necessary files to run Mfitvid
XX July Results => folders contain the pose output files from Mfitvid
17 July covariance results => contains the covariance results for selected images

Finally all requests for the AVI1 and Mfitvid .exe files should be addressed to:

Dr S.E Hobbs: S.E.Hobbs@cranfield.ac.uk

***

****

Pierre-Daniel Jameson Msc Aerospace Dynamics August 2008

****

Appendix 8: Example curvature, covariance and correlation matrices for:

Pierre_machine_vision_test_pipercub_17_july_0013

Curvature and covariance matrices from modelfit, v 1.10
Calculated on Tue Aug 05 18:38:26 2008
Source file is spycamimage17JLY13dat.txt
SVD routines have deleted 0 (fit), 0 (error bounds) eigenvectors

Curvature matrix (alpha):

6 6

1.077940e+002	-1.273632e+002	-6.078913e+002	-9.153774e+002	-4.009583e+003	-1.719997e+003
-1.273632e+002	6.989261e+003	3.295221e+001	4.972047e+004	2.302065e+003	-6.400314e+002
-6.078913e+002	3.295221e+001	5.793128e+003	2.700548e+002	3.796974e+004	1.654776e+004
-9.153774e+002	4.972047e+004	2.700548e+002	3.552301e+005	1.645991e+004	-3.960487e+003
-4.009583e+003	2.302065e+003	3.796974e+004	1.645991e+004	2.507400e+005	1.080350e+005
-1.719997e+003	-6.400314e+002	1.654776e+004	-3.960487e+003	1.080350e+005	4.903418e+004

Covariance matrix (covar):

6 6

2.400387e-002	-2.230673e-004	4.315779e-003	9.923819e-005	-2.290034e-004	-1.048099e-004
-2.230673e-004	3.750062e-002	-2.502999e-004	-5.204025e-003	-6.146947e-004	1.500134e-003
4.315779e-003	-2.502999e-004	4.458571e-002	2.461953e-004	-5.639154e-003	-2.453998e-003
9.923819e-005	-5.204025e-003	2.461953e-004	7.265499e-004	5.267563e-005	-2.049050e-004
-2.290034e-004	-6.146947e-004	-5.639154e-003	5.267563e-005	8.200835e-004	8.441056e-005
-1.048099e-004	1.500134e-003	-2.453998e-003	-2.049050e-004	8.441056e-005	6.619306e-004

vector of covariance eigenvalues

0.046283	0.023172	0.038283	0.000555	0.000003	0.000003

Correlation matrix (corr):

6 6

1.000000e+000	-7.434915e-003	1.319231e-001	2.376323e-002	-5.161456e-002	-2.629393e-002
-7.434915e-003	1.000000e+000	-6.121298e-003	-9.969822e-001	-1.108437e-001	3.010958e-001
1.319231e-001	-6.121298e-003	1.000000e+000	4.325628e-002	-9.325822e-001	-4.517209e-001
2.376323e-002	-9.969822e-001	4.325628e-002	9.999999e-001	6.824141e-002	-2.954701e-001
-5.161456e-002	-1.108437e-001	-9.325822e-001	6.824141e-002	1.000000e+000	1.145675e-001
-2.629393e-002	3.010958e-001	-4.517209e-001	-2.954701e-001	1.145675e-001	1.000000e+000

Insert A1: Example curvature, covariance and correlation matrices for image 13, taken on 17th of July

Appendix Experiment 1: Camera Calibration: 05/07/08 – 08/07/08

1.1) Introduction:

The purpose of this experiment is to provide an estimation of the amount of distortion present for two *Eyecam*© CMOS micro-cameras (ALM-2451G/4RX) to a 1st order degree. Using readily available apparatus a simple experiment was devised and initial results for the lens' central distortion was determined.

1.2) Theory:

An image is captured by the following process:

1) the light reflected by the image enters the camera's aperture.
2) the lens then enables this light to be focused onto the CMOS chip.
3) the CMOS chip registers the image in numerical format.

The lens is the key component as it permits an image mapping from the 3D-world to the 2D pixel array output of the CMOS chip. Therefore, any manufacturing imperfections or surface aberrations will lead to inaccurate results.

In order to quantify the trueness of the "real" image to pixel mapping the discrepancies between known points such as on a calibration grid pattern can be measured. Using a chequered board (see appendix T1) with known square size ($26mm \times 26mm$) the camera's image mapping can be evaluated as follows:

let, X_{sq} = Square length *x* (*m*), Y_{sq} = Square length *y* (*m*), X_{pix} = Square length *x* (*pixels*) Y_{pix} = Square length *y* (*pixels*) and *L* = Length camera to calibration pattern (*m*).

in X: $\frac{X_{sq}}{X_{pix}} \Big/ L$ (mrads) … (eqn E1.1) in Y: $\frac{Y_{sq}}{Y_{pix}} \Big/ L$ (mrads) … (eqn E2.1)

1.3) Apparatus:

1×Ruler (±0.0005m), 1×Tape measure (±0.002m), 1×retort stand with vice and clamp, 1×Chequered calibration pattern, 1×*Eyecam*©, 1×receiver, 1×analogue to digital converter and 1×Laptop with image capture and processing software installed.

1.4) Method:

The machine vision configuration is shown in diagrams E1.1 to E4.1 below, the camera transfers the video images via a Radio Frequency (RF) link with the receiver box, see antenna in diagram E1.1.

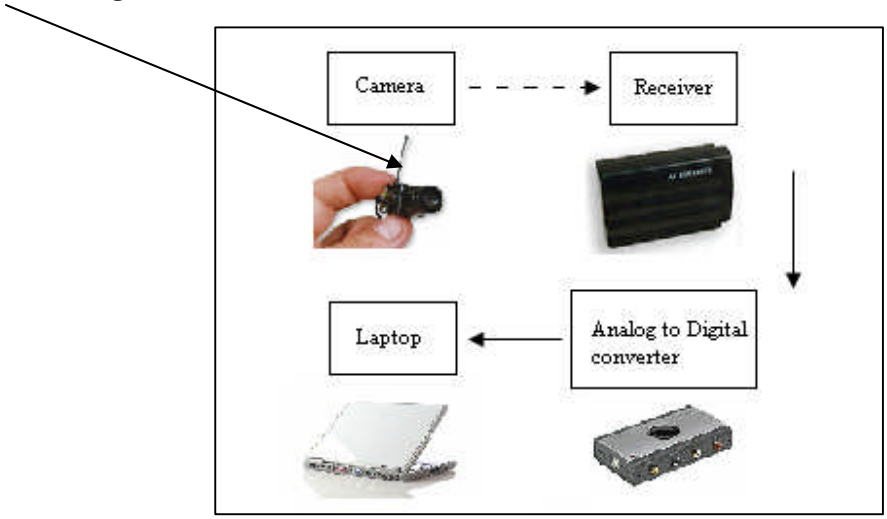

Diagram E1.1: Circuit diagram

Diagram E2.1: Camera and receiver

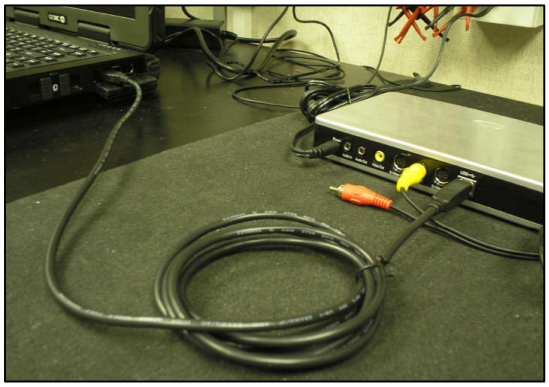

Diagram E3.1: A/D converter to laptop

Connections between the camera receiver and the Analogue to Digital (A/D) converter are made then the digital link to the laptop is completed via a USB connection (diagram E3.1).

It is important to ensure that the correct voltage power adapters are connected to the camera (4.5V) and receiver (12V) respectively, in order to prevent any damage to the camera. Once the machine vision apparatus has been correctly connected the calibration image can be set up.

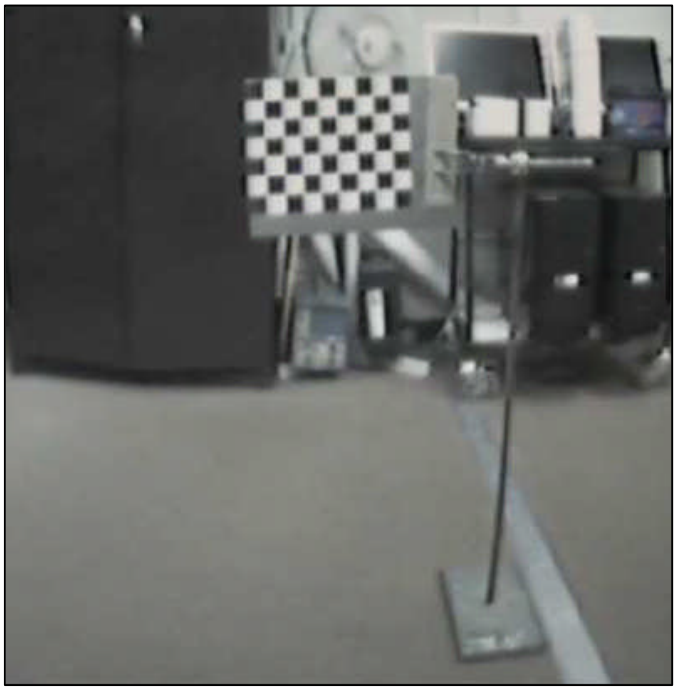

Using the vice and clamp the calibration chequerboard (see appendix T1.1) is held up on the retort stand at a measured distance from the camera lens as in diagram E4.1.

Having set up the apparatus the video data is captured using the *Capwizz*© software which is supplied with the A/D converter.

Diagram E4.1: Calibration pattern set up (as seen with *Eyecam*©).

Following the GUI prompts (see appendix T1.2) from the *Capwizz*© program the video imagery can be recorded on the computer. Once the desired video has been captured a still image can be taken using the *Windows Movie Maker*© (see Appendix T1.3) software to extract an image from the video. A suitable image for the 1st order calibration is shown beside (diagram E5.1).

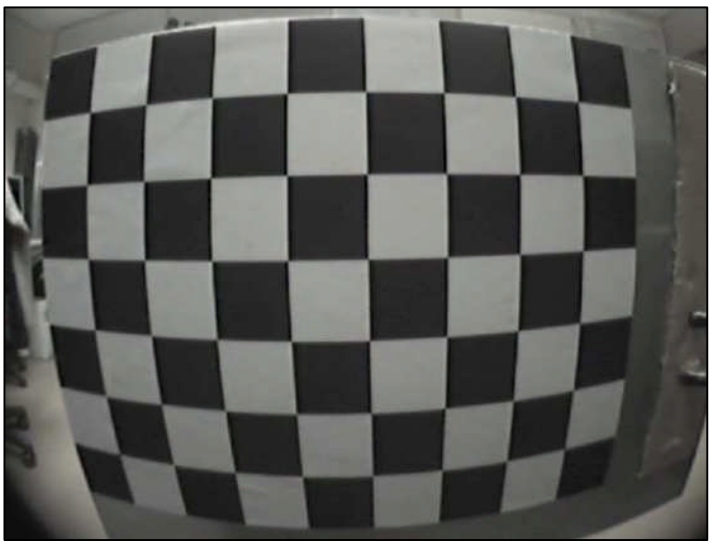

Diagram E5.1: Calibration Image (taken from *Eyecam*©)

From the above image the necessary pixel lengths can be determined using suitable image processing software such as GIMP and first order estimations for camera distortion can be calculated.

1.5) Results:

Using the squares closest to the centre of the image (see diagram E6.1 below) the following calculations were performed for both cameras. Note that the square lengths in pixels were measured for the closest complete square nearest the centre of the lens. For example referring to diagram E6.1, taking the centre of the lens to be represented by the black dot, the nearest complete squares are between the two white dots in both the X and Y directions.

Yellow dot camera:

Using the images named: **Pierre_machine_vision_test_5_july_0003** and **Pierre_machine_vision_test_5_july_0002**. Image 0002 and 0003 were taken at 1.15*m* and 0.15*m* away from the camera central lens respectively for the **Yellow dot camera** (this denotes the principal camera used throughout the research It has an a RF of 2472MHz).

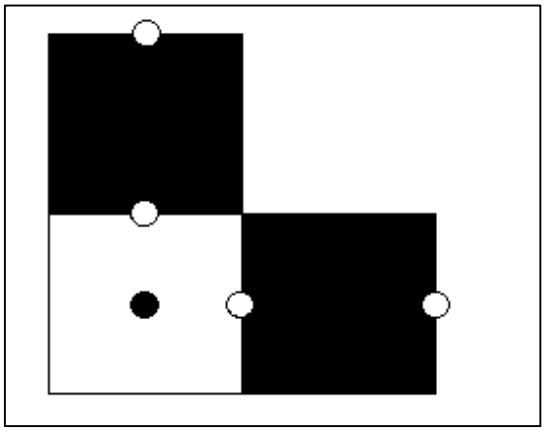

Image 0002

In *X*: $\frac{0.026}{10} \Big/ 1.15 = \underline{2.2609}$ *m*rad

In *Y*: $\frac{0.026}{12} \Big/ 1.15 = \underline{1.8841}$ *m*rad

Image 0003

In *X*: $\frac{0.026}{78} \Big/ 0.15 = \underline{2.3423}$ *m*rad

In *Y*: $\frac{0.026}{74} \Big/ 0.15 = \underline{2.2222}$ *m*rad

Diagram E6.1: Sample grid near image centre.

Green dot camera:

Using the images named: **green_dot_camera_calib_close_up** and **green_dot_camera_calib_far_away**. The **Green dot camera** is the spare/secondary camera and has an RF of 2472MHz. The same procedure for calculating a first order model was used and the following values were established:

Far_away:

In *X*: $\frac{0.026}{24} \Big/ 0.57 = \underline{1.9006}$ *m*rad

In *Y*: $\frac{0.026}{25} \Big/ 0.57 = \underline{1.8246}$ *m*rad

Close_up:

In *X*: $\frac{0.026}{76} \Big/ 0.16 = \underline{2.1382}$ *m*rad

In *Y*: $\frac{0.026}{84} \Big/ 0.16 = \underline{1.9345}$ *m*rad

Summarising the close up calibration results:

Where the test image fills the majority of the field of view, the first order camera calibration is determined to be:

Camera:	**X**	**Y**
Yellow dot (principle)	2.3423 *m*rad	2.2222 *m*rad
Green dot (secondary)	2.1382 *m*rad	1.9345 *m*rad

Table E1.1: Camera calibration results

Uncertainty in measurements (For **Yellow dot** camera):

The measured quantities have the following ranges of precision: Tape measure = $\pm 0.002m$, Ruler = $\pm 0.0005m$, Pixel in $X = \pm 2$ pixel and $Y = \pm 2$ pixel

For the 15*cm* trial the following (1) Max error and (2) Min error are calculated with:

(1) Measurements: $L = 0.152m$, $X_{sq} = Y_{sq} = 0.0265m$, $X_{pix} = 76$ pixels and $Y_{pix} = 80$ pixels

(2) Measurements: $L = 0.148m$, $X_{sq} = Y_{sq} = 0.0255m$, $X_{pix} = 72$ pixels and $Y_{pix} = 76$ pixels

Therefore 1) Max error is determined to be:

In *X*: $\frac{0.0265}{76} \Big/ 0.152 = \underline{2.2940}$ *m*rad

In *Y*: $\frac{0.0265}{80} \Big/ 0.152 = \underline{2.1793}$ *m*rad

And the 2) Min error is determined to be:

In *X*: $\frac{0.0255}{72} \Big/ 0.148 = \underline{2.3930}$ *m*rad

In *Y*: $\frac{0.0255}{76} \Big/ 0.148 = \underline{2.2671}$ *m*rad

These enable a percentage error to be calculated in the X and Y axis:

Value	X	Y
Min	2.062 %	2.165 %
Max	1.9305 %	2.021 %

Table E1.2: Percentage error values for X and Y.

Following these results the camera calibration file, **imagecal_spycam** was created with the calibration data (for the **Yellow dot** camera) as required for the pose position software used in *Experiment 3*:

```
# imagecal_spycam.txt
# Contains image calibration coefficients for the Spycam.
# File contains one data line summarising the contents (# of cameras, # of coefficients, etc.)
# then a line giving the image origin for each camera (origin_col, origin_row),
# and then the lines giving coefficients of the polynomials used to model distortions for
# each camera (inclination coefficients, then azimuth; excluding a[0] which is assumed to be 0).
# All comment lines are at the head of the file and start with '#', data lines start with a white
# space character.
#
# S.E. Hobbs, 11:06, 17 Jul 2008   Modified PDJ, 16:00, 05 Aug 2008
        2       10
                383.5           287.5           383.5           287.5
                0.0             2.2E-3          -0.0            2.2E-3
                2.3E-3          0.0             2.3E-3          0.0
                0.0             0.0             0.0             0.0
                0.0             0.0             0.0             0.0
                0.0             0.0             0.0             0.0
                0.0             0.0             0.0             0.0
                0.0             0.0             0.0             0.0
                0.0             0.0             0.0             0.0
                0.0             0.0             0.0             0.0
```

Insert E1.1: Camera calibration results, as required for Experiment 3.

This file enables the first order distortion for the **Yellow dot** camera to be accounted for, in the correct format required for Experiment 3 (when the pose estimation program **Mfitvid** is run).

1.6) Discussion:

The above experimental procedure describes the process to determine a basic first order relationship for the cameras' distortion. An important point to note during the image capturing process is the choice of backing material for the calibration grid pattern. A flat rigid backing material is required, such as sheet steel which is used in this experiment. This is essential in order to ensure that the calibration grid remains flat and perpendicular to the test camera.

The first order camera calibration has been determined to be approximately 2*mrad* (table E1.1). These results have been written in the required form for the **Mfitvid** program (see insert 1). The estimated errors in X and Y for the camera calibration were determined to be approximately 2% (table E1.2). However, due to the shape of the cameras lens these values would be expected to be higher in accordance with the "fish-eye" / skew effect associated with such a spherically shaped lens. The calibration would thus be expected to hold true for the central region in each image. Therefore, care must be taken when capturing further images in order to keep the object of interest within the centre of the cameras' field of view.

A final note regarding the experiment set-up should be mentioned. Before launching the *Capwizz*© software all cables should be correctly connected and the power to each device turned on, these should not be removed or turned off during the image capturing. Failure to adhere to these precautions may cause problems when attempting to preview and capture any image with the software, thus requiring a re-launch of the Capwizz© program.

1.7) Conclusion:

This simple experiment has enabled a first order calibration of the two *Eyecams* to be performed. The values for the **Yellow dot** camera have been written in the necessary file format (**Imagecal_spycam**) for the **AVI1** converter. Thus the **Mfitvid** program can now also be used to determine the position/pose of the camera relative to key points within an image as required for Experiment 3.

Appendix: T1.1 Chequerboard

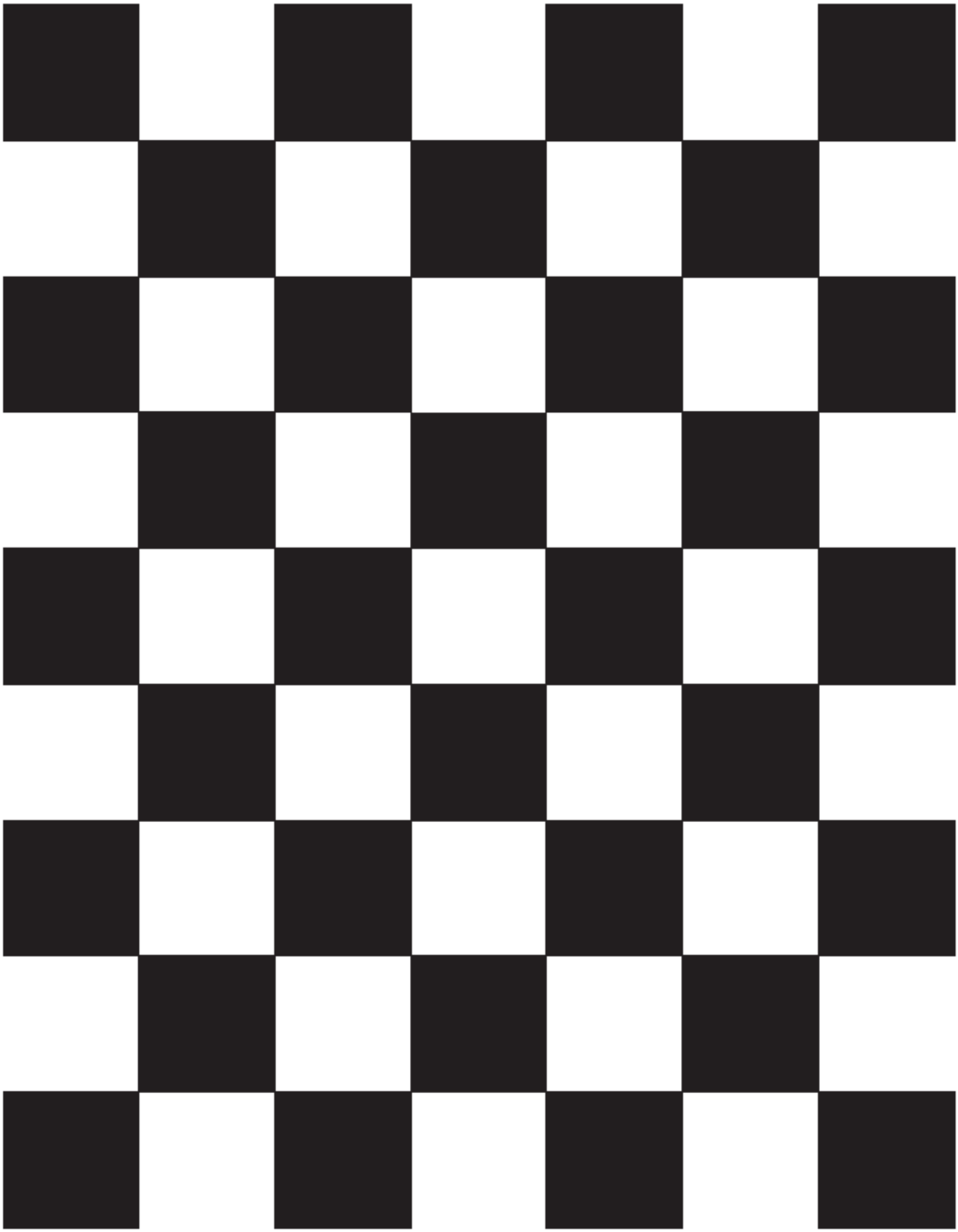

Appendix T1.2: Guidelines for using *Capwizz*© program

1) Having set up the apparatus as illustrated in diagram E1.1 ensuring that all connection leads are plugged in the computer can be switched on.

2) Double-click on the *Capwizz*© icon on the desktop to open up the analogue to digital converter configuration panel.

3) When prompted to select a video system select: **United Kingdom, PAL**.
This will enable the correct colour format to be used for the video images received from the *Eyecam*. Then click on **Next**.

4) The following box enables the user to specify the connections used on the analogue to digital converter. Using the leads provided with the *Eyecam* and analogue to digital converter select: **RCA**, both times for 1. video capture/record and 2. send back.

5) The next box enables the user to specify a name for the video file. A suitable file name should be chosen with necessary information in mind for later referral, such as:
username*_MACHINE_VISION_*testnumber_camera_month_date replacing the italics as appropriate (N.B. use Yellow_dot or Green_dot to specify the *camera* used). The files location can be specified using the save files address bar or by clicking on **Browse**.

6) The final box requires the user to specify which video format the captured files should be recorded in. Selecting the **DVD/MPEG-2** format provides the best quality image available for the post video capture processing. Following this, click-on **Next**, followed by **Finish** and this will start the camera plug in enabling video capture**.**

7) Following the final configuration box, a preview window should open, click-on **Preview** and the real time video images from the camera should be displayed within the window.

8) To capture a video file use the video controls located on the bottom left of the preview window. Click on the **Red Dot** to record and click again on the **Black Square** to stop recording. **N.B** each time a video is captured (due to a Red Dot - Black Dot sequence) the file name is used and a four digit number assigned to the end in sequential order starting from 0000.
i.e ***username*_MACHINE_VISION_*testnumber_camera_month_date*-XXXX**

Appendix T1.3: **Guidelines for using *Windows Movie Maker* ©**

In order to capture a still image from the video files created with *Capwizz* ©.

1) Open the *Windows Movie Maker* © program by clicking on the **Windows Start** bar and then by selecting *Windows Movie Maker* © from the **All programs** menu.

2) Once the program window is opened select the movie file for image capture by clicking on **File**, followed by **Import into Collections**. Specify the folder containing the file in the address bar and select the required file name:

i.e. **Pierre_machine_vision_*testnumber__camera_month_date*-XXXX**

and click **Import**, making sure to select *all media files* from the **File of type** drop down menu.

3) The chosen file should be imported into the **Collection Window**. It can be selected for previewing in the **Viewing Window** by clicking on it. Adjust the **Viewing Window** to a suitable size in order to preview using the mouse curser. Then by operating the play-back buttons in the viewing window, clicking on the **Play arrow** and then *Pause* the movie at the desired frame by clicking on the **Play arrow** again, which pauses the on screen video playback.

4) Subsequently, a still image is captured from the **Viewing Window** by either clicking on **Tools**, followed by **Take Picture from Preview** *or* clicking on the *Camera icon* on the video play-back window controls.

5) When the **Save Picture As** window opens, specify the folder to save the image to using the **Save in:** address bar. It is useful to specify the image file name from that automatically generated to:

Pierre_machine_vision_*testnumber_camera_month_date*_XXXX (with the italics replaced accordingly) finally specify the file type to be saved as **.Jpg** in the **Save as type** address bar and then click on **Save**. This process should be repeated for the required number of images.

Appendix Experiment 2: RGB estimation 07/07/08 – 11/07/08

2.1) Introduction:

The aim of this experiment was to determine the ability of the two different *Eyecams* (**Yellow dot** and **Green dot**) to detect and isolate the three main colours in a given image. In order to enable a better comparison of the results, an Olympus Digital Camera was also used to capture images. Two LED's similar to those that would be used in the main pose estimation experiment provided the target image with a "passive" (i.e. without an information signal transfer, such as radio waves) colour source to be analysed.

2.2) Theory:

Using illuminated LEDS on a target enables a *passive* beam of light to be projected. This stands out from the ambient background and can be easily captured by a digital camera's CCD which captures the image and breaks down the colour into three colour channels consisting of ***Red***, ***Green*** and ***Blue*** (RGB). Thus by selecting an area in the image and using a post image capture processing tool, such as *GIMP 2©*, a colour histogram showing the quantity of colour saturation for each channel can be obtained.

The saturation values for each channel enable a specific shade of colour to be defined. This is an important point in being able to clearly identify the coloured target in a scene. It should be noted that the values for each of the three channels are free to vary between 0 and 225, with 225 (the saturation/maximum value) on all three channels corresponding to pure white light.

2.3) Apparatus:

$1\times$Tape measure ($\pm$0.002m), $1\times$retort stand with vice and clamp, $1\times$A4 red folder, $2\times$LEDs (see appendix T2.2) with power source, $1\times$Olympus camera (c-180), $2\times$*Eyecams*, $1\times$receiver, $1\times$analogue to digital converter and $1\times$Laptop with image capture and processing software installed.

2.4) Method:

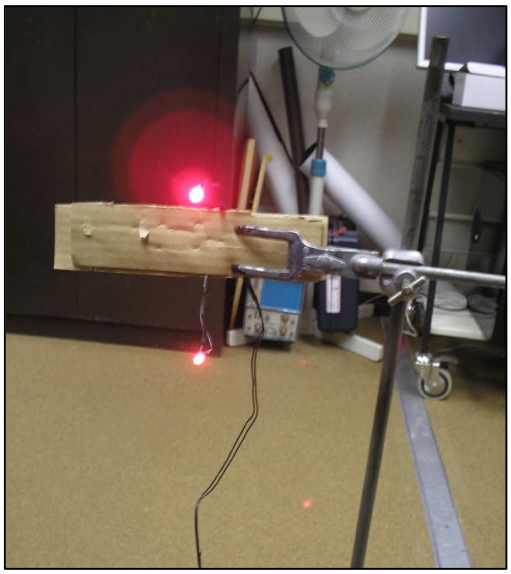

Diagram E2.1: The LED set up.

The RGB test is performed using the above apparatus. The LEDs were 0.1*m* apart (see diagram E2.1) and can be positioned at varying distances away from the camera by moving the stand.

The camera set up is as per Experiment 1, with the **Yellow dot camera** used to capture the images.

The camera image is transferred via RF to the receiver which outputs its signal to the analogue to digital converter which in turn is connected to the laptop via USB cable (see Diagram E1.1 in Experiment 1).

Images from each of the *Eyecams*, (**Yellow Dot** and **Green Dot**) were recorded for both the top and bottom LEDs. Images of the LEDS at distances of 0.15*m*, 0.50*m*, 1.15*m* and 2.30*m* were taken together with a sample image for each camera taken in darkness for a comparison purposes.

The same LED experiments above were repeated with the Olympus camera to provide an additional comparison. Finally, in order to evaluate the cameras' sensitivity to a non-emitting source of red, an additional experiment, capturing an image of a Red Folder, was performed for all three cameras.

Once all the images for the 4 experiments had been collected the RGB colour captured for both LEDs could be determined for the complete set of images. A detailed description of this procedure can be found in appendix T2.1.

Machine Vision Image RGB results from post processing of 5th of July experiments Yellow dot Camera (N0.1)

		Red			Green			Blue			Average Σ RGB		
Name of Image	LED	Mean	σ	Median	Mean	σ	Median	Mean	σ	Median	Mean	σ	Median
Pierre_machine_vision_test2_5_July_0000	Top	231.4	1.1	232.0	225.1	0.9	225.0	220.3	1.7	221.0	225.6	1.2	226.0
Taken @ 15cm from camera	Bottom	237.8	2.2	238.0	230.7	1.3	231.0	227.5	1.4	227.0	232.0	1.6	232.0
	Av.LED =>	***234.6***	***1.7***	***235.0***	***227.9***	***1.1***	***228.0***	***223.9***	***1.6***	***224.0***	***228.8***	***1.4***	***229.0***
Pierre_machine_vision_test2_5_July_0001	Top	222.8	1.9	222.0	216.5	3.0	217.0	211.5	1.9	212.0	216.9	2.3	217.0
Taken @ 53cm from camera	Bottom	232.7	2.1	233.0	223.5	3.4	224.0	221.3	2.2	221.0	225.8	2.6	226.0
	Av.LED =>	***227.8***	***2.0***	***227.5***	***220.0***	***3.2***	***220.5***	***216.4***	***2.1***	***216.5***	***218.2***	***3.7***	***221.5***
Pierre_machine_vision_test2_5_July_0002	Top	220.9	1.6	221.0	215.5	2.1	216.0	210.3	1.6	210.0	215.6	1.8	215.7
Taken @ 115cm from camera	Bottom	224.5	2.8	235.0	228.9	3.3	229.0	226.9	1.7	227.0	226.8	2.6	230.3
	Av.LED =>	***222.7***	***2.2***	***228.0***	***222.2***	***2.7***	***222.5***	***218.6***	***1.7***	***218.5***	***221.2***	***2.2***	***223.0***
Pierre_machine_vision_test2_5_July_0003	Top	235.2	2.8	235.0	228.9	3.3	229.0	226.9	1.7	227.0	230.3	2.6	230.3
Taken @ 115cm from camera (in Darkness)	Bottom	235.6	1.9	236.0	226.6	2.5	227.0	226.4	2.0	227.0	229.5	2.1	230.0
	Av.LED =>	***235.4***	***2.4***	***235.5***	***227.8***	***2.9***	***228.0***	***226.7***	***1.9***	***227.0***	***229.9***	***2.4***	***230.2***
Pierre_machine_vision_test2_5_July_0004	Top	217.8	2.0	217.0	212.9	2.7	213.0	207.4	1.6	207.4	212.7	2.1	212.5
Taken @ 230cm from camera	Bottom	220.4	2.6	220.0	213.5	2.6	213.0	208.6	2.5	208.0	214.2	2.6	213.7
	Av.LED =>	***219.1***	***2.3***	***218.5***	***213.2***	***2.7***	***213.0***	***208.0***	***2.1***	***207.7***	***213.4***	***2.3***	***213.1***
Pierre_machine_vision_test2_5_July_0005	Top	234.7	2.1	235.0	226.9	2.1	227.0	223.7	2.5	224.0	228.4	2.2	228.7
Taken @ 230cm from camera (in Darkness)	Bottom	231.9	6.3	234.0	221.2	6.6	224.0	221.6	6.2	223.0	224.9	6.4	227.0
	Av.LED =>	***233.3***	***4.2***	***234.5***	***224.05***	***4.35***	***225.5***	***222.7***	***4.35***	***223.5***	**226.7**	**4.3**	**227.8**

	Red			Green			Blue				Average Σ RGB		
Average of total Ave values for both LEDS	Mean	σ	Median	Mean	σ	Median	Mean	σ	Median		Mean	σ	Median
for the 6 positions =	228.8	2.5	229.8	222.5	2.8	222.9	219.4	2.3	219.5	Σ Ave. =	223.0	2.7	224.1

i.e average of average value from LEDs for the 6 different LED positions

σ = Standard deviation
Σ = Total

Table E2.1: Yellow dot camera RGB results.

Machine Vision Image RGB results from post processing of 8th of July experiments GREEN DOT CAMERA (No. 2)

		Red			Green			Blue			Average Σ RGB		
Name of Image	LED	Mean	σ	Median	Mean	σ	Median	Mean	σ	Median	Mean	σ	Median
Pierre_machine_vision_test2_8_july_0000	Top	208.7	27.8	220.0	206.9	29.8	220.0	205.8	28.6	218.0	207.1	28.7	219.3
Taken @ 15cm from camera	Bottom	207.0	10.9	213.0	201.0	18.2	211.0	201.7	15.8	210.0	203.2	15.0	211.3
	Av.LED =>	***207.9***	***19.4***	***216.5***	***204.0***	***24.0***	***215.5***	***203.8***	***22.2***	***214.0***	***205.2***	***21.9***	***215.3***
Pierre_machine_vision_test2_8_july_0001	Top	207.4	4.7	208.0	207.1	5.0	208.0	205.1	4.9	206.0	206.5	4.9	207.3
Taken @ 30cm from camera	Bottom	204.9	25.2	215.0	201.3	30.9	214.0	199.7	29.5	212.0	202.0	28.5	213.7
	Av.LED =>	***206.2***	***15.0***	***211.5***	***204.2***	***18.0***	***211.0***	***202.4***	***17.2***	***209.0***	***220.8***	***31.0***	***210.5***
Pierre_machine_vision_test2_8_July_0002	Top	189.9	33.8	206.0	189.7	34.1	206.0	187.6	34.5	204.0	189.1	34.1	205.3
Taken @ 50cm from camera	Bottom	202.4	26.1	214.0	194.9	30.0	210.0	195.4	28.5	210.0	197.6	28.2	211.3
	Av.LED =>	***196.2***	***30.0***	***210.0***	***192.3***	***32.1***	***208.0***	***191.5***	***31.5***	***207.0***	***193.3***	***31.2***	***208.3***
Pierre_machine_vision_test2_8_July_0003	Top	170.9	38.9	186.0	170.2	39.9	187.0	169.2	39.5	184.0	170.1	39.4	185.7
Taken @ 1m from camera	Bottom	170.8	48.4	194.0	167.2	49.1	191.0	167.4	48.8	192.0	168.5	48.8	192.3
	Av.LED =>	***170.9***	***43.7***	***190.0***	***168.7***	***44.5***	***189.0***	***168.3***	***44.2***	***188.0***	***169.3***	***44.1***	***189.0***
Pierre_machine_vision_test2_8_July_0004	Top	191.2	27.3	202.0	190.8	27.2	201.0	191.0	27.2	202.0	191.0	27.2	201.7
Taken @ 230cm from camera	Bottom	202.5	17.5	208.0	202.6	17.5	208.0	201.5	17.2	207.0	202.2	17.4	207.7
	Av.LED =>	***196.9***	***22.4***	***205.0***	***196.7***	***22.4***	***204.5***	***196.3***	***22.2***	***204.5***	***196.6***	***22.3***	***204.7***
Pierre_machine_vision_test2_8_July_0005	Top	152.7	61.0	173.0	148.6	61.6	170.0	151.9	61.1	174.0	151.1	61.2	172.3
Taken @ 230cm from camera (in Darkness)	Bottom	202.1	24.4	211.0	198.3	24.1	207.0	200.8	24.3	210.0	200.4	24.3	209.3
	Av.LED =>	***177.4***	***42.7***	***192***	***173.45***	***42.85***	***188.5***	***176.4***	***42.7***	***192***	***175.7***	***42.8***	***190.8***

	Red			Green			Blue				Average Σ RGB		
Average of total Ave values for both LEDS	Mean	σ	Median	Mean	σ	Median	Mean	σ	Median		Mean	σ	Median
for the 6 positions =	192.5	28.8	204.2	189.9	30.6	202.8	189.8	30.0	202.4	Σ Ave. =	193.5	32.2	203.1

i.e average of average value from LEDs for the 6 different LED positions

σ = Standard deviation
Σ = Total

Table E2.2: Green dot camera RGB results.

Machine Vision Image RGB results from post processing of 8th of July experiments with OLYMPUS CAMERA

		Red			Green			Blue			Average Σ RGB		
Name of Image	**LED**	**Mean**	**σ**	**Median**	**Mean**	**σ**	**Median**	**Mean**	**σ**	**Median**	**Mean**	**σ**	**Median**
p7080092.jpg	Top	254.1	4.8	255.0	128.6	57.4	104.0	156.2	46.1	149.0	179.6	36.1	169.3
Taken @ 15cm from camera	Bottom	250.5	10.5	255.0	182.7	76.6	214.0	192.1	62.9	217.0	208.4	50.0	228.7
	Av.LED =>	***252.3***	***7.7***	***255.0***	***155.7***	***67.0***	***159.0***	***174.2***	***54.5***	***183.0***	***194.0***	***43.1***	***199.0***
p7080093.jpg	Top	230.5	28.8	244.0	80.0	63.3	53.0	106.0	60.0	85.0	138.8	50.7	127.3
Taken @ 30cm from camera	Bottom	249.7	9.7	255.0	105.7	73.1	76.0	130.7	64.3	110.0	162.0	49.0	147.0
	Av.LED =>	***240.1***	***19.3***	***249.5***	***92.9***	***68.2***	***64.5***	***118.4***	***62.2***	***97.5***	***163.4***	***74.4***	***137.2***
p7080094.jpg	Top	246.1	16.6	255.0	89.3	56.8	69.0	126.1	52.3	113.0	153.8	41.9	145.7
Taken @ 50cm from camera	Bottom	252.6	6.4	255.0	126.3	78.0	86.0	153.3	64.3	142.0	177.4	49.6	161.0
	Av.LED =>	***249.4***	***11.5***	***255.0***	***107.8***	***67.4***	***77.5***	***139.7***	***58.3***	***127.5***	***165.6***	***45.7***	***153.3***
p7080095.jpg	Top	239.8	22.0	254.0	93.1	64.0	70.0	124.4	58.7	110.0	152.4	48.2	144.7
Taken @ 100cm from camera	Bottom	251.9	8.1	255.0	131.6	62.8	115.0	157.6	50.6	156.0	180.4	40.5	175.3
	Av.LED =>	***245.9***	***15.1***	***254.5***	***112.4***	***63.4***	***92.5***	***141.0***	***54.7***	***133.0***	***166.4***	***44.4***	***160.0***
p7080096.jpg	Top	253.0	3.1	255.0	165.8	62.5	163.0	192.4	39.4	180.0	203.7	35.0	199.3
Taken @ 115cm from camera	Bottom	249.1	11.1	253.0	151.7	67.9	128.0	172.0	56.3	164.0	190.9	45.1	181.7
	Av.LED =>	***251.1***	***7.1***	***254.0***	***158.8***	***65.2***	***145.5***	***182.2***	***47.9***	***172.0***	***197.3***	***40.1***	***190.5***

	Red			Green			Blue				Average Σ RGB		
	Mean	**σ**	**Median**	**Mean**	**σ**	**Median**	**Mean**	**σ**	**Median**		**Mean**	**σ**	**Median**
Average of total Ave values for both LEDS for the 5 positions =	247.7	12.1	253.6	125.5	66.2	107.8	151.1	55.5	142.6	Σ Ave. =	177.3	49.5	168.0

i.e average of average value from LEDs for the 6 different LED positions

σ = Standard deviation
Σ = Total

Table E2.3: Olympus camera RGB results.

Machine Vision Image RGB results from post processing of 8th of July experiments Yellow dot Camera (N0.1), Green dot camera (No.2) and Olympus camera on red folders

		Red			Green			Blue			Average Σ RGB		
Name of Image	Position	Mean	σ	Median	Mean	σ	Median	Mean	σ	Median	Mean	σ	Median
YELLOW DOT (No.1) Pierre_machine_vision_test3_8_july_0001	Close up	87.4	6.0	87.0	83.1	5.4	83.0	80.2	5.4	221.0	83.6	5.6	130.3
YELLOW DOT (No.1) Pierre_machine_vision_test3_8_july_0002	Far away	133.2	5.5	133.0	107.9	5.6	107.0	6.0	107.0	227.0	82.4	39.4	155.7
		110.3	***5.8***	***110.0***	***95.5***	***5.5***	***95.0***	***43.1***	***56.2***	***224.0***	***83.0***	***22.5***	***143.0***
GREEN DOT (No.2) Pierre_machine_vision_test_8_july_0001	Close up	101.5	9.0	103.0	97.7	9.1	99.0	95.0	8.5	96.0	98.1	8.9	99.3
GREEN DOT (No.2) Pierre_machine_vision_test_8_july_0002	Far away	148.3	1.4	148.0	118.3	1.6	118.0	116.5	1.5	116.0	127.7	1.5	127.3
		124.9	***5.2***	***125.5***	***108.0***	***5.4***	***108.5***	***105.8***	***5.0***	***106.0***	***112.9***	***5.2***	***113.3***
OLYMPUS Camera P7080098	Close up	206.5	3.3	207.0	67.0	3.5	67.0	49.4	3.8	49.0	107.6	3.5	107.7
OLYMPUS Camera P7080099	Far away	193.1	3.1	193.0	64.4	3.1	64.0	52.4	3.6	52.0	103.3	3.3	103.0
		199.8	***3.2***	***200.0***	***65.7***	***3.3***	***65.5***	***50.9***	***3.7***	***50.5***	***105.5***	***3.4***	***105.3***

	Red			Green			Blue				Average Σ RGB		
Average of total Ave values for the RED folder positions =	Mean	σ	Median	Mean	σ	Median	Mean	σ	Median		Mean	σ	Median
	145.0	4.7	145.2	89.7	4.7	89.7	66.6	21.6	126.8	Σ Ave. =	100.4	10.4	120.6

i.e average of average value for RED folder for the 6 different folder positions

n.b. Close up = 0.15m, Far away = 1m

σ = Standard deviation
Σ = Total

Table E2.4: All 3 cameras RGB results for red folders.

Diagram E2.2: *Eyecam*© image at 0.15*m*.

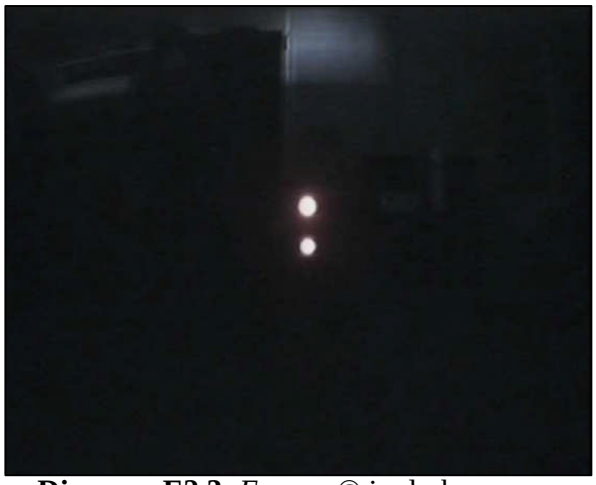

Diagram E2.3: *Eyecam*© in darkness

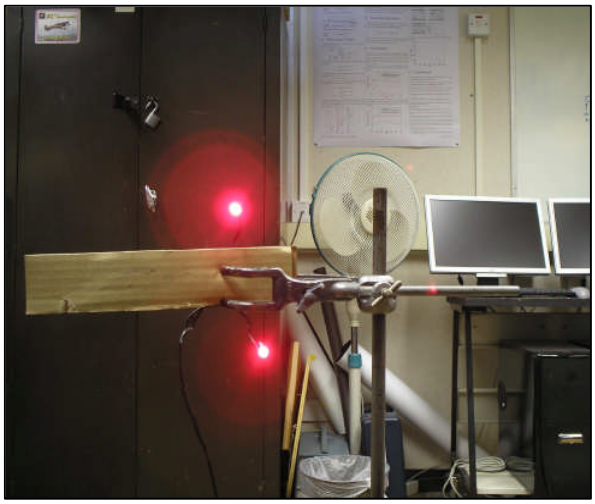

Diagram E2.4: Olympus camera LED test.

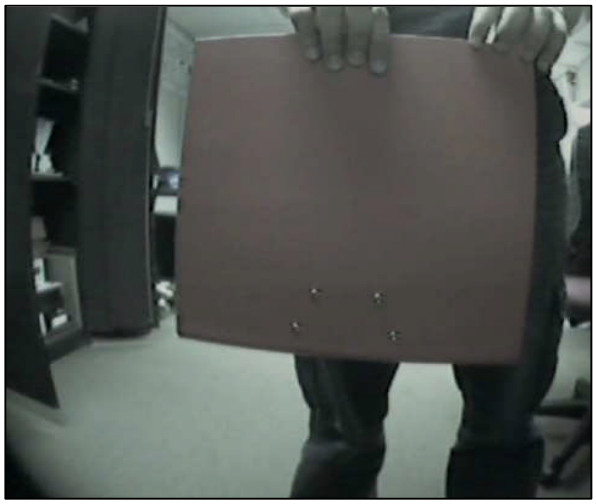

Diagram E2.5: *Eyecam*© red folder test.

2.6) Discussion:

The results shown in tables E2.1 to E2.4 enable the RGB capture for all three cameras to be compared. It can be observed for the 15*cm* case that the red LEDs for the **Yellow dot** and **Green dot** camera are seen as white (similar values across the RGB channels), however the **Olympus camera** has high *Red* saturation and marked lower saturation values for the *Green* and *Blue* channels.

Furthermore, the standard deviations for the **Green dot** camera results are much larger than that of the **Yellow dot**. However, the difference between the RGB values for the top and bottom LEDs did not vary significantly for any of the cameras.

Referring to diagrams E2.2 to E2.4, the LEDs as seen by the *Eyecam*© appear as a mixture of white with pale red, with the LEDs being easier to distinguish in darkness as would be expected. The image taken by the Olympus camera shows the top and bottom LEDs emitting their bright *Red* colour which is clearly distinct against their respective background.

The final diagram E2.5 illustrates the captured *Eyecam*© image for the passive non-emitting test for the red folder. These results in table E2.4 have much smaller values for the *Red* channel saturation in comparison to the LED tests and a slight reduction would be expected as the folder is a non-emitting source of *Red*. In addition, there is a difference between the *Close up* and *Far away* images for the *Eyecams*, with more *Red* colour being captured at the greater distance. Again the Olympus camera registers higher *Red* colour saturation than either of the *Eyecams* for this test. However, the difference between the results with distance from the target for the Olympus camera differs, with the colour saturation reducing very slightly in the *Red* and *Green* channels. A possible explanation for this difference between the Olympus and *Eyecams* could be the fact that the *Eyecams* are designed for outdoor use at height above a target.

2.7) Conclusion:

The *Eyecam*© cameras RGB capabilities have been tested and it has been shown that their ability to distinguish the difference between *Red* targets and the background scenery is less sensitive than that of a consumer Digital camera. However, the *Eyecams* provide an adequate means of detecting the difference between the LEDs and their background, thus enabling a basic colour filter process of the image to select the LEDs. Finally, it should be highlighted that the cost, weight and size of the *Eyecams* against their image capturing performance are key factors that need to be considered should an improved image sensitivity be required.

Appendix T2.1:

Directions for using GIMP 2: in order to determine the RGB values in the test images.

1) Double-click on the GIMP 2© desktop icon to launch the program to open up GIMP.

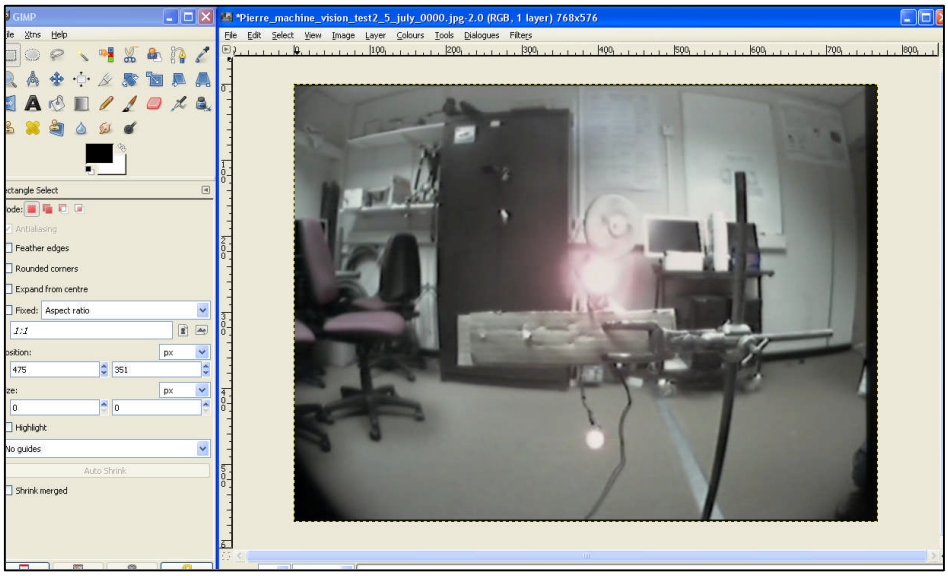

Diagram T2.1: Screen shot of the *GIMP 2*© image processing tool.

2) Select the image to be analysed by clicking on **File**, **Open**, which opens the **Open Image** window. Using the **Places** box select the image file location. Clicking on the desired file will enable a thumbnail of the image to be displayed in the **Preview** box. In the bottom right corner of the window select **All Images** option from the drop down menu and then click **Open**.

3) Once **Open** has been clicked a stand alone window with the selected image will appear in the desktop area. In order to analyse the areas in the image with the LEDs colour select the **Rectangle Select Tool** (top left icon, see diagram T2.1) in the GIMP main window. Then bringing the mouse curser over into the image window, click and drag to form a square over the region with similar colour for either the top or bottom LED (making sure to make a note of which).

4) Having selected a rectangular area in the image click on the **Colours** tab in the image window, followed by **Info** then **Histogram** to open the RGB colour histogram. Enlarge the histogram and select Red, Green and Blue in turn from the drop down menu situated in the top left of the window. From the Histogram information (diagram T2.3) the **Mean**, **Standard Deviation** and **Median** values for the colour saturation can be obtained.

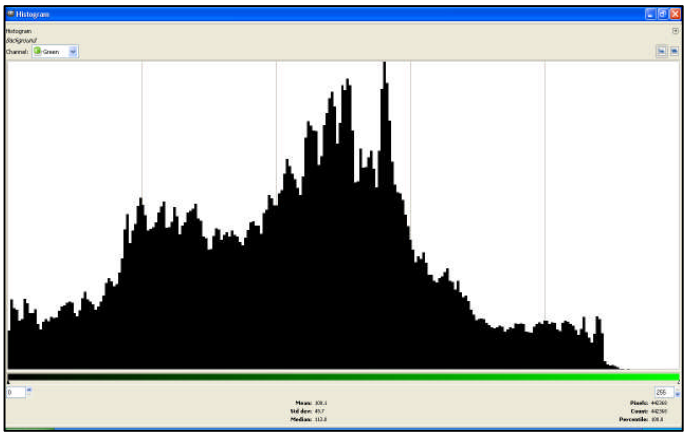

Diagram T2.3: Colour histogram.

Repeat step 3 for the other LED and return to step 2 to process further images as required.

Appendix T2.2:

Kingbright© : L-53SRC-DW 5*mm* Superbright Red LED specifications.

Part No.	Dice	Lens Type	Iv (mcd) @ 20 mA		Viewing Angle
			Min.	Max.	2θ1/2
L-53SGC	SUPER BRIGHT GREEN (GaP)	WATER CLEAR	100	300	
L-53SRC-A	SUPER BRIGHT RED (GaAlAs)	WATER CLEAR	300	400	30°
L-53SRC-B			400	500	
L-53SRC-C			500	1000	
L-53SRC-DU			1000	1300	
L-53SRC-DV			1300	1600	
L-53SRC-DW			1600	2000	
L-53SRC-E			2000	3500	
L-53SRC-F			3500	4500	

Notes:
1. θ1/2 is the angle from optical centerline where the luminous intensity is 1/2 the optical centerline value.
2. Luminous intensity/ luminous Flux: +/-15%.

Table T1.1[1]: Manufacturer's specifications for LED Luminosity and viewing angle.

Electrical / Optical Characteristics at TA=25°C

Symbol	Parameter	Device	Typ.	Max.	Units	Test Conditions
λpeak	Peak Wavelength	Super Bright Red	660		nm	IF=20mA
λD [1]	Dominant Wavelength	Super Bright Red	640		nm	IF=20mA
Δλ1/2	Spectral Line Half-width	Super Bright Red	20		nm	IF=20mA
C	Capacitance	Super Bright Red	45		pF	VF=0V;f=1MHz
VF [2]	Forward Voltage	Super Bright Red	1.85	2.5	V	IF=20mA
IR	Reverse Current	Super Bright Red		10	uA	VR = 5V

Notes:
1.Wavelength: +/-1nm.
2. Forward Voltage: +/-0.1V.

Table T1.2[1]: Manufacturer's red LED light wavelength specifications.

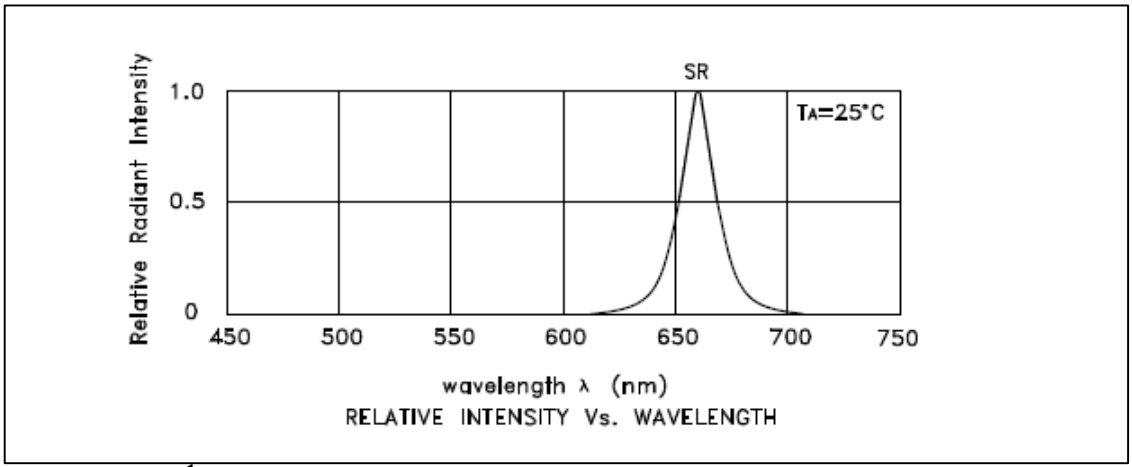

Graph T1.1[1]: Manufacturer's specifications red LED light intensity with wavelength.

[1] Kingbright L-53SRC-E, www.kingbright.com

Appendix Experiment 3:Aircraft-LED position estimation 14.07.08 – 17.07.08

3.1) Introduction:

This experiment is a follow up from experiments 1 and 2 and aims to progress towards establishing the machine vision pose estimation concept. A suitable set of images is required in order to provide a variation in all three axes: *X*, *Y* and *Z*.

Using the knowledge gained in the previous experiments, the selected **Yellow dot** camera's physical properties can be accounted for. The technique and algorithms used to determine the pose estimation, is explained in detail in "*Target position and Trajectory Measurements by Videogrammetry*", COA Report No. 208, S.E Hobbs, 2003 see reference (Hobbs, 2003).

3.2) Apparatus:

1×Tape measure (±0.002m), 1×retort stand with vice and clamp, 2×Tables, 1× Pipercub model aircraft, 1×cardboard stand, 4×Kingbright L-53SRC-DW LEDs in parallel circuit with power source (PP3 battery), 1×extension lead, 1×*Eyecam*©, 1×receiver, 1×analog to digital converter and 1×Laptop with image capture and processing software installed.

3.3) Method:

The machine vision set up remains unchanged from that used previously in experiments 1 and 2. Care was taken to select a suitable test area with a neutral / white background (see diagram E3.1 below) in order to aid the camera in distinguishing the contrast between the Piper cub model, the LEDs and any background colours.

The four LEDs in a parallel circuit were attached to the rear of both wing tips and the top and bottom of the fin, making sure that any lose wires were fastened to the model. This enabled a cross pattern of the LEDs to be observed from the rear of the aircraft model, for a forward looking observer. It is necessary to point out that the choice of wire and tape was black and yellow in order to prevent the production of any additional red in the image other

than from the LEDs. This was done so that in future work a colour filter could be implemented on the images to automatically determine each LEDs location.

The next step was to choose two tables of the same height to act as suitable work benches. Then once the Piper cub model was ready, a piece of cardboard was used to support the model in a wings level position (n.b. the Piper cub is a tail dragger aircraft) on the table in front of the white backdrop.

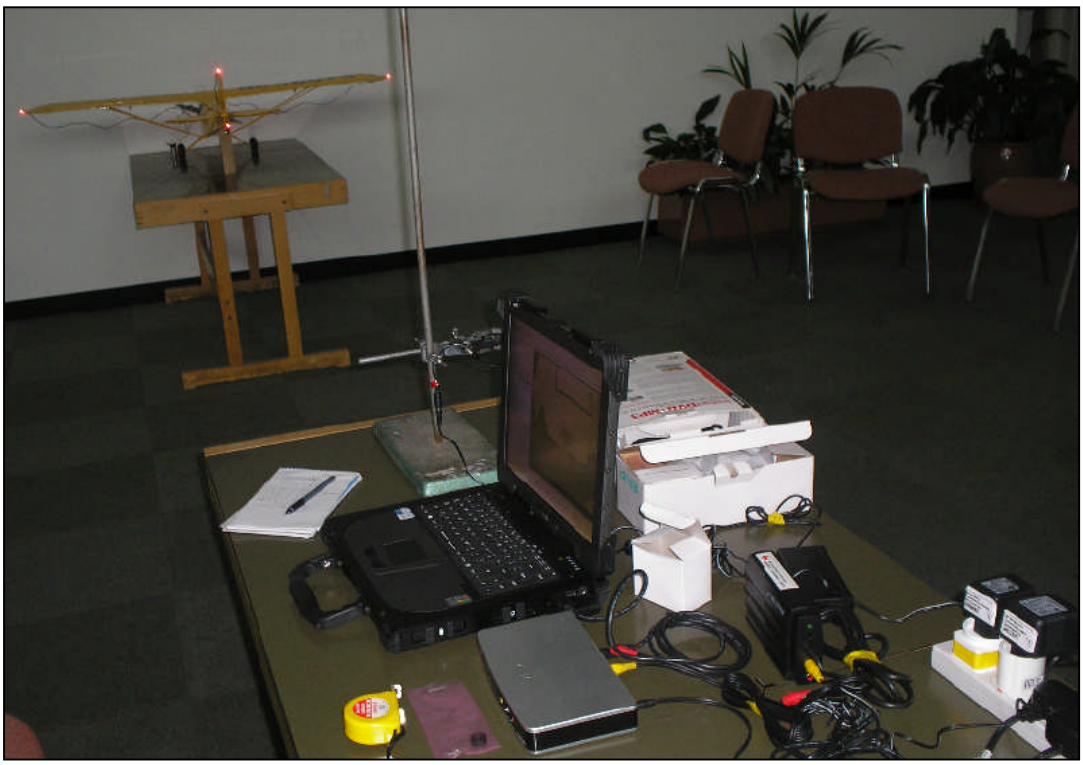

Diagram E3.1: Indoor experiment set up, showing camera aligned with model aircraft

It should be noted that the axis system used in the experiment takes displacements about and in the *North*, *East* and *Down* directions to be positive, in accordance with standard aircraft axes.

On the second table the machine vision apparatus was set up and the camera rig aligned with the centre-line of the model aircraft (setting the *Y* reading to zero). The model's centre of gravity (located on the wings centre spar) was chosen as the origin for the *NED* axes and using the measuring tape, the distance between the origin and the camera was then measured (the –*X* reading).

Setting the camera to the correct height (the $-Z$ reading) an image was captured on the laptop using the *Capwizz*© software. For each set of readings at a constant value of $-X$, the $-Z$ reading was varied 5 times between 0.1m and 0.7m before displacing the table back by approximately 1m and repeating the $-Z$ readings. A final set of readings at a constant value of $-X$ and $-Z$ were taken, varying in $-Y$ between -1.0, -1.5 and -2.0m. Following the image capturing (see appendix T1.2 and 1.3 from Experiment 1), the image processing using *GIMP* was performed (see appendix T3.1). This enabled the *row* and *column* vales for each individual LED in each of the images taken to be determined.

For each image (diagram E3.2) an individual *txt* file was created (see appendix T3.2) with the distances of the camera relative to each LED (in the Pipercub reference frame) and the corresponding *row* and *column* value for that LED. This information was then converted into the necessary format using the **AVI1** converter program for the **MFITvid** program, both of which were developed according to (Hobbs, 2003). A summary of the procedure can be found in appendix T3.3). This process required the **imagecal_spycam** file, determined from experiment 1.

Diagram E3.2: Test image captured from *Eyecam*©, illustrating the location of the LEDs.

3.4) Results:

Experimental results from **Monday 14th of July**, for 2 trials: 1) Varying Z and 2) Increasing X then Varying Z
N.B using a right-handed axis system, with A,B,C and D corresponding to LEDS on Aircraft in Clockwise allocation.

Pixel coordinates distance 1 (X = -5.59m)

	A		B		C		D		Camera position		
Image Name	Col	Row	Col	Row	Col	Row	Col	Row	X (m)	Y (m)	Z (m)
Pierre_machine_vision_test_pipercub_14_july_0002	404	216	473	227	405	237	335	231	-5.59	0.00	-0.21
Pierre_machine_vision_test_pipercub_14_july_0003	439	232	507	240	439	252	370	247	-5.59	0.00	-0.31
Pierre_machine_vision_test_pipercub_14_july_0004	461	244	529	251	461	265	392	258	-5.59	0.00	-0.40
Pierre_machine_vision_test_pipercub_14_july_0005	466	262	536	265	469	285	399	281	-5.59	0.00	-0.55
Pierre_machine_vision_test_pipercub_14_july_0006	473	277	543	277	476	300	405	295	-5.59	0.00	-0.70

Pixel coordinates distance 2 (X = -6.23m)

	A		B		C		D		Camera position		
Image Name	Col	Row	Col	Row	Col	Row	Col	Row	X (m)	Y (m)	Z (m)
Pierre_machine_vision_test_pipercub_14_july_0007	389	217	453	224	392	235	330	233	-6.23	0.00	-0.20
Pierre_machine_vision_test_pipercub_14_july_0008	385	232	447	236	387	250	325	247	-6.23	0.00	-0.31
Pierre_machine_vision_test_pipercub_14_july_0009	427	239	489	244	430	259	367	256	-6.23	0.00	-0.40
Pierre_machine_vision_test_pipercub_14_july_0010	431	245	492	247	432	263	370	262	-6.23	0.00	-0.51
Pierre_machine_vision_test_pipercub_14_july_0011	443	260	505	260	445	279	384	274	-6.23	0.00	-0.70

Location of LEDS on aircraft:

	X (m)	Y (m)	Z (m)
A	-0.67	0.00	-0.13
B	-0.12	0.76	-0.02
C	-0.67	0.00	0.07
D	-0.12	-0.76	-0.02

Table E3.1: Yellow dot camera LED *row* and *column* results, 14th July.

Experimental results from Thursday 17th of July, for 3 trials: 1) Varying Z, 2) Increasing X then Varying Z and 3) Varying Y at constant X and Z
N.B using a right-handed axis system, with A,B,C and D corresponding to LEDS on Aircraft in Clockwise allocation.

Pixel coordinates distance 1 (X = -4.67m)

	A		B		C		D		Camera position		
Image Name	Col	Row	Col	Row	Col	Row	Col	Row	X (m)	Y (m)	Z (m)
Pierre_machine_vision_test_pipercub_17_july_0000	416	210	498	230	416	236	332	288	-4.67	0.00	-0.10
Pierre_machine_vision_test_pipercub_17_july_0002	428	224	511	242	430	250	345	240	-4.67	0.00	-0.20
Pierre_machine_vision_test_pipercub_17_july_0003	429	245	512	259	430	271	346	260	-4.67	0.00	-0.30
Pierre_machine_vision_test_pipercub_17_july_0004	426	264	507	276	426	290	343	278	-4.67	0.00	-0.40
Pierre_machine_vision_test_pipercub_17_july_0005	416	281	497	292	416	306	332	293	-4.67	0.00	-0.50

Pixel coordinates distance 2 (X = -5.86m)

	A		B		C		D		Camera position		
Image Name	Col	Row	Col	Row	Col	Row	Col	Row	X (m)	Y (m)	Z (m)
Pierre_machine_vision_test_pipercub_17_july_0006	375	221	444	238	374	242	312	236	-5.86	0.00	-0.10
Pierre_machine_vision_test_pipercub_17_july_0007	364	233	433	246	364	252	301	246	-5.86	0.00	-0.20
Pierre_machine_vision_test_pipercub_17_july_0008	374	250	444	261	374	270	312	261	-5.86	0.00	-0.30
Pierre_machine_vision_test_pipercub_17_july_0009	386	265	456	275	386	286	324	276	-5.86	0.00	-0.40
Pierre_machine_vision_test_pipercub_17_july_0010	374	276	444	286	372	296	311	286	-5.86	0.00	-0.50

Pixel coordinates distance 3 (X = -5.86)

	A		B		C		D		Camera position		
Image Name	Col	Row	Col	Row	Col	Row	Col	Row	X (m)	Y (m)	Z (m)
Pierre_machine_vision_test_pipercub_17_july_0011	477	280	534	286	476	296	402	286	-5.86	-1.00	-0.50
Pierre_machine_vision_test_pipercub_17_july_0012	523	276	573	284	524	297	447	289	-5.86	-1.50	-0.50
Pierre_machine_vision_test_pipercub_17_july_0013	588	276	631	286	589	298	514	290	-5.86	-2.00	-0.50

Location of LEDS on aircraft:	X (m)	Y (m)	Z (m)
A	-0.67	0.00	-0.13
B	-0.12	0.76	-0.02
C	-0.67	0.00	0.07
D	-0.12	-0.76	-0.02

Table E3.2: Yellow dot camera LED *row* and *column* results 17th July.

Experimental results from Monday 14th of July, for 3 trials: 1) Varying Z, 2) Increasing X then Varying Z and 3) Varying Y at constant X and Z
N.B using a right-handed axis system, comparing actual measurements with MFITVID.exe results

Results 1)

	X (m)				Y (m)			
Image Name	Actual	Estimated	Error (sim)	Difference	Actual	Estimated	Error (sim)	Difference
Pierre_machine_vision_test_pipercub_14_july_0002	-5.59	-5.183	± 0.09379	0.4070	0	-0.0263	± 0.11201	0.0263
Pierre_machine_vision_test_pipercub_14_july_0003	-5.59	-5.2623	± 0.09599	0.3277	0	0.0282	± 0.11433	0.0282
Pierre_machine_vision_test_pipercub_14_july_0004	-5.59	-5.3192	± 0.09689	0.2708	0	0.0294	± 0.11605	0.0294
Pierre_machine_vision_test_pipercub_14_july_0005	-5.59	-5.2961	± 0.09555	0.2939	0	-0.0143	± 0.11568	0.0143
Pierre_machine_vision_test_pipercub_14_july_0006	-5.59	-5.27	± 0.09422	0.3200	0	0.0062	± 0.11391	0.0062
Pierre_machine_vision_test_pipercub_14_july_0007	-6.23	-5.7768	± 0.11741	0.4532	0	-0.0842	± 0.13974	0.0842
Pierre_machine_vision_test_pipercub_14_july_0008	-6.23	-5.789	± 0.11838	0.4410	0	-0.0147	± 0.14091	0.0147
Pierre_machine_vision_test_pipercub_14_july_0009	-6.23	-5.8288	± 0.11873	0.4012	0	-0.0628	± 0.14305	0.0628
Pierre_machine_vision_test_pipercub_14_july_0010	-6.23	-5.8206	± 0.11864	0.4094	0	0.0618	± 0.14128	0.0618
Pierre_machine_vision_test_pipercub_14_july_0011	-6.23	-5.891	± 0.12086	0.3390	0	0.0166	± 0.14479	0.0166

N.B. Position measured relative to the lead aircraft axis system
sim = simulation

Z (m)				Psi (Azimuth/Yaw) rad		Theta (pitch) rad		Phi (Roll) rad	
Actual	Estimated	Error (sim)	Difference	Estimated	Error (sim)	Estimated	Error (sim)	Estimated	Error (sim)
-0.21	-0.1996	± 0.11191	0.0104	-0.0438	± 0.02251	0.1707	± 0.02197	0.0330	± 0.01889
-0.31	-0.1683	± 0.11528	0.1417	-0.13	± 0.02239	0.1248	± 0.02227	0.0581	± 0.01913
-0.40	-0.2214	± 0.11816	0.1786	-0.1759	± 0.02237	0.1049	± 0.02249	0.0613	± 0.01935
-0.55	-0.3214	± 0.11865	0.2286	-0.1809	± 0.02216	0.0674	± 0.02260	0.1334	± 0.01936
-0.70	-0.3059	± 0.11699	0.3941	-0.1943	± 0.02177	0.028	± 0.02241	0.1481	± 0.01918
-0.20	-0.1867	± 0.13907	0.0133	-0.0119	± 0.02514	0.1655	± 0.02445	0.0784	± 0.02106
-0.31	-0.1847	± 0.14070	0.1253	-0.0127	± 0.02511	0.1340	± 0.02469	0.0959	± 0.02117
-0.40	-0.3154	± 0.14436	0.0846	-0.0948	± 0.02523	-0.0948	± 0.02523	0.1086	± 0.02147
-0.51	-0.185	± 0.14237	0.3250	-0.1232	± 0.02482	0.0911	± 0.02480	0.1327	± 0.02127
-0.70	-0.2533	± 0.14674	0.4467	-0.1390	± 0.02498	0.0678	± 0.02518	0.1279	± 0.02157

Table E3.3: Yellow dot camera LED pose estimation results, 14th of July.

Experimental results from Thursday 17th of July, for 3 trials: 1) Varying Z, 2) Increasing X then Varying Z and 3) Varying Y at constant X and Z
N.B using a right-handed axis system, comparing actual measurements with MFITVID.exe results

Results 1)

	X (m)				Y (m)			
Image Name	Actual	Estimated	Error (sim)	Difference	Actual	Estimated	Error (sim)	Difference
Pierre_machine_vision_test_pipercub_17_july_0000	-4.67	-4.1217	±0.05860	0.5483	0	0.1589	±0.06957	0.1589
Pierre_machine_vision_test_pipercub_17_july_0002	-4.67	-4.3477	±0.06514	0.3223	0	-0.0909	±0.07783	0.0909
Pierre_machine_vision_test_pipercub_17_july_0003	-4.67	-4.3326	±0.06485	0.3374	0	-0.0406	±0.07754	0.0406
Pierre_machine_vision_test_pipercub_17_july_0004	-4.67	-4.368	±0.06613	0.3020	0	-0.0042	±0.07919	0.0042
Pierre_machine_vision_test_pipercub_17_july_0005	-4.67	-4.3264	±0.06518	0.3436	0	-0.0083	±0.07762	0.0083
Pierre_machine_vision_test_pipercub_17_july_0006	-5.86	-5.3957	±0.10209	0.4643	0	0.0524	±0.12263	0.0524
Pierre_machine_vision_test_pipercub_17_july_0007	-5.86	-5.392	±0.10234	0.4680	0	0.0212	±0.12170	0.0212
Pierre_machine_vision_test_pipercub_17_july_0008	-5.86	-5.3644	±0.10159	0.4956	0	0.0229	±0.12130	0.0229
Pierre_machine_vision_test_pipercub_17_july_0009	-5.86	-5.3509	±0.10113	0.5091	0	0.0286	±0.12131	0.0286
Pierre_machine_vision_test_pipercub_17_july_0010	-5.86	-5.3112	±0.09985	0.5488	0	0.1161	±0.11901	0.1161
Pierre_machine_vision_test_pipercub_17_july_0011	-5.86	-5.5740	±0.10664	0.2860	-1.00	-0.0024	±0.12536	0.9976
Pierre_machine_vision_test_pipercub_17_july_0012	-5.86	-6.1076	±0.12192	0.2476	-1.50	-0.0715	±0.14808	1.4285
Pierre_machine_vision_test_pipercub_17_july_0013	-5.86	-7.1922	±0.15493	1.3322	-2.00	-0.0556	±0.19365	1.9444

N.B. Position measured relative to the lead aircraft axis system (and in a NED axis)
sim = simulation

Z (m)				Psi (Azimuth/Yaw) rad		Theta (pitch) rad		Phi (Roll) rad	
Actual	Estimated	Error (sim)	Difference	Estimated	Error (sim)	Estimated	Error (sim)	Estimated	Error (sim)
-0.10	-0.1327	±0.07061	0.0327	-0.1387	±0.01758	0.1056	±0.01758	0.3471	± 0.01495
-0.20	-0.1971	±0.07875	0.0029	-0.0744	±0.01861	0.1546	±0.01853	-0.0088	± 0.01580
-0.30	-0.1976	±0.07880	0.1024	-0.0897	±0.01841	0.1079	±0.01861	0.0111	± 0.01578
-0.40	-0.2078	±0.08058	0.1922	-0.0901	±0.01849	0.0675	±0.01887	0.0179	± 0.01594
-0.50	-0.1667	±0.07880	0.3333	-0.0666	±0.01818	0.0223	±0.01869	0.0100	± 0.01574
-0.10	-0.2636	±0.12268	0.1636	0.0077	±0.02363	0.1678	±0.02307	-0.0136	± 0.01982
-0.20	-0.1611	±0.12179	0.0389	0.0350	±0.02327	0.1260	±0.02300	0.0015	± 0.01967
-0.30	-0.2025	±0.12183	0.0975	0.0119	±0.02315	0.0969	±0.02310	0.0020	± 0.01967
-0.40	-0.2486	±0.12218	0.1514	-0.0155	±0.02319	0.0712	±0.02319	0.0108	± 0.01969
-0.50	-0.1916	±0.11981	0.3084	-0.0041	±0.02270	0.0366	±0.02296	0.0023	± 0.01946
-0.50	-0.0178	±0.12778	0.4822	-0.1904	±0.02276	0.0010	±0.02331	0.0011	± 0.02005
-0.50	-0.3968	±0.15492	0.1032	-0.2711	±0.02444	0.0511	±0.02533	0.0581	± 0.02205
-0.50	-0.7545	±0.2115	0.2545	-0.3998	±0.02695	0.0805	±0.02864	0.0749	± 0.02573

Table E3.4: Yellow dot camera LED pose estimation results, 17th July.

Results 4)
Altering both row and column pixel readings by 2 pixels for selected images:

	X (m)				Y (m)			
Image Name	Actual	Estimated	Error (sim)	Difference Res 1	Actual	Estimated	Error (sim)	Difference Res 1
Pierre_machine_vision_test_pipercub_17_july_0002	-4.67	-4.3493	± 0.06517	0.0016	0.00	-0.0914	± 0.07787	0.0005
Pierre_machine_vision_test_pipercub_17_july_0003	-4.67	-4.3353	± 0.06489	0.0027	0.00	-0.0409	± 0.07760	0.0003
Pierre_machine_vision_test_pipercub_17_july_0004	-4.67	-4.3712	± 0.10126	0.0032	0.00	-0.0042	± 0.07926	0.0000
Pierre_machine_vision_test_pipercub_17_july_0007	-5.86	-5.3878	± 0.10126	0.0042	0.00	0.0204	± 0.12160	0.0008
Pierre_machine_vision_test_pipercub_17_july_0008	-5.86	-5.3621	± 0.10155	0.0023	0.00	0.0224	± 0.12124	0.0005
Pierre_machine_vision_test_pipercub_17_july_0009	-5.86	-5.3506	± 0.10112	0.0003	0.00	0.0283	± 0.12130	0.0003
Pierre_machine_vision_test_pipercub_17_july_0011	-5.86	-5.5837	± 0.10684	0.0097	-1.00	-0.0016	± 0.12560	0.0001
Pierre_machine_vision_test_pipercub_17_july_0012	-5.86	-6.1224	± 0.12223	0.0148	-1.50	-0.0694	± 0.14849	0.0005
Pierre_machine_vision_test_pipercub_17_july_0013	-5.86	-7.2151	± 0.15544	0.0229	-2.00	-0.0512	± 0.19435	0.0012

Z (m)				Psi (Azimuth/Yaw) rad		Theta (pitch) rad		Phi (Roll) rad	
Actual	Estimated	Error (sim)	Difference Res 1	Estimated	Error (sim)	Estimated	Error (sim)	Estimated	Error (sim)
-0.20	-0.1979	± 0.07886	0.0008	-0.0786	± 0.01859	0.1503	± 0.01855	-0.0086	± 0.01581
-0.30	-0.1983	± 0.07760	0.0007	-0.0939	± 0.01839	0.1035	± 0.01863	0.0113	± 0.01579
-0.40	-0.2084	± 0.08068	0.0006	-0.0943	± 0.01847	0.0629	± 0.01888	0.0181	± 0.01595
-0.20	-0.1612	± 0.12173	0.0001	0.0308	± 0.02324	0.1215	± 0.02301	0.0016	± 0.01966
-0.30	-0.2026	± 0.12180	0.0001	0.0077	± 0.02313	0.0923	± 0.02311	0.0021	± 0.01966
-0.40	-0.2487	± 0.12220	0.0001	-0.0197	± 0.02305	0.0666	± 0.02320	0.011	± 0.01969
-0.50	-0.1948	± 0.02276	0.1770	-0.1948	± 0.02276	-0.0035	± 0.02333	0.0012	± 0.02008
-0.50	-0.3991	± 0.15550	0.0023	-0.2753	± 0.02442	0.0464	± 0.02535	0.0585	± 0.02208
-0.50	-0.7593	± 0.21219	0.0048	-0.4038	± 0.02693	0.0759	± 0.02867	0.0755	± 0.02577

Table E3.5: Yellow dot camera LED pose estimation results, 17th July, with 2 pixel differences.

3.6) Discussion:

Two experiments were performed in order to provide sufficient data for the analysis using the **Mfitvid** program. In the first experiment (14th July) there were only two sets of images taken varying the cameras position only in *X* and *Z* axes, thus, enabling the performance of the pose estimation program to be determined. For the second experiment (17th July) an additional test varying the camera position in the *Y* axes was included which enabled a complete test of the pose software in all three axes to be performed.

Referring to tables E3.1 and E3.2 the *row* and *column* positions for each of the four LEDs are listed for all of the images captured. A table of the location of each LED with respect to the axes origin is included with both sets of results. Referring to diagram E3.2 the labelling of the LEDs was done in a clockwise manner starting at the 12 o'clock position with *A* followed by *B* then *C* and finishing with *D* at the port wing tip, this information for each image was stored in a *txt* file (see appendix T3.2 for an example) for later use in the **AVI1** program.

Using the **Mfitvid** program the pose estimation of the camera relative to the target object (the Piper cub aircraft, identified by the rear mounted LEDs) was determined for each image in turn, this process required considerable manual configuration and manipulation of the **AVI1** output data. The results are presented in tables E3.3 and E3.4 with the measured *X*, *Y* and *Z* data compared to that predicted. In addition the angular pose of the camera in yaw, pitch and roll has been included.

Comparing the measured and estimated results for the *X*, *Y* and *Z* values in the first experiment, 14th of July (table E3.3), the largest difference for the *X* readings is 0.45*m*. This occurs for the first reading at the -6.23*m* distance (for an elevation value of -0.2*m*) and this difference is the same for the last *Z* reading of -0.70*m*, again at the -6.23*m* value. The *Y* values have fewer differences with the maximum difference of 0.08*m* occurring also for the -6.23*m* readings (at an elevation of -0.2*m*). These differences may be due to the fact that during the vision trials the camera's position is "off-centre" from the target in *X* and *Z*

(being above or below it) unlike in the *Y,* axis which is not varied from its initially aligned position. In addition, the three pose angles estimated are small, as would be expected for a wings level position and a correctly aligned camera. The values are less than 10 degrees with small uncertainties of 1 degree or less.

Referring to the second set of experimental results (see table E3.4) taken on the 17th of July, where an additional trial which included varying in the *Y* axis was performed. This experiment highlighted the difficulty with estimating the pose position when the *Field of View* is not perpendicular to the target object. In the *X* direction the largest difference occurred for the maximum *Y* displacement of -2*m* with an overestimation of 1.332*m* predicted by the program. Again this same *Y* displacement produced the largest error in *Y* estimation with an underestimation of 1.944*m* by the algorithm. The largest difference in the Z direction occurred for the -1m *Y* displacement with an underestimation of 0.48*m*. Therefore, the ability to determine the pose of the camera relative to the object is affected when observing a target from the side / "off-centre" position. This is further highlighted when analysing the number of iterations required to achieve a solution for *image 05* and *image 13*, the first required only 2 iterations while the latter required 28.

In addition, the in-built error estimation for the **Mfitvid** program did not compare well with the "real" error differences determined by measuring. For the majority of the cases the error was underestimated. Using the Correlation matrix for the *image 13* result (see appendix T3.4) the relationships between *Y* and the 5 variables can be seen:

- Y and X, -0.00743
- Y and Z, -0.00612
- Y and ψ, -0.96982
- Y and θ, -0.111084
- Y and φ, 0.30110

The above results show that there is large negative correlation between Y and ψ. Furthermore, a very small negative correlation can be seen between X, Z, θ and Y and finally, the roll angle φ, has a positive medium correlation with Y. From these relationships it can be said that further changes to Y will result in poorer X, Z and θ estimations by the **Mfitvid** program. However, it should be highlighted that the camera calibration is only of first order. Therefore, a first step to understanding the error discrepancy would be to obtain a higher order camera calibration.

Comparing the pose angles determined for the X = -4.67m and X = -5.86m distances (see table E3.4), the largest angles for yaw and pitch occur for X = -5.86m with Z = -0.1m in the order of 10 degrees. However a larger than expected roll angle of 20 degrees is predicted for the X = -4.67m and Z = -0.1m case. After calculating the trigonometry this last result would require the camera to be located at Y = -1.59m which is clearly not the case, therefore this result is anomalous. However, the other results are within acceptable values of less than 10 degrees. Referring to the Y displacement results in table E3.4 for the pose angles it is interesting to observe the yaw angles as these angles agree well with those calculated by trigonometry, using the X and Y displacement values. Finally, the pitch and roll angles remain close to zero which is as expected.

Furthermore, an attempt to investigate the effect of changing the pixel coordinates for the *row* and *column* position of each LED by two pixels was performed (see table E3.5). This was done in order to determine the sensitivity of the program to mistakes in the actual location of the LED's centre in establishing the target object's pose. Overall, there are no major differences between the *X*, *Y* and *Z* distances with respect to the original values (table E3.4) greater than 0.02*m*. In this respect, it should be noted that the anomalous result occurring at X = -5.86*m*, Y = -1*m* and Z = -0.1*m* is excluded (which estimates a difference of 0.2*m*). Finally, observing the comparison between the pose angles the differences are of the order of 1 to 2 degrees with the original angles. Therefore, it can be seen that this simple investigation indicates that the algorithm is suitably well mannered, that small errors in pixel coordinates do not create large pose estimation.

3.7) Conclusion:

Using the **AVI1** and **Mfitvid** programs provided by (Hobbs, 2003)a technique enabling the pose estimation of a camera relative to a target has been trailed. This method provides reliable results in the *X*, *Y* and *Z* directions and yaw (ψ), pitch (θ) and roll (φ) angles provided the camera is perpendicular to and in-line with the centre of the object. However, there are number of problems with the pose estimation when the camera is displaced both in the Y direction and for low *Z* (elevation) values. The angular position of the camera has also been estimated for the steady wing level condition at different –*X* distances and the results for yaw, pitch and roll reflect this with their small estimated angles

An additional investigation into the effect of pixel errors on the final pose estimation has also been performed. For errors of 2 pixels in both *row* and *column* coordinates **Mfitvid** is still capable of estimating the pose of the camera correctly with minimal differences in comparison with the zero error input data. Thus the position estimation exhibits good robustness with respect to pixel errors.

Appendix T3.1:

Directions for using GIMP 2: in order to determine the pixel row and column values from the test images.

1) Double-click on the GIMP 2© desktop icon to launch the program to open up GIMP.

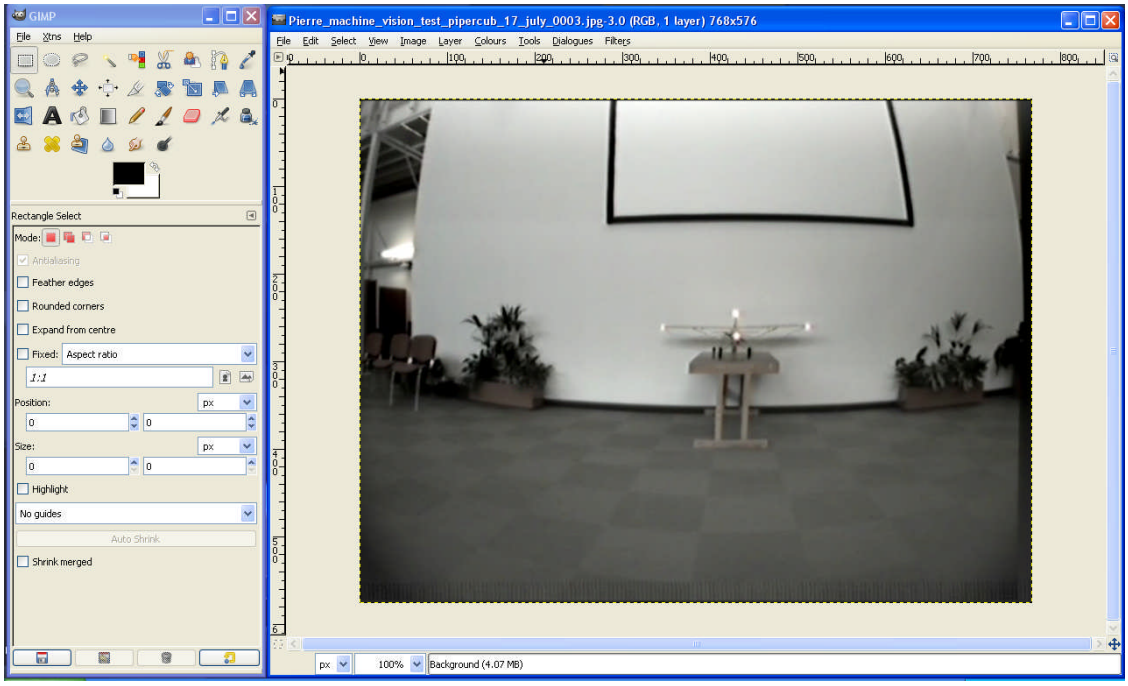

Diagram T3.1: Screen shot of the *GIMP 2*© image processing tool.

2) Select the image to be analysed by clicking on **File**, **Open**, which opens the **Open Image** window. Using the **Places** box select the image file location. Clicking on the desired file will enable a thumbnail of the image to be displayed in the **Preview** box. In the bottom right corner of the window select **All Images** option from the drop down menu and then click **Open**.

3) Once **Open** has been clicked a stand alone window with the selected image will appear in the desktop area. In order to analyse the position in the image for the LEDs select the **Rectangle Select Tool** (top left icon, see diagram T3.1) in the GIMP main window.

4) Then bringing the mouse curser over into the image window, place the curser above each LED in turn, noting the row and column values which are displayed in the bottom left of the image window. The labelling of the four LEDs is in a clockwise manner starting from the top LED at the 12 o'clock position.

Appendix T3.2:

A sample *text* file for the LED positions as required by the **AVI1** program is shown below (this file should be saved at the following address **c:\videowork**). Each image should have a similar file with a suitable filename for easy recognition during the image processing:

% Camera position calibration data file.
Pierre_machine_vision_test_pipercub_17_july_0000
% For spycam, Piper Cub expt 17 Jul 2008; measurements in m rather than cm.
%
% Exactly 9 comment lines (ignored, % prefix optional), then line with number of points
% followed by 1 data line for each point giving label (string <= 19 char, no white space),
% x y z values of point in user units and then col and row values for that point in the
% image, values separated only by spaces.
%
% S.E. Hobbs, 17 Jul 2008, PDJ 04 Aug 2008 01:48
4
A -0.67 0.0 -0.13 416 210
B -0.12 0.76 -0.02 498 230
C -0.67 0.0 0.07 416 236
D -0.12 -0.76 -0.02 332 288

Insert T3.1: This file is required along with the **imagecal_spycam** file (determined in experiment 1) to produce the required data input for the **AVI1** program which in produces the correct input files for the **Mfitvid** program to determine the target objects pose.

Appendix T3.3: basic guides to using the **AVI1** and **Mfitvid** programs, for further information refer to (Hobbs, 2003) *Appendix B*.

AVI1:

1) Launch the **AVI1** .exe program, from the *top level menu* select option 2 by inputting **2** followed by **return**.

2) Following the top level menu choice a *Target tracking submenu* will be open, again typing **2** followed by **enter**, selects the necessary option to create the **Mfitvid** files.

3) Specify the work directory for the input data, by typing **c:\videowork** at the directory prompt, followed by **return**, confirm this selection by, **y** followed by **return**.

4) The IMAGE CALIBRATION file should be saved at the above address with the following filename: **Imagecal_spycam.txt**. At the screen prompt type in the filename, press **enter**, confirm the file name with, **y** and again press **enter**.

5) The POSITION CALIBRATION DATA file (such as in insert E3.1) is next specified by typing in the necessary filename e.g. **spycamposcaldata**.txt** followed by **enter**, **y** and **enter** again (with ** replaced with the image number).

6) The OUTPUT filename is then specified, e.g. **cubtest**** followed by **return**, **y** and **return** to confirm. Following this the camera used for the conversion needs to be specified. At the prompt enter **1**, followed by **enter**. Then specify the direction in which the *column* and *row* increase. When using GIMP 2©, the required inputs are: **1**, **return**
-1, **return**. Finally specify the measurement uncertainty as: **0.004** followed by **enter**. This will then display the position calibration data on screen, pressing **enter** will return to the *Target tracking sub menu*, with the necessary files for **Mfitvid** saved in the work directory.

7) Finally, select all the dat.txt files created in the previous step and place them at the following address: **c:\video\ref0**

Mfitvid:

1) Launch the **Mfitvid** program, from the Main menu select option 1 to load the **AVI1** data by typing **1** followed by **return** at the screen prompt.

2) At the file directory entry prompt press **enter** (i.e. select the address **c:\video\ref0**) followed by, **y** and **enter** again.

3) Next, input the filename containing the position data, **cubtest**dat.txt** , followed by **enter**. A prompt for the number of data records to be skipped will open automatically, enter **0**. This will then open the MODEL fit menu.

4) Select option 3 by entering, **3**.For the first record prompt enter **0** followed by **enter** then for the last record enter **7** followed by **return**. Then the option for varying the parameters is printed on the screen. At each of the six screen prompts enter **1**, followed by **enter** thus enabling all 6 parameters to be varied.

5) Using the measurement data collected during the imaging trials, these values can then be inputted as initial guesses into the program. The first three prompts relate to ***-X***, ***-Y*** and ***-Z*** (remember to keep in mind the axes being used). The next three prompts relate to the position angles *yaw*, *pitch* and *roll*. For the steady level flight, input **0** for both *yaw* and *pitch* (a[4] and a[5]) followed by **return** each time, for a[6] enter **3.14**. This is required to perform the necessary axes transformation.

6) The program then calculates iterations using the inputted data as starting values before returning a *Results analysis* submenu. The determined values can be displayed on screen by entering **1**. These details can also be saved to a *txt* file using option **4**, which allows the save to location and file name to be specified. Finally, option **7** enables the covariance matrices to be saved to file for later analysis.

Appendix T3.4:

Example curvature, covariance and correlation matrices for:

Pierre_machine_vision_test_pipercub_17_july_0013

```
# Curvature and covariance matrices from modelfit, v  1.10
# Calculated on Tue Aug 05 18:38:26 2008
# Source file is spycamimage17JLY13dat.txt
# SVD routines have deleted  0 (fit),  0 (error bounds) eigenvectors

# Curvature matrix (alpha):
     6      6
 1.077940e+002 -1.273632e+002 -6.078913e+002 -9.153774e+002 -4.009583e+003 -1.719997e+003
-1.273632e+002  6.989261e+003  3.295221e+001  4.972047e+004  2.302065e+003 -6.400314e+002
-6.078913e+002  3.295221e+001  5.793128e+003  2.700548e+002  3.796974e+004  1.654776e+004
-9.153774e+002  4.972047e+004  2.700548e+002  3.552301e+005  1.645991e+004 -3.960487e+003
-4.009583e+003  2.302065e+003  3.796974e+004  1.645991e+004  2.507400e+005  1.080350e+005
-1.719997e+003 -6.400314e+002  1.654776e+004 -3.960487e+003  1.080350e+005  4.903418e+004

# Covariance matrix (covar):
     6      6
 2.400387e-002 -2.230673e-004  4.315779e-003  9.923819e-005 -2.290034e-004 -1.048099e-004
-2.230673e-004  3.750062e-002 -2.502999e-004 -5.204025e-003 -6.146947e-004  1.500134e-003
 4.315779e-003 -2.502999e-004  4.458571e-002  2.461953e-004 -5.639154e-003 -2.453998e-003
 9.923819e-005 -5.204025e-003  2.461953e-004  7.265499e-004  5.267563e-005 -2.049050e-004
-2.290034e-004 -6.146947e-004 -5.639154e-003  5.267563e-005  8.200835e-004  8.441056e-005
-1.048099e-004  1.500134e-003 -2.453998e-003 -2.049050e-004  8.441056e-005  6.619306e-004

vector of covariance eigenvalues
    0.046283      0.023172      0.038283      0.000555      0.000003      0.000003

# Correlation matrix (corr):
     6      6
 1.000000e+000 -7.434915e-003  1.319231e-001  2.376323e-002 -5.161456e-002 -2.629393e-002
-7.434915e-003  1.000000e+000 -6.121298e-003 -9.969822e-001 -1.108437e-001  3.010958e-001
 1.319231e-001 -6.121298e-003  1.000000e+000  4.325628e-002 -9.325822e-001 -4.517209e-001
 2.376323e-002 -9.969822e-001  4.325628e-002  9.999999e-001  6.824141e-002 -2.954701e-001
-5.161456e-002 -1.108437e-001 -9.325822e-001  6.824141e-002  1.000000e+000  1.145675e-001
-2.629393e-002  3.010958e-001 -4.517209e-001 -2.954701e-001  1.145675e-001  1.000000e+000
```